Point Contacts in Chalcopyrite Solar Cells

im Fachbereich Physik
der Freien Universität Berlin eingereichte
Dissertation

zur Erlangung des akademischen Grades
eines Doktors der Naturwissenschaften
(Dr.rer.nat)

von

Binoy Chacko

angefertigt am
Helmholtz Zentrum Berlin für Materialien und Energie

HZB Helmholtz Zentrum Berlin

2018

Gutachter:

1. Frau Prof. Dr. Martha Ch. Lux-Steiner (Betreuerin)

2. Herr Prof. Dr. Paul Fumagalli

Disputation am 05.03.2019

Table of contents

Abstract

Recent advancements in Cu(In,Ga)Se_2 based solar cells with alkaline fluoride treatment have suggested the role of the recombination at the absorber/buffer interface as a limiting factor of open-circuit voltage (V_{oc}) in high-efficiency CIGSe solar cells [1, 2]. Therefore, this work focuses on the interface engineering at the CIGSe/ buffer of 2 μm standard absorbers. Furthermore, as the influence of recombination at the back interface becomes noticeable with thin absorbers, the back interface Mo/CIGSe of thinner absorbers is also optimised. Both use the concept of point junctions through a passivation layer (PaL). A low-cost versatile technique for point contact fabrication is developed by using a nanolithographic technique employing a sacrificial template of low temperature synthesised, mono-dispersed, self-assembled and size-tunable CdS nanoparticels (NP's), and a PaL of aluminium oxide (Al_2O_3), thereby achieving 60 nm point contact radius and a maximum of 89% PaL coverage on CIGSe. The impact of point contacts at the CIGSe/buffer interface on solar cell performance is theoretically analysed using three-dimensional simulations on the point contact radius, coverage area, defect density and interface quality. An efficient PaL should create positive surface charge, which induces band bending at the CIGSe/PaL and influences the contact junction properties; its beneficial effect on V_{oc} and efficiency reaches a maximum when the coverage area of PaL is more than 95% and the interface charge density is greater than 10^{12} cm^{-2}.

The point contact technology is experimentally validated by incorporating it into tangible CIGSe devices, featuring CdS and Zn(O,S) buffer layers. A positive impact of +10.4% is seen on the V_{oc} of the point contact devices with sputtered Zn(O,S) compared to the unpassivated reference cells. However the power conversion efficiency (PCE) didn't follow the same trend, which might be due to an upward bandbending created by Al_2O_3 at the interface, impeding the current flow. Nonetheless, at the Mo/CIGSe interface of thinner CIGSe absorbers, the technology led to a significant reduction in the surface recombination velocity, due to the back surface field from the Al_2O_3 layer. Consequently, all cell parameters of point contact devices showed a relative improvement to the unpassivated reference devices: open-circuit voltage (V_{oc} : +21%), short-circuit current (J_{sc}: +2.6%), fill-factor (FF: +4.9%), and efficiency (η: +31%).

Zusammenfassung

Jüngste Fortschritte bei Cu(In,Ga)Se_2-basierten Solarzellen durch eine Alkalimetallfluorid-Behandlung haben dazu geführt, dass die Ladungsträgerrekombination an der Absorber/Puffer-Grenzfläche als limitierender Faktor für die Leerlaufspannung (V_{oc}) in hocheffizienten CIGSe-Solarzellen diskutiert wird [1,2]. Daher konzentriert sich diese Arbeit auf die Optimierung der Grenzfläche CIGSe/Puffer von Solarzellen mit 2 μm Standardabsorbern. Außerdem wird auch der Rückkontakt Mo/CIGSe von Solarzellen mit dünneren Absorbern optimiert. In beiden Fällen wird das Konzept der Punktkontakte durch eine Passivierungsschicht (PaL) verwendet. Eine vielseitige, kostengünstige nanolithografische Technik zur Herstellung von Punktkontakten wird unter Verwendung einer Opferschicht realisiert, die als Schablone eingesetzt wird. Diese besteht aus bei niedrigen Temperaturen synthetisierten, monodispersen und größenabstimmbaren CdS-Nanopartikeln (NP's) und einem PaL aus Aluminiumoxid (Al_2O_3). Damit lässt sich ein Punktkontaktradius von 60 nm und eine Oberflächenbedeckung von maximal 89% PaL auf CIGSe erreichen. Der Einfluss von Punktkontakten an der CIGSe/Puffer-Grenzfläche auf die Leistung der Solarzelle wird mittels dreidimensionaler Simulationen unter Berücksichtigung des Punktkontaktradius, der Oberflächenbedeckung, der Defektdichte und der Qualität der Grenzfläche analysiert. Eine effiziente PaL sollte eine positive Oberflächenladung erzeugen, die am CIGSe/PaL eine Bandverbiegung induziert und damit die Eigenschaften der Grenzfläche beeinflusst; ihre positive Wirkung auf V_{oc} und den Wirkungsgrad erreicht ein Maximum, wenn die Oberflächenbedeckung der PaL mehr als 95% beträgt und die Grenzflächenladungsdichte größer als 10^{12} cm^{-2} ist.

Die Punktkontakttechnologie wird mithilfe von CIGSe-Solarzellen mit CdS- und Zn(O,S)-Pufferschichten experimentell validiert. Eine Steigerung der V_{oc} um 10,4% gegenüber den unpassivierten Referenzzellen wird mit der Punktkontaktsolarzelle erzielt. Allerdings wird keine Erhöhung des gesamten Wirkungsgrads erreicht, was auf eine von Al_2O_3 erzeugte, nach oben gerichtete Bandverbiegung an der Grenzfläche hindeuten könnte, die den Stromfluss behindert. Am Mo/CIGSe-Rückkontakt von dünneren CIGSe-Absorbern führt die Einführung der Punktkontakte jedoch zu einer signifikanten Senkung der Oberflächenrekombinationsgeschwindigkeit, bedingt durch das durch Ladungen in der Al_2O_3-Schicht induzierte elektrische Feld. Folglich zeigten alle Zellparameter von Punktkontaktsolarzellen eine relative Verbesserung gegenüber den unpassivierten Referenzzellen: Leerlaufspannung (V_{oc} : + 21%), Kurzschlussstrom (Jsc: + 2,6%), Füllfaktor (FF: + 4,9%) und Wirkungsgrad (FF+ 31%).

Symbols and Abbreviations

α	Absorption coefficient
λ	Wavelength
A	Ideality factor
C	Concentration
E_a	Activation energy
E_c	Conduction band minimum
E_v	Valence band minimum
E_d	Defect position
E_F	Fermi energy
E_{kin}	Kinetic energy
E_g	Band gap
$E_{g,if}$	Interface band gap
ΔE_c	Conduction band offset
ΔE_v	Valence band offset
J_L	Photocurrent density
J_0	Saturation current density
J_{rec}	Total current density
k	Boltzmann's constant
n/p	Electron/hole density
n_i,	intrinsic carrier density
n_1	Available electron density
p_1	Available hole density
N_A	Acceptor state density
N_D	Donor state density
N_c	DOS in conduction band
N_v	DOS in valence band
N_d	Defect density
h	Planck's constant
ϕ	Work function
ϕ_h	Hole barrier height
q	electron charge
R	Recombination rate
R_s	Series resistance
R_p	Parallel resistance
S_{rec}	Surface recombination velocity
V_{oc}	Open circuit voltage
T	Temperature
η	Efficiency
μ_n / μ_p	Electron/hole mobility
τ_n/τ_p	Electron/hole lifetimes
v_{th}	carriers thermal velocity
σ_p	Hole capture cross-section
σ_n	Electron capture cross-section
ALD	Atomic layer deposition
BE	Binding energy
CBD	Chemical bath deposition
CBM	Conduction band maximum
CBO	Conduction band offset
CIGSe	$Cu(In,Ga)Se_2$
DOS	Density of states
EQE	External quantum efficiency
FEM	Finite element method
ILGAR	Ion layer gas reaction
IQE	Internal quantum efficiency
KCN	Potassium cyanide
PaL	Passivation layer
PC	Point contact
PDE	Partial differential equation
PDT	Post-deposition treatment
PERC	Passivated emitter and rear cells
PVP	Polyvinylpyrrolidone
SCAPS	Solar cell Capacitance Simulator
SEM	Scanning electron micrograph
TMA	Trimethylaluminum
TRPL	Time resolved photoluminescence
VBM	Valence band maximum
VBO	Valence band offset
XRD	X-ray diffraction
XPS	X-ray photoelectron spectroscopy
χ	Electron affinity

1

Introduction

Even in a post-truth world, climate change is a fact that can no longer be denied. Its direct relation to the extended exploitation of fossil-fuels is unequivocal. For a long time, we ignored this fact to meet our increasing energy demand. Now, more concrete evidence confirms that extreme weather and climate events across the world are human-induced [3]. At last, we are alarmed! One consequence was the Paris agreement, which set the ambitious target of holding the average global temperature rise below 2°C by reducing greenhouse gas emissions to 40 gigatonnes [4]. 90% of this reduction can be achieved by a rapid and massive implementation of renewables with high energy efficiency [5].

In the energy market, renewables are still in their adolescence. They are the fastest growing energy source, with consumption predicted by an average of 500 TWh/year from 2015 to 2040 [6]. Economically, the use of alternative energy sources alias renewables is expensive compared to non-renewables. But this gap is narrowing in the case of the photovoltaic (PV) sector. In the last decade, the PV sector has seen an exponential growth, mainly due to the decline in the solar PV module prices about 80% [7].

Albeit the solar energy shares only 1.8% of the global power generation in 2018 [8], indeed, it alone has the potential to meet the global energy demand. Silicon has been dominating the photo-voltaic industry from the beginning. But with the introduction of the second-generation solar cells, better known as thin-film solar cells, the prospect is getting bigger. In 2018, thin-film solar cells hold a market share of 8% of the solar industry, and solar cells based on copper indium gallium di-selenide absorbers $\left(\mathrm{Cu(In,Ga)Se_2}\right.$ abbreviated as CIGSe$\left.\right)$ are experiencing an efficiency leap with the introduction of post-deposition treatment on the CIGSe surface with alkali fluorides (KF, NaF, RbF, CsF) [1, 9, 10]. In the last six-years, a 25% surge in the efficiency has resulted in reaching lab efficiencies up to

22.8%, surpassing poly-crystalline silicon [10]. These reports suggest the role of the $p-n$ junction interface between CIGSe and CdS as a limiting factor for the efficiency. Also, the interface states at the CIGSe/CdS interface are of a concern for achieving a high quality interface as they can act as the main recombination channel for electrons and holes and reduce the open-circuit voltage (V_{oc}) and efficiency [11]. Therefore, for a further improvement of CIGSe device performance, interface engineering at the CIGSe/CdS interface is inevitable.

In this scenario, the concept of passivated emitter and rear cells (PERC) used in silicon solar cells at the rear contact for efficiency enhancement could be seen as a prospect for CIGSe solar cells [12]. The recombination rate of electrons and holes at interfaces in solar cells is determined by the total contact area. Also, the recombination rate determines the V_{oc} of the device because it causes the reverse bias saturation current density, J_0: $V_{oc} = \frac{AkT}{q}\, In\left(\frac{-J_L}{J_0}+1\right)$, (with A = ideality factor, k = Boltzmann constant, T = temperature, q = charge of the electron, and J_L = photocurrent density). At room temperature and assuming A = 1, this means that V_{oc} will increase by around 60 mV per decade of the ratio (J_L/J_0). If the contact area that limits the V_{oc} can be reduced by a factor of 100, this means an increase of V_{oc} by approximately 120 mV, provided the non-conducting area is passivated perfectly. The aim of this work is to introduce this concept at the CIGSe/CdS interface of 2 μm standard absorbers or Mo/CIGSe interface of thinner absorbers using lithographic techniques with the objective to see higher open circuit voltages than conventional devices made from the same materials.

The goals of this work are achieved in three steps: (i) Developing a facile, effective and stable technology for implementing a porous passivation layer resulting in nano-point contacts at the CIGSe/buffer or Mo/CIGSe interface. (ii) Theoretical analysis of the influence of the point contacts at CIGSe/CdS or Mo/CIGSe interface on the device performance (iii) Implementing the point contact technology in tangible CIGSe devices, and analysing its influence on solar cells energy conversion efficiency.

This thesis is structured in the following way:

Chapter 2 covers an introduction on the basics of the CIGSe solar cells, including material properties, state-of-art device structure, significance of band offsets at the CIGSe/buffer

interface and main recombination mechanisms in CIGSe devices.

Chapter 3 deals with a low-temperature synthesis of mono-dispersed and self-assembled cadmium sulphide nanoparticles (NP's) by a modified chemical bath deposition and using it for point contact fabrication with a passivation layer of Al_2O_3.

Chapter 4 discusses theoretical simulation on the influence of point contact junctions at the CIGSe/buffer interface on the device performance using the three-dimensional finite element based software WIAS-TESCA and the one-dimensional SCAPS.

Chapter 5 presents the experimental results of the CIGSe solar cells energy conversion efficiency after the implementation of point contacts at the CIGSe/buffer interface of the standard 2 μm thick CIGSe absorbers.

Chapter 6 presents the experimental results on the influence of point contacts at the Mo/CIGSe interface of thinner CIGSe absorbers on device performance.

Chapter 7 gives a summary of the theoretical and experimental results on the influence of point contacts at the CIGSe/buffer and the Mo/CIGSe interface on CIGSe solar cell performance.

2

Basics of $Cu(In,Ga)Se_2$ solar cells

The energy crisis in the late seventies was an epiphany and changed the attitude towards the renewable energy sources. Consequently, the birth of the second generation solar cell took place. Currently, the second generation or the so called thin film photovoltaics occupies a market share of 8% [13]. Some of the favourites in this group includes amorphous silicon (a-Si), cadmium telluride (CdTe) and chalcopyrites ($Cu(In,Ga)(S,Se)_2$ and related compounds). Among the thin-film solar cells, chalcopyrites solar cells based on $Cu(In,Ga)Se_2$ (CIGSe) have reached efficiencies up to 22.8%, surpassing even polycrystalline silicon [1, 10]. The surge in the efficiencies of CIGSe based devices is owed to the post-deposition treatment (PDT) with alkali fluorides [9]. This has reported to improve the CIGSe surface and interface quality between the CIGSe and CdS [10, 14, 15]. Inspired by this, in this work, an innovative attempt has been made to improve the interface quality and thereby reduce interface recombination by incorporating the concept of the point contacts at the front (CIGSe/CdS) or back (Mo/CIGSe) interface of the $Cu(In,Ga)Se_2$ devices. This is the topic of discussion of this thesis, but before that a brief introduction to the CIGSe technology — the design, device preparation, device characteristics, and an overlook on the prominent recombination mechanisms are presented in this chapter.

2.1 $Cu(In,Ga)Se_2$ (CIGSe)

$Cu(In,Ga)Se_2$ is a p-type quaternary semiconductor alloyed from $CuInSe_2$ and $CuGaSe_2$, which crystallizes in the tetragonal structure and is hence included in the group of chalcopyrites [16, 17]. This I-III-VI_2 (I: Cu, III: In and Ga and VI: Se) chalcopyrite resembles the zinc-blende structure with an ordered substitution of Zn with Cu, In and Ga. The two cations, Cu and In or Ga, are bonded tetrahedrally with four Se anions, and each Se anion

is coordinated to two Cu and two In or Ga cations as shown in Figure 2.1. However, unlike in the zinc-blende structure, the lattice constants, *a* and *c*, are distorted due to differences in the bond strength between the covalent (Se–Cu) and the partially ionic bonds (Se–In, Se–Ga) [17–19]; the unstrained crystal structure has *c/a* = 2, which is equal to a Ga content, *x* = 0.23, and a higher or lower deviation of *x* will decrease or increase the *c/a* ratio respectively [20].

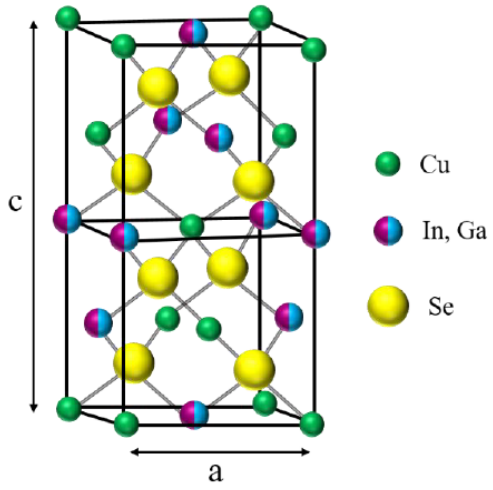

Figure 2.1: The unit cell of a Cu(In,Ga)Se_2 compound with the lattice parameters *a* and *c*. Cu, In (or Ga) and Se atoms are represented by green, purple (or blue) and yellow spheres respectively. Taken from [21].

What makes the CIGSe more desirable from its counterparts is its high absorption coefficient (α = 10^5 cm^{-1}), direct and tunable band gap ($CuInSe_2$: 1.04 eV – $CuGaSe_2$: 1.68 eV), cost-effective production techniques, excellent electronic properties, and a high tolerance towards environmental conditions, even to cosmic radiation [22, 23].

2.2 Structure of a CIGSe solar cell

A typical CIGSe solar cell is made by depositing sequentially layers of molybdenum, CIGSe, cadmium sulphide (CdS), intrinsic zinc oxide (i-ZnO) and aluminium doped zinc oxide (ZnO:Al) on a soda-lime glass substrate (Mo/Cu(In,Ga)Se_2/CdS/i- ZnO/ZnO:Al). Figure 2.2 shows the stack arrangement of these layers and a corresponding SEM cross-section of a CIGSe device. The reference CIGSe solar cells used in this thesis follows the same configuration.

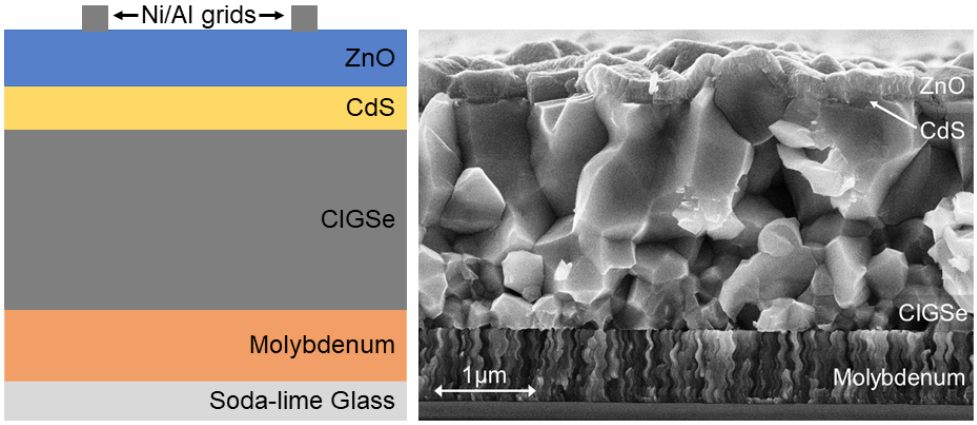

Figure 2.2: Left: Schematic representation of the cross-section of the standard CIGSe solar cells. Right: Scanning electron micrograph (SEM) of the cross-sectional view of a CIGSe solar cell.

In a standard CIGSe solar cell preparation, soda-lime glass of 2 mm thickness is used as the substrate. It is subsequently sputtered with 800 nm of molybdenum (Mo), a metal having work function (Φ = 4.3 eV) close to the CIGSe (Φ = 4.6 eV) [24, 25], to serve as the back contact. On top of the Mo, the CIGSe absorber layer of thickness between 600 nm - 2 μm is deposited by means of a three-stage co-evaporation process using Cu, In, Ga and Se sources. Detailed descriptions of the process can be found in literature [26–28]. Following this, the chemical bath deposition (CBD) of the buffer layer, cadmium sulphide (CdS) (E_g = 2.4 eV, thickness, d = 50-60 nm), is done. CdS offers a better lattice match (CIGSe: a = 5.7 Å, CdS: a = 5.8 Å) [29–31], a favourable band-alignment between the absorber and window layer by diffusion of Cd into the absorber, transforming CIGSe surface to an n-type. [32–34]. Apart from the CdS, alternative buffer layers like Zn(O,S), In_2S_3, (Zn,Sn)O_y, (Zn,Mg)O, and (Zn, Mg)O/Zn(O,S,OH), have also been intensively investigated [10, 35].

In a CIGSe device, the p-n junction is formed between the p-type CIGSe, and the n- type CdS and the ZnO window layers — an intrinsic layer of 110 nm i-ZnO followed by a 250 nm highly aluminium doped ZnO (ZnO:Al). The highly resistive i-ZnO reduces the impact of shunts on the cell performance [36]. The higher band gap (E_g = 3.3 – 3.4 eV) ZnO window layers deposited by reactive sputtering allows most of the incoming light to reach the CIGSe absorber. The completion of the solar cell is done by evaporating a Ni/Al grid, which serves as the front contact.

2.3 Band offsets at CIGSe/buffer interface

In hetero-junction devices like CIGSe, a band discontinuity occurs at the CIGSe/CdS interface due to the difference in their energy band positions in reference to the vacuum level. They could control the electron transport across the CIGSe/buffer interface and have a direct impact on the device power conversion efficiency. A simulated band diagram of a CIGSe solar cell is shown in Figure 2.3. Even if high defect concentrations are present at the CIGSe/buffer interface, a favourable band alignment at the interface can reduce their effect on the open circuit voltage [37]. In chalcopyrites, it is shown that a moderate spike in the conduction band at the CIGSe/buffer interface, $0.0 < \Delta E_c < 0.3$ eV, is beneficial for reducing the interface recombination [33, 38]. Because the spike increases the hole barrier height (the energetic difference between the valence band maximum and the Fermi level, ϕ_h) and hence reduces the local hole density seen by their recombination partners, electrons from the CIGSe absorber [39]. Also, it increases the effective bandgap at the CIGSe/buffer interface, and thus chances for a cross recombination channel (a recombination involving holes from the absorber with the electrons from the buffer via interface defect) are the least; this will be opposite in the case of a cliff, $\Delta E_c < 0$.

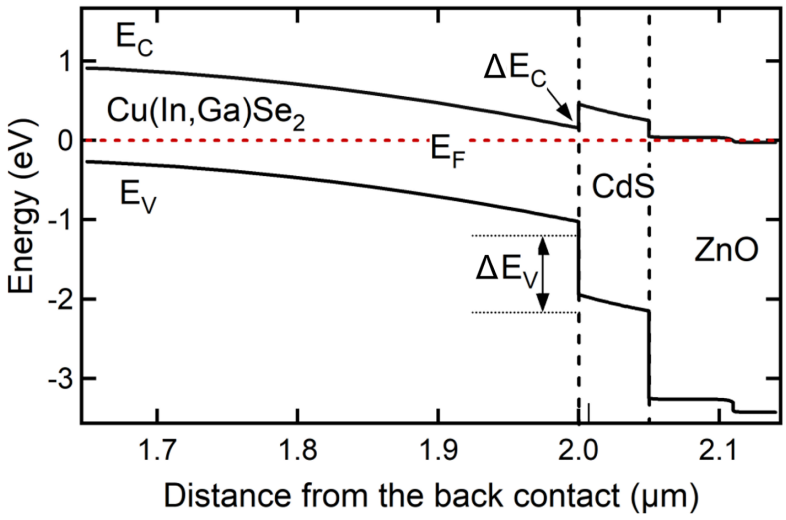

Figure 2.3: Simulated band diagram of a CIGSe solar cell, close to the region of the CIGSe/CdS/ZnO. The semiconductor parameters are according to the default values in Table 4.1

Another important aspect to discuss in connection with the CIGSe/CdS interface is the type inversion. This means that the conduction band of the p-type absorber is close to the Fermi-energy, E_F, at the CIGSe/buffer interface. An asymmetric doping, i.e, a highly

doped buffer layer in comparison to CIGSe, along with donor-like states or donor states alone at the interface could trigger the type-inversion [37]. Under these conditions, the photo-generated minority carriers (electrons) in the p-type CIGSe will become the majority carriers as they reaches the interface. And since their counterpart (holes) concentration is low at a type inverted interface, the recombination is minimised.

2.4 Recombination Mechanisms in CIGSe solar cells

Recombination of charge carriers in solar cells is unavoidable and unfavourable for the device performance. In simple terms, it can be defined as the mechanism through which the charge carrier population decays, i.e. unification of an electron and a hole; therefore, it has a direct influence on the electrical transport mechanisms of a device. In a solar cell, recombination of carriers is spread throughout the device, with several recombination channels accompanied by different recombination mechanisms.

While considering Cu(In,Ga)Se_2 devices, assessing the main recombination channel is difficult. This is due to the fact that recombination can occur in the entire structure, i.e. in the CIGSe or CdS or ZnO or at the Mo/CIGSe, CIGSe/CdS, CdS/ZnO interfaces. Since the CIGSe band gap (1.1 - 1.2 eV) is low as compared to the CdS (2.4 eV) or ZnO (3.3 eV) layers, most of the diode current contribution comes from the CIGSe, which means that the CIGSe is at the greatest stake of recombination. The total current density, J_{rec}, due to recombination in a dominion of interest is given by the Eq. (2.1), where R is the net recombination rate, and the net recombination rate for a defect related recombination is given by the Schockley and Read and Hall (SRH) formalism is shown in Eq. (2.2) [40]. SRH, a quasi-stationary approximation of electrons in the traps, is a two step process assisted via the trap levels giving the probability of a total of four processes — trapping of an electron from the conduction band, emission of a hole to the valence band (capturing of an electron from valence band by a trap), capture of a hole from the valence band, and emission of an electron into the conduction band.

$$J_{rec} = q \int R dz \tag{2.1}$$

$$R = \frac{np - n_i^2}{\tau_n(n + n_1) + \tau_p(p + p_1)} \tag{2.2}$$

$$\tau_n = \frac{1}{\sigma_n \, N_d \, v_{th}} \quad and \quad \tau_p = \frac{1}{\sigma_p \, N_d \, v_{th}} \tag{2.3}$$

$$n_1 = N_c \, exp\left(-\frac{E_c - E_d}{kT}\right) \quad and \quad p_1 = N_v \, exp\left(-\frac{E_d - E_v}{kT}\right) \tag{2.4}$$

where; n/p : electron/hole density
n_i,v_{th} : intrinsic carrier density, carriers thermal velocity
τ_n/τ_p : minimum electron/hole lifetimes
σ_n/σ_p : capture cross-sections electron/hole
n_1/p_1 : available electron/hole density, depending on the position of the defect, E_d
N_c/N_v : density of states in conduction/valence band
E_c/E_v : energetic level of conduction/valence band
N_d,E_d : defect density, defect's energetic level

Equations (2.2) and (2.4) highlight the fact that the defects won't contribute to the recombination process if they are located to very close to the band edges. Also, they reveal that maximum recombination occurs when $\tau_n n = \tau_p p$; if the carrier lifetimes are equal, this condition changes to the state when $n = p$.

In CIGSe, the recombination mechanisms are differentiated according to the region at which recombination occurs: (1) at the space charge region (SCR), (2) at the quasi neutral region (QNR), (3) at the back contact, (4) at the interfaces. The dominant recombination channels are mathematically extracted using the Eq. (2.1) and comparing with the general form of the voltage dependent diode current density, described in the following form:

$$J(V) = J_{00} \, exp\left(\frac{-E_a}{AkT}\right) \, exp\left(\frac{qV}{AkT} - 1\right) = J_0 \, exp\left(\frac{qV}{AkT} - 1\right) \tag{2.5}$$

where; J_0 : saturation current density
J_{00} : reference current density – weakly dependent on temperature

Table 2.1: List of recombination mechanisms in chalcopyrite solar cells and corresponding J_0 and diode quality factor. Adapted from [11, 41]

Recombination region	Recombination mechanism and defect type	Activation energy of J_0	V_{oc} (T=0 K)	Ideality factor, A
Quasi-neutral region (QNR)	Thermally activated	E_g	E_g	1
Space charge region (SCR)	(1) Thermally activated & single mid-gap defect	$E_g/2$	E_g	2
	(2) Thermally activated & exponential defect distribution	E_g/A	E_g	$1 \leqslant A \leqslant 2$
	(3) Tunneling enhanced			$2\left(1 - \frac{E_{00}^2}{3(kT)^2} + \frac{T}{T^*}\right)^{-1}$
Interface (IF)	(1) Thermally activated, single mid-gap defect (a) $\Delta E_c \leqslant 0$ (b) $\Delta E_c > 0$	 $E_{g,if}$ E_g	 $E_{g,if} \leqslant E_g$ E_g	$1 \leqslant A \leqslant 2$
	(2) Thermally activated, single mid-gap defect			$\frac{1}{\alpha}\frac{E_{00}}{kT}\ coth\left(\frac{E_{00}}{kT}\right)$

E_g : CIGSe band gap, $E_{g,if}$: CIGSe/CdS interface band gap, $\Delta E_c \leqslant 0$: cliff in the conduction band at the CIGSe/CdS interface, $\Delta E_c > 0$: spike in the conduction band at the CIGSe/CdS interface, A : diode quality factor, E_{oo} : the energy required for the transition from a thermally activated to an tunnelling enhanced recombination, α : correlation factor for the band bending at the CIGSe interface, $1/T^*$: damping of the exponential defect distribution, k : Boltzmann constant, T : temperature.

E_a : activation energy

A : ideality factor

The parameter A determines the quality of the diode and the voltage dependency of the current density. The magnitude of each recombination mechanism operating in parallel depends on the corresponding values of J_0 and A. The values for J_0 and A for the most relevant recombination mechanisms in CIGSe solar cells are tabulated in Table 2.1, following the literature [11, 41]. Detailed information is well described in the solar cell books [11, 40, 42]. The reader is encouraged to have a look at those derivations, in case of any ambiguity. Here, the discussion is confined to interface recombination.

Interface recombination

Interfaces and surfaces of semiconductors are prone to be highly defective as the crystal atoms in this region are highly perturbed due to a lattice mismatch or defect segregation, which can create a high density of defects at the interface compared to the bulk of the absorber. At the CIGSe/CdS interface, recombination is influenced mainly by their band alignment and also the conditions under which the absorber is grown. For example, it is reported that interface recombination dominates in Cu-rich samples as compared to those grown under Cu-deficient conditions [43]. Interface recombination can be lowered by a careful designing of the CIGSe/buffer interface by bringing the Fermi-level close to the conduction band at the interface. This can be done by an asymmetric doping of the CIGSe absorber and the buffer layer [37]. Also, a band-gap widening at the interface or a moderate spike at the interface can considerably reduce the interface recombination by decreasing the hole density available for the electrons coming from the CIGSe to recombine.

In the case of $\Delta E_c \leqslant 0$, the interface effective band-gap is smaller than the absorber band-gap. This would enable a cross recombination (a recombination involving holes from the absorber with the electrons from the buffer via interface defects) path increasing the recombination current. Under these conditions, assuming a single mid-band gap interface defect with no-Fermi-level pinning involved at the interface, the saturation current density and the diode quality factor heavily depends on the doping ratio of the CIGSe and the buffer/window layer. The value of A lies between 1 and 2 for $N_{D,b/w} > N_{A,a}$ or $N_{D,b/w} = N_{A,a}$ or $N_{D,b/w} < N_{A,a}$, where $N_{A,a}$ and $N_{D,b/w}$ denotes the doping of the absorber and buffer/window layer respectively. For a symmetric junction $N_{D,b/w} = N_{A,a}$, it takes the maximum value of 2. And if the junctions are highly asymmetric, $N_{D,b/w} >> N_{A,a}$ or $N_{D,b/w} << N_{A,a}$, then A = 1. The saturation current density depends readily on the distance of the Fermi level from the valence band, $E_{p,a_{if}}$. The larger the value of the $E_{p,a_{if}}$, the smaller is the J_0. Following Scheer et. al. [44], the activation energy of the saturation current density is given by $E_{g,if} = E_{g,a} + \Delta E_c$. Therefore, in the case of a cliff and flat band conditions, the activation energy is less than the absorber band gap.

$$V_{oc} = \frac{E_a}{q} - \frac{AkT}{q}\, ln\left(\frac{J_{00}}{J_{sc}}\right) \tag{2.6}$$

$$J_0 = q\ N_{V,a}\ S_p\ exp\left(\frac{-E_{p,a_{if}}}{kT}\right) \tag{2.7}$$

If the interface states are sufficient to induce Fermi-level pinning, the activation energy can be smaller than the interface band gap, which is equal to the difference between the conduction band and the Fermi-level, Φ_b^p, and A=1. The diode current activation energy for a spiked interface is equal to its band gap, which means that the recombination is lower. At the same time, the diode quality factor, A =1. The saturation current density and its impact on the open circuit voltage is shown in Eqs., (2.6) and (2.7).

Nadenau et al. and Rau et al. showed that the tunneling enhanced recombination is also affected by the SCR width [45, 46]. This modifies the saturation current density and V_{oc} equation accordingly in the following way.

$$J_0 = J_{00} exp\left(\frac{-\Phi_b^p}{\alpha kT}\right) exp\left(\frac{qV}{AkT}\right) \tag{2.8}$$

$$A = \frac{1}{\alpha}\frac{E_{00}}{kT}\ coth\left(\frac{E_{00}}{kT}\right) \tag{2.9}$$

where, $\alpha = \delta V_p/(\delta V_p + \delta V_n)$ is a parameter related to the band bending at the interface. In summary, the activation energy of the J_0 is $E_{g,if}$ in the case of $\Delta E_c \leqslant 0$ and $E_{g,a}$ in the case of $\Delta E_c > 0$ and Φ_b^p in the case of Fermi level pinning. And the tunneling at the interface does not alter the activation energy of the saturation current density.

2.5 Current-voltage characteristics

The performance of a solar cell is determined by the electronic transport mechanisms, which entirely depend upon the recombination process. The simplest tool to get some hints on recombination process is by measuring the photo-current density and photo-voltage ($J-V$ curves). Often, the $J-V$ curves in the dark or under illumination are described using a simple one diode model. The one-diode-model is an extension of the diode equation with

the saturation current density J_0 and diode quality factor A_1; the value of A_1 is related to the main recombination channel, and J_0 describes the recombination losses. In addition to the J_0 and A_1, the one-diode-model includes the ohmic losses and barriers for the current extraction by adding the voltage dependent series resistance, $R_s(V)$, and the parasitic shunt paths by the shunt resistance, R_p. It also introduces an additional current source to take account of the photo-generated current density under illumination, J_L. Figure 2.4 describes the equivalent circuit diagram of a solar cell according to the one-diode-model that follows the Eq. (2.10).

$$J(V) = J_0 \left(exp\left(\frac{q(V - R_s J(V))}{AkT} \right) - 1 \right) + \frac{V - R_s J(V)}{R_p} - J_L \tag{2.10}$$

where; R_s : series resistance
R_p : parallel resistance
J_L : illuminated current density

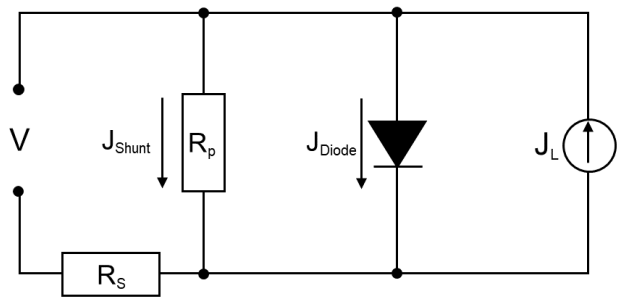

Figure 2.4: Circuit diagram of a one-diode modelled photo-voltaic cell.

The first part of the Eq. (2.10) refers to the contribution from the diode current density J_{Diode}, the second accounts for the current flowing through the shunt, J_{Shunt} and J_L stands for photo-generated current density. Although, the one-diode model serves well for describing the behaviour of solar cells, it often fails to give a perfect fit for the the $J - V$ curves, especially when A_1 is a function of voltage and temperature; hence, an extra diode, with an ideality factor A_2, and saturation current density, J_{01} is added in parallel to the first diode to gauge recombination at low voltages.

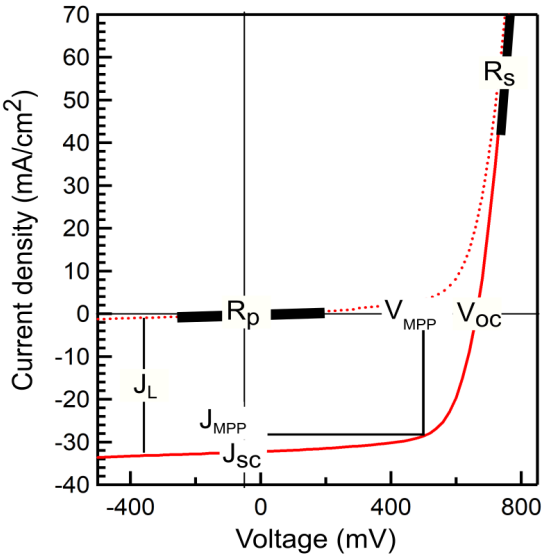

Figure 2.5: Dark (dashed lines) and illuminated (solid lines) $J-V$ curves of a standard CIGSe solar cell. The resistances R_p and R_s are measured from the dark $J-V$ curve around the voltage range marked with thick black lines, while the V_{OC}, the J_{SC}, the J_{MPP} and the V_{MPP} are measured from the illuminated curve.

Device parameters

When it comes to the performance analysis of a solar cell, mainly four parameters are of particular interest: short-circuit current density, J_{sc}, open-circuit voltage, V_{oc}, fill factor, FF, and efficiency. Figure 2.5 illustrates the dark and illuminated $J-V$ curves of a CIGSe solar cell with Cu/[Ga+In] = 0.92. Under illumination and zero-bias condition, $J(V=0)$, and assuming that J_L is voltage independent, the only current flowing through the device is the light generated current density, J_L or commonly known as short-circuit current density, J_{sc}. In the case of an open circuit condition, no current flows through the circuit $J(V_{oc}) = 0$. At this point, $R_s = 0$ and $R_p \to \infty$ and V_{oc} can be approximated as in the following Eq. (2.11).

$$V_{oc} = \frac{AkT}{q} \, ln\left(\frac{-J_L}{J_0}\right) \tag{2.11}$$

Equation (2.11) tells that the saturation current is a decisive factor in determining the open circuit voltage; the same holds for the ideality factor, too. The important parameter used to classify a solar cell is its power conversion efficiency, η, which is the ratio of the generated power, P_{out}, to the incident irradiated power, P_{in}. The generated power can be calculated by

measuring the current at different voltages and the corresponding maximum power-points can be found from the $J-V$ curves: V_{mpp}, and I_{mpp}. The ratio of the power at the maximum power point to the product of open-circuit voltage and short-circuit current is the fill-factor of the device ($FF = V_{mpp}I_{mpp}/V_{oc}I_{sc}$). Then, the efficiency is calculated using the Eq. (2.12),

$$\eta = \frac{P_{out}}{P_{in}} = \frac{V_{oc}I_{sc}FF}{P_{in}}. \tag{2.12}$$

The short-circuit current density gives the convoluted value of the photo-current produced by each photon over the entire spectrum. However, it will not reflect on the J_{sc} losses on the spectral basis. A better understanding of the recombination losses can be gained by measuring the wavelength dependent photo-current.

2.6 Quantum efficiency

An insight into the spectrally resolved photo-current can be gained from the external quantum efficiency (EQE) measurements, which measures the photo-current density as a function of wavelength of the incident light. The EQE is also a standard measurement technique to determine the device quality, as the measurement is the sum of several processes, from absorption to current extraction. It can be defined as the efficiency of a device to absorb the photons and to extract the charge carriers. In reality, short circuit current measured by EQE is always lower than the $J-V$ measurements due to its dependence on the light intensity or reflection losses or lost charge carriers in the absorber and buffer or from a non-ideal current collection. The basic equation of an EQE is expressed in the following way,

$$EQE = \frac{1}{q}\frac{dJ_{photo}(\lambda)}{d\phi(\lambda)} \tag{2.13}$$

where $d\phi(\lambda)$ is the incident photon flux in the wavelength interval $d\lambda$ that leads to the short-circuit current density, dJ_{sc}. EQE can also give the information about the regions where the losses occur in a device by making a distinction between blue response and red response. The same equation can be related to the internal quantum efficiency (IQE),

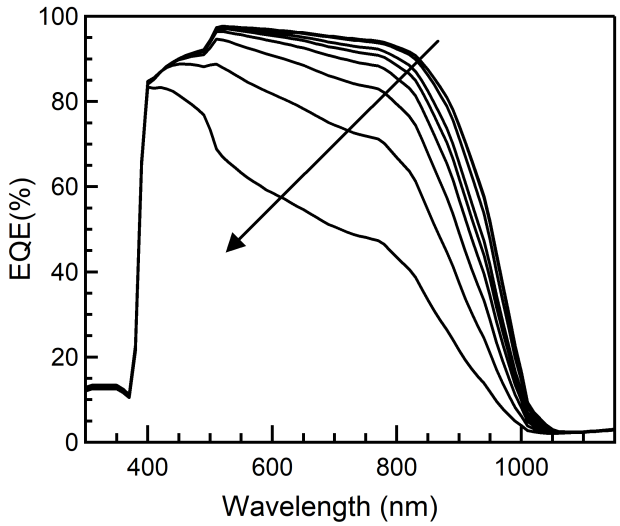

Figure 2.6: Simulated external quantum efficiencies of CIGSe absorbers in the order of decreasing thickness: 2 μm, 1.5 μm, 900 nm, 600 nm, 500 nm, 400 nm, 300 nm, 200 nm and 100 nm; the arrow shows the direction of decrease in thickness. The semiconductor parameters are according to the default values in the Table 4.1

which is a measure of the photons entering the device, i.e neglecting the reflected photons. In an opaque solar cell, the sum of absorption and reflection is unity. Hence, the EQE is related to IQE in the following way,

$$EQE = (1 - R(\lambda))IQE(\lambda) \tag{2.14}$$

This completes the short review on the basic principles of the CIGSe based solar cell devices, and the prominent recombination mechanisms; the list is not complete, but the review is kept short, only taking the aspects needed for discussing and analyzing the solar cells in the course of this work.

2.7 Review on point contacts at the CIGSe interfaces

Surface and interface engineering are inevitable for achieving high performance CIGSe thin film devices [9, 47, 48]. Theoretically, interface engineering by incorporating a suitable passivation layer at the CIGSe/CdS can significantly reduce the high surface recombination velocity [49], but a closed layer would create problems for the carrier transport between the

CIGSe and CdS layers. A concept that is used in the Si solar cell technology to surpass this problem is by applying a perforated passivation layer, provided the distance between contacts is shorter than the diffusion length. Compared to Si, the diffusion lengths in CIGSe are in the order of nanometers (300 - 900 nm) [50, 51]; this certainly demands for the structures to be in the nanometer scale, imposing limits on the conventional patterning techniques.

The concept of localized contacts at the CIGSe/CdS junction was first suggested by Allsop, et.al [49], based on 3D simulations. With a similar version, a point-junction device, Fu et. al [48] reported a slight improvement in efficiency by adding a high density of ZnS nanodots ($\approx$ 10 nm), acting as the passivating islands, before the deposition of an In_2S_3 buffer layer by ion layer gas assisted reaction (ILGAR). The potassium fluoride treatment showed indications that the efficiency in high efficiency solar cells is limited by interface recombination [9, 14, 47]. Reinhard et.al [47] reported that tuning the post deposition treatment generates localised nano-contacts on the CIGSe surface and was found to be beneficial for reducting recombination at the front interface (CIGSe/CdS) [47].

Inspired from the concept of passivated emitter and rear locally diffused (PERL) cells, Vermang et.al [52] introduced the concept of localized point contacts at the rear interface (Mo/CIGSe) of ultra-thin CIGSe solar cells through a perforated aluminium oxide (Al_2O_3) passivation layer. The approach has been successful in reducing the V_{oc} loss due to the high recombination at the rear interface when the absorber thickness is reduced. Lately, several research groups have reported this technology to be beneficial for ultra-thin solar cells, even employing conventional patterning techniques [53, 54].

However, the concept of localised point point contacts through a passivation layer, especially at the front interface, is not investigated in detail, and further development could bring an efficiency enhancement in record efficiency solar cells. Therefore, a technologically feasible point contact technique is needed to open the door for the further development of CIGSe/buffer interface.

A successful application of a point contact junction device depends on whether the device performance is limited by interface recombination or not. Hence, the selection of CIGSe samples, and their performance with a passivation layer is to be checked before the ap-

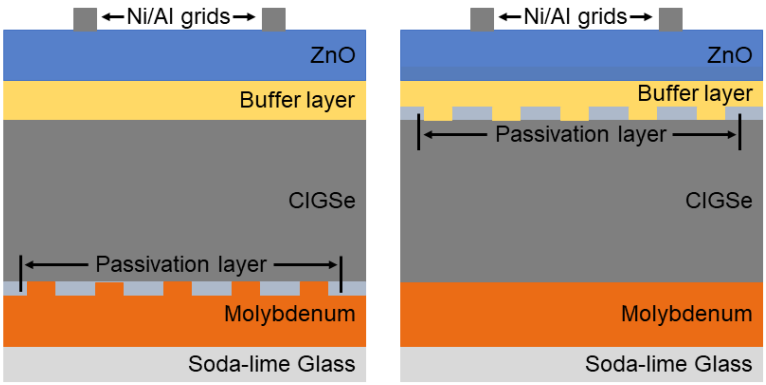

Figure 2.7: Left: Sketch of point contact configuration in CIGSe solar cells at the back interface (Mo/CIGSe); right: point contact configuration in CIGSe solar cells at the front interface (CIGSe/CdS)

plication of the point contacts at the CIGSe/buffer interface. Typically, in a type inverted CIGSe/buffer interface, the recombination is negligible at the interface due to the decreased number of available holes; hence, space charge region recombination (SCR) is found to be the dominating loss mechanism in CIGSe devices [55–57], which is contradictory to the findings from the alkali fluoride treatment [1, 9, 14, 47, 58–60]. Therefore, as a background study, we selected three stoichiometrically three different CIGSe samples: a copper–rich, [Cu/In+Ga] = 1, copper–poor gallium–rich, [Cu/In+Ga] = 0.9, and a Cu-poor, [Cu/In+Ga] = 0.92, and investigated them using temperature dependent current-voltage characterisation along with spectral and time-resolved photoluminescence.

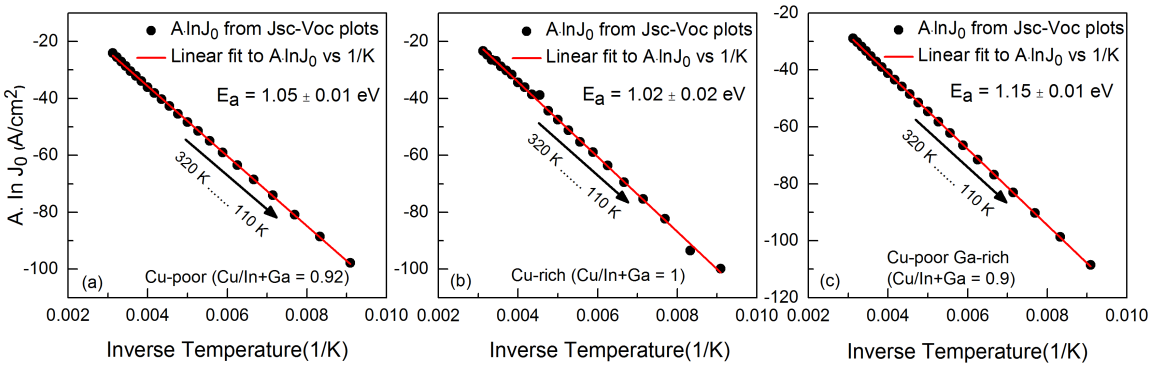

Figure 2.8: Arrhenius plots for calculating the activation energies of three different stoichometric CIGSe solar cells: (a) Cu/[In+Ga] = 0.92, (b) Cu/[In+Ga] = 1 and (c) Cu/[In+Ga] = 0.9. $A \cdot lnJ_0$ as a function of inverse temperature and the activation energy is determined by a linear regressional fitting of data points.

We chose these three stichiometrically different absorbers due to the following reasons. The electronic properties of Cu–rich absorbers — low defect density, higher carrier mobility and no potential fluctuations — are superior to Cu-poor absorbers [61–65]. But, as a device, its performance is inferior to the Cu–poor absorbers. This could be due to an absence of an ordered vacancy compound (ODC), which widens the surface band gap at the CIGSe/CdS interface, or absence of a type inverted CIGSe/CdS interface [66, 67]. With wide-band gap Ga–rich absorbers, V_{oc} does not follows a linear relation with the band-gap energies: saturation of V_{oc} has been reported for higher gallium concentrations, contrary to its expected increase. This might be due to changes at the interface with Ga-rich conditions. Lany et.al., [68] using first -principle calculation, predicted that intrinsic donor defects In_{Cu}, Ga_{Cu}, V_{Se} and their complexes with copper vacancies, V_{Cu}, could be the reason for V_{oc} limitation. And for Cu-poor absorbers, a KF treatment showed an improvement in the V_{oc}.

From the activation energies (AE) calculated, as shown in Figure 2.8, it was observed that they are close to their corresponding band gaps expect for the Cu-rich absorber (a detailed analysis is presented in Appendix C). The Cu-rich absorbers exhibited a barrier at low temperatures, but this was less pronounced in Cu-poor absorbers; this was absent in Cu-poor–Ga-rich absorbers. However, when thin layers of Al_2O_3 (5, 10, 20 nm) as passivation layer are deposited onto these absorbers and spectral and time-resolved photoluminescence measurements were performed, both photoluminescence intensity and charge carrier lifetime were enhanced for Cu-poor and Cu-rich absorbers. This might be pointing towards a interface quality improvement. The effect of passivation was least visible in Ga–rich absorbers and best visible in Cu-poor samples (for TRPL and PL analysis, see supplementary information in Appendix C). Therefore, in the chapters to follow, Cu-poor absorbers are chosen for studying the effect of point contacts at the front interface.

3

Template assisted fabrication of point contacts using self-assembled spherical CdS NP's

In order to meet the requirements for realising point contact solar cells, at the onset of this work, we tested techniques like self-assembling of polystyrene nanospheres at the air-water interface, ion layer gas reaction (ILGAR) and nanolithography (refer to Appendix B), which didn't show any promise to proceed further: to mention some of the hurdles we faced, the low diffusion length and rough surface of the CIGSe was one of the problems in implementing nanolithography, the same is true with polystyrene nanospheres. These limitations drove us to take the path of a solution based self assembly of nanoparticles; and to attain this, we modified the chemical bath deposition (CBD) method used for depositing cadmium sulphide (CdS) buffer layers in CIGSe solar cells, thus yielding mono-disperse spherical CdS nanoparticles (SNP's), which were used as a masking template for the point contact fabrication at CIGSe/buffer and Mo/CIGSe interfaces. This is the central topic of discussion in this chapter.

3.1 Approach for point contacts using monodisperse SNP's

Mono-disperse semiconductor nanoparticles (NP's) are a topic of intense research because of their versatile applications, ranging from catalysis [69, 70], quantum dot solar cells [71, 72], photo-detectors [73] and so on [74–78]. Suitability of these NP's for a particular application depends on a set of parameters like size, structure, morphology, crystalline phase and defects, and this is mainly influenced by the synthesising technique. One of the most common NP's synthesising route is the hydrothermal method, and this is same for the preparation of cadmium sulphide nanoparticles (CdS NP's) too [79, 80]. CdS, a II–VI and

an n-type semiconductor compound, belonging to this group, has above all its flexibility to adapt for various applications and also serves as the best buffer layer for CIGSe solar cells. CdS is found in nature in cubic and hexagonal structure with coordination of four cadmium to one sulphur atom [81]. Until now, self assembled spherical CdS nanoparticles (SNP's) are synthesised above 120°C [79]. In this chapter, we demonstrate a low temperature ion to ion reaction of Cd^{2+} with S^{2-} ions without the aid of any complexing agents, for a controlled rapid growth of CdS nanoparticles with narrow size distribution and its subsequent application as a template for achieving point contacts on CIGSe solar cells.

3.2 Preparation of spherical CdS nanoparticles

For the synthesis of spherical CdS nanoparticles, cadmium acetate ($Cd(Ac)_2$) ($Cd(CH_3COO)_2$. $2H_2O$) is used as the source for cadmium and the sulphur is delivered to the reacting medium from thiourea (NH_2CSNH_2). One of the reasons for selecting $Cd(Ac)_2$ as the precursor is due to its faster growth rate in reaction with thiourea as compared to other cadmium containing compounds [82]. For the preparation of CdS NP's, analytic grade reagents were brought from Sigma Aldrich and used without further purification. In a typical synthesis, 1 mmol of the cadmium acetate was mixed in 100 ml of deionised water and stirred until it gets dissolved. Then, 10 mmol of the thiourea is added to the same and kept at room temperature and waited for a complete dissolution of the thiourea. Following this, the solution was transferred to an open, double walled vessel, with water circulating through the walls at a temperature of 100°C. The solution was allowed to react for one hour. As the reaction proceeds with time, initialisation of ligand complexes and the particle formation starts to show up and this is marked by a change in transparency of the solution into a light yellowish colour. This is entirely dependent on the initial concentration of the reactants and the temperature of the water-bath. Here, this transformation is visible after eight minutes of reaction. However, the solution is allowed to react further, to increase the density of the particles by simply evaporating the solution. When the desired concentration of particles is reached, CIGSe substrates, etched with 5% solution of potassium cyanide (KCN) to clean out any secondary phases or other contaminants [83], are successively dipped into the colloidal solution, followed by washing with water, each time, thus cleaning out the excess CdS SNP's that may alter the mono-layer formation. This process is continued until the desired density of a two-dimensional layer is formed on top of the CIGSe

substrate. The interval between coating and dipping in this case is fixed to be 30 s, but this timing is varied for other temperature processes, due to different deposition rates of NP's.

3.3 Structural properties of spherical CdS nanoparticles

The formation of CdS nanospheres obtained hydrothermally at 100°C with a starting ratio of 1:10 to ($Cd(Ac)_2$):thiourea is presented on Figure 3.1. A closer look at the SEM images shows that the nanospheres are mono-dispersed and have a narrow size distribution around 120 nm with an uncertainty of $\pm$ 5 nm. It can be also seen that the spherical surface is not smooth and is constituted from small nanocrystallites. The nanocrystallines formed in this case are approximately in the range of 25-40 nm. There was no indication of a change in the morphology of the nanospheres when the reaction time is increased, but it was certainly dependent on temperature of the water bath. Figure 3.2 shows the X-ray diffraction

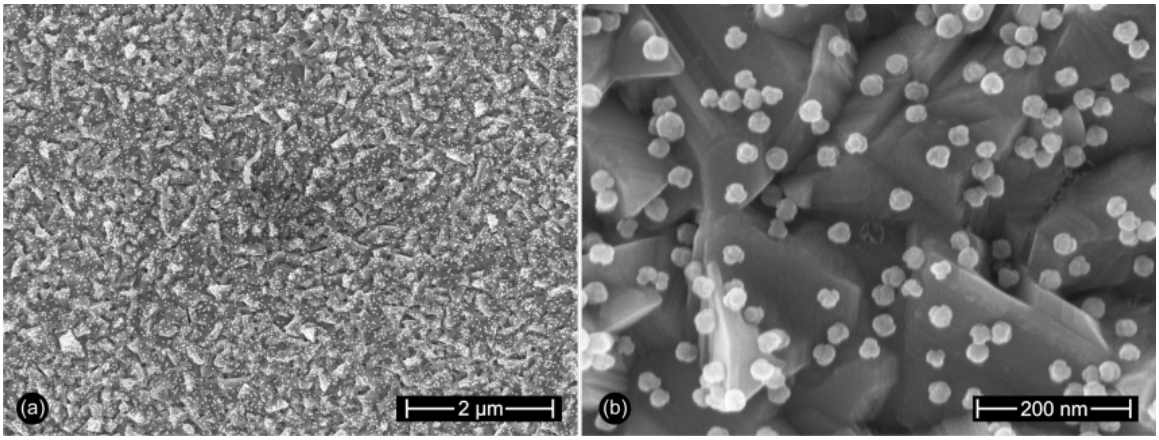

Figure 3.1: SEM images of the cadmium sulphide nanoparticles on the top of CIGSe samples synthesized with starting ratio of ($Cd(Ac)_2$):thiourea, 1:10

pattern of CdS NP's synthesized at 100°C with starting ratio of ($Cd(Ac)_2$):thiourea, 1:10. The sharp peaks in the X-ray diffraction patterns have revealed a good crystalline quality of the nanoparticles and the peaks are indexed to the hexagonal phase of the wurtzite CdS structure (JCPDS card No. 75-1545) with lattice constants a = 4.137 Å and c = 6.7144 Å. Another thing to notice is that the nanospheres grew preferentially in (002) reflection direction.

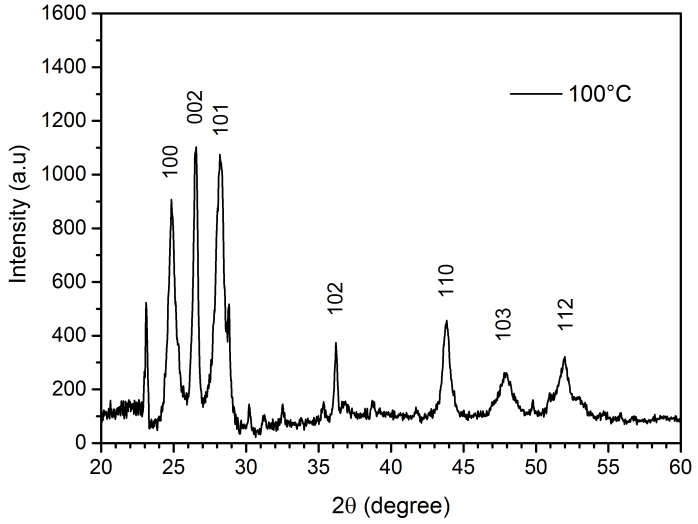

Figure 3.2: X-ray diffraction patterns of the cadmium sulphide nanoparticles synthesized at 100°C with starting ratio of $(Cd(Ac)_2)$:thiourea, 1:10.

3.3.1 Formation mechanism of spherical CdS nanoparticles.

It is believed that for the ion to ion reaction of Cd^{2+} with S^{2-} reaction to take place, a high temperature hydro-thermal reaction is necessary, which is published elsewhere [79, 80]. The formation of nanospheres in this work can be attributed to the spontaneous Ostwald ripening process [84]. In the underlying reaction, the electroneutral ligand, thiourea forms complexes with Cd^{2+} cations through $\mathrm{C}{=\!=}\mathrm{S}$ coordination bonding. It should be noted that no coordinating reagents were present in the reaction medium, in contrast to the NH_4OH, a complexing agent used in chemical bath deposition of CdS. So, the formation of nanocrystallites and its subsequent nanosphere formation points to the double agent role played by thiourea, facilitating the formation of Cd^{2+} ligands by acting as the complexing agent and also as the source of sulphur, once the double bond between $\mathrm{C}{=\!=}\mathrm{S}$ is broken by the attack of strong nuceophilic oxygen atoms from the water molecules. The scheme of the reaction is described below.

$$Cd(L)_n^{2+} \longrightarrow Cd^{2+} + nL \tag{3.1}$$

$$SC(NH_2)_2 + 2OH^- \longrightarrow S^{2-} + CN_2H_2 + 2H_2O \tag{3.2}$$

$$Cd^{2+} + S^{2-} \longrightarrow CdS(s) \tag{3.3}$$

Sulphide ions are released by the hydrolysis of thiourea and cadmium ions by the decomplexation reaction, here L represents the ligand species, which in our case is OH^- or thiourea complex. Since the concentration of thiourea in the reaction medium exceeds $Cd(Ac)_2$, Cd atoms on the surface of CdS nanocrystallites could be coordinated with the excess of thiourea. The constitution of nanocrystallites into nanospheres minimises the surface energy, and arrests agglomeration of the particles. This conclusion can be ex-

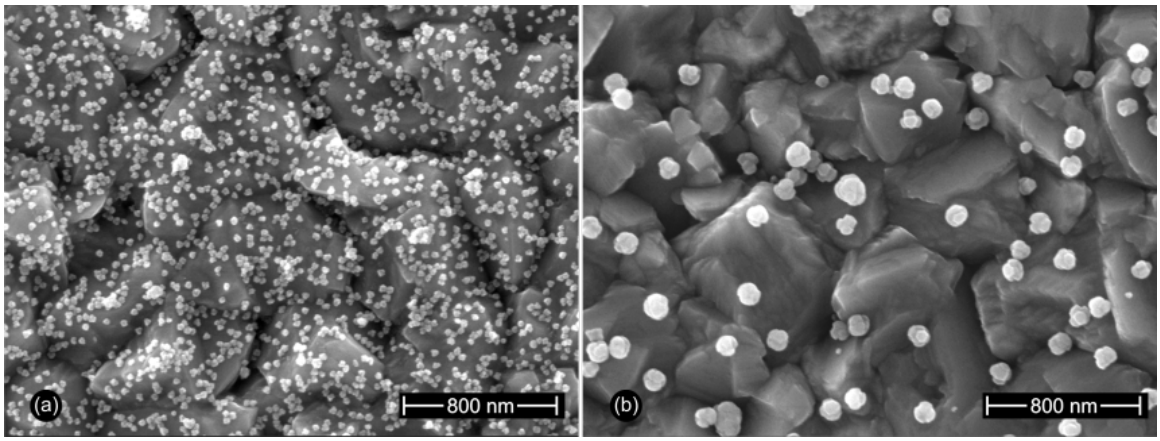

Figure 3.3: A comparison of the nanospheres synthesised with and without the addition of PVP in the solution (a) with PVP (b) without PVP; both cases have the same starting ratios: $Cd(Ac)_2$:thiourea (1:10).

plained further by the use of a stabilising agent for hindering the constitution process. For this we use polyvinylpyrrolidone (PVP) and observed that thermodynamically, it promotes a more favourable arrangement by minimizing the surface energy of nanocrystallites. Figure 3.3 shows a comparison between the sizes and morphology between a process with $Cd(Ac)_2$:thiourea (1:10) and that with the inclusion of PVP in the reaction medium. The small nanocrystallities are better for the application of point contacts, but the organic layer they have is detrimental for the performance of the solar cell.

3.3.2 Impact of temperature and concentration on CdS SNP's growth

Our primary aim was to synthesis CdS nanoparticles without any stabilising agents in the sub-micrometer range, keeping the diffusion length of the CIGSe in mind. Once we reached our first goal, we tried whether it is possible to tune the particle size smaller by simply changing the parameters of the reaction: temperature of the water bath and precursor concentration. By keeping the reaction temperature (100°C) and $Cd(Ac)_2$ concentration constant, we varied the thiourea concentration to study its effect on the particle size and growth rate. For this, we took two thiourea concentrations 1:5 and 1:20, on either side of the typical process (1:10) concentration.

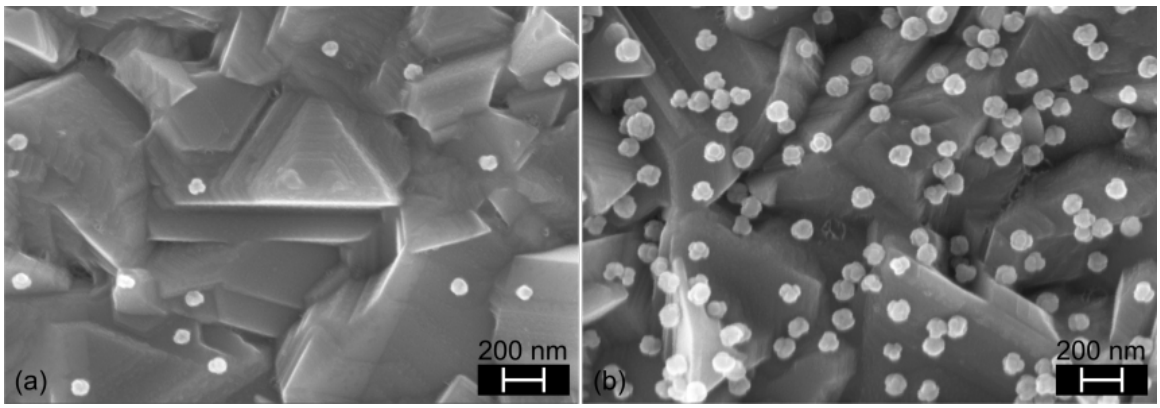

Figure 3.4: SEM images showing the size comparison of the cadmium sulphide nanoparticles on the top of CIGSe samples synthesised with starting ratio of ($Cd(Ac)_2$):thiourea, 1:10, at 80°C (left) and 100°C (right).

Figure 3.4 shows the SEM images of CdS NP's synthesized at 80°C and 100°C for the same starting ratio of ($Cd(Ac)_2$):thiourea, 1:10. The image is clearly differentiated for the density of the nanoparticles on the CIGSe surface for an equal dipping time (30 s each) of four times. When thiourea is increased in the reacting medium, the growth rate of the particles is primarily affected. This is due to the fact that more sulphur is released to the solution, but the particle size stayed the same. However, the particle size got affected as we changed the temperature from 100°C to 80°C. A minimum of 45 nm particle radii is obtained at the lowest temperature possible for the particle formation. One thing to notice is that the reaction rate is much lower because of the lower decomposition of thiourea and further decrease in temperature, which didn't yield any particles at all.

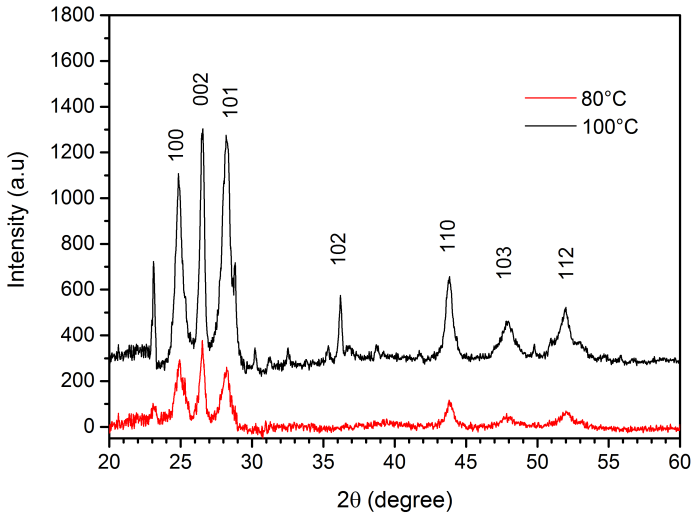

Figure 3.5: X-ray diffraction patterns of the cadmium sulphide nanoparticles synthesised at 80°C and 100°C with starting ratio of $Cd(Ac)_2$:thiourea (1:10).

The temperature also affects the crystallinity of the particles as shown in Figure 3.5. On increasing the temperature from 80°C to 100°C, the sharpness of peaks spikes up, which is a general measure of crystalline quality of the particles. This is due to the fact that at higher temperature thiourea helps a faster growth rate of nanocrystals, making them bigger in size by initiating the reaction earlier and allowing the particle to recrystallise.

3.3.3 Impact of substrate's roughness on CdS SNP's self-assembling

The roughness of the substrates is a key parameter when it comes to the self-assembling of CdS NP's. CIGSe is well known for its surface roughness. This can create some preferable sites for (acting like templates for attracting particles) landing the particles — especially at the facets or even at the grain boundaries. The difference can be easily deciphered when a smooth surface like molybdenum is employed for the adhesion of the particles: we witnessed a greater arrangement of the particles on a Mo substrate. The SEM images shown in Figure 3.6 clearly show the difference between the two.

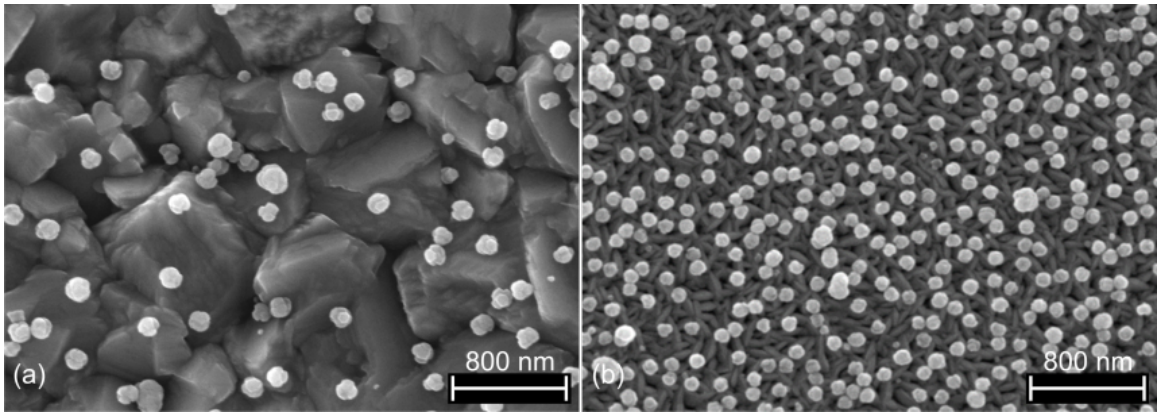

Figure 3.6: A roughness comparison with a smooth molybdenum surface (right) against the CIGSe surface (left), showing the dependence of roughness on arrangement of nanoparticles.

3.4 Coverage area of CdS SNP's on CIGSe

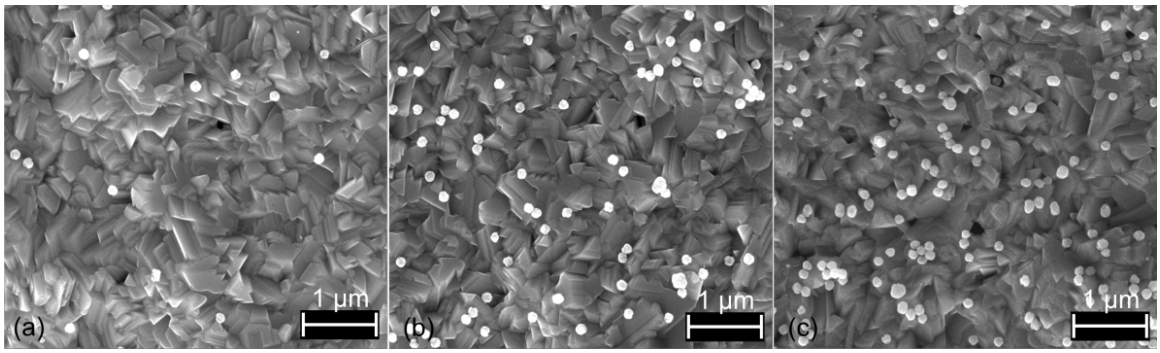

Figure 3.7: Density of CdS NP's on CIGSe surface as a function of dipping cycles of 30 s each; (a) 1 dip, (b) 3 dips, and (c) 6 dips.

The nanospheres fabricated by the process of chemical bath deposition are suited for the application of point contacts: their sizes are in the sub-micrometer range, and moreover, their radii can be tuned. But, for point contacts what is more interesting is the distance between the particles, or in other words, the density of the particles on the CIGSe surface. The monolayer assembly on the surface follows a random ordering of the particles, making it difficult to change the pitch between the particles. So, statistically, density is the only parameter that can be tuned to change the distance between the particles. Also, when a passivation layer is implemented and if it works under the concept of inversion, this parameter gains even more significance because according to theory, as the minority carriers reach the passivation layer, they become the majority carriers, extending their lifetime.

Then, the diffusion length restricted distance between the nanoparticles can be called into question.

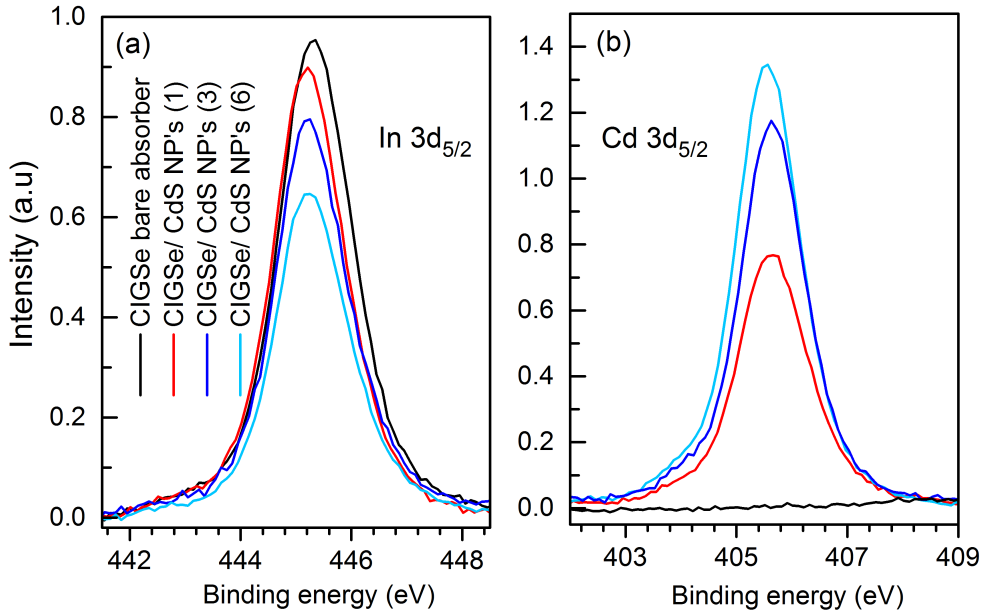

Figure 3.8: Normalized XPS peak of In $3d_{5/2}$ and Cd $3d_{5/2}$ obtained from the surface of CIGSe absorbers without CdS NP's deposition (reference), CdS NP's deposition for 1 cycle (each cycle is 30s each), 3 cycles and 6 cycles.

Table 3.1: Approximate percentage of area covered by CdS NP's on CIGSe surface for different cycles as described in Figure 3.8, calculated by taking the fitted area covered by In $3d_{5/2}$ and Cd $3d_{5/2}$ peaks.

Dipping cycles	Peak area (In $3d_{5/2}$) (CPS · eV)	Coverage area of CdS NP's (%)
0	1.13×10^5	0
1	1.05×10^5	7
3	8.44×10^4	25.4
6	5.78×10^4	49

Figure 3.7 shows the density of the CdS NP's on the CIGSe surface as a function of the dipping cycle of 30 s each. One way to quantify the coverage area of these CdS NP's on CIGSe is by using an image processing software (like ImageJ) and counting the number of particles. Another way is to use XPS. This surface sensitive technique gives the collective information of the elements present on the surface. Figure 3.8 shows the XPS spectra of the In $3d_{5/2}$ and Cd $3d_{5/2}$ peaks for different densities of CdS NP's. In an XPS spectrum of a bare CIGSe absorber, In $3d_{5/2}$ has the highest intensity. On covering the surface with

CdS NP's, the intensity of In peaks gets reduced as the Cd concentration increases (refer to Figure 3.8 (b)), and this reduction can be transferred into the coverage area by simply calculating the new area of the In $3d_{5/2}$ peaks and calculating the difference from it from the In reference curve, assuming that the reduction is constant for all core-level peaks. Table 3.1 displays the approximate percentage of the area covered by CdS NP's, for different number of dipping cycles, calculated by taking the corresponding Voigt area of the In $3d_{5/2}$ peaks.

3.5 Steps involved in point contacts fabrication

The CdS NP's are synthesised for considering them as a sacrificial template for the fabrication of point contacts at the front interface of the CIGSe interface. Based on the synthesis, we found that it was easy to control the deposition rate of the CdS NP's at 100°C with $Cd(acac)_2$:thiourea in the ratio 1:10. An increased concentration of thiourea beyond this can lead to agglomeration of particles while transferring to CIGSe surfaces. Thus, we fixed this as the standard process in all experiments to follow. Figure 3.9 illustrates the four main steps involved in the realisation of point contacts in this work. The first two steps are already discussed in sections 3.2 and 3.3.

1. Etching of the bare CIGSe using KCN (Figure 3.9 (a)).
2. Depositing CdS NP's on top of CIGSe (Figure 3.9 (b)).
3. Depositing a suitable passivation layer (Figure 3.9 (c)).
4. Etching out of the CdS NP's (Figure 3.9 (d)).

The third step is the deposition of the passivation layer. The prototype material chosen as the passivation layer (PaL) is aluminium oxide (Al_2O_3). In our trial runs, we used a low cost and fast method of depositing Al_2O_3 using the ILGAR technique. In this deposition technique aluminium acetate is chosen as the precursor, which is dissolved in ethanol and using an ultrasonicator the aerosol formed is guided through glass tubes to the substrate heated to a temperature of 400°C. However, the technique turned to be a failure due to lack of directionality and coverage for very thin films, thus making it difficult to etch out CdS

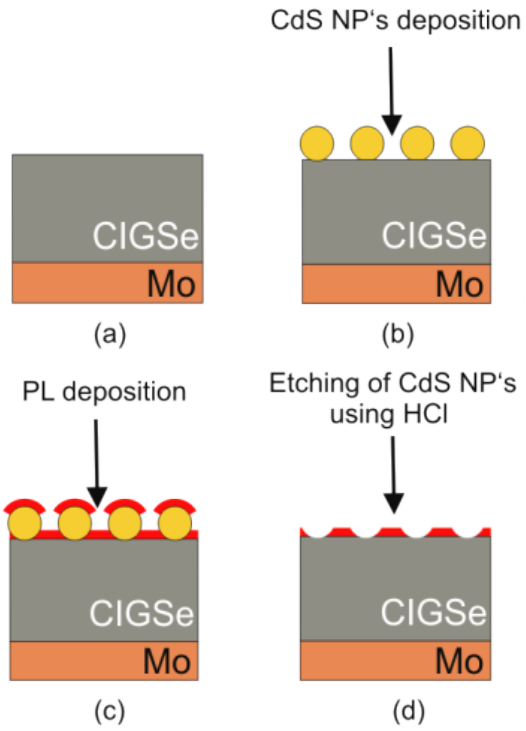

Figure 3.9: Schematic diagram showing the steps involved in the fabrication of point contacts (a) bare absorber, (b) after deposition of CdS NP's, (c) passivation layer (Al_2O_3) on top of nanospheres, (d) after etching of CdS NP's.

NP's (refer to Appendix). Another drawback was heating CIGSe at 400°C might degrade the material quality and enhance the diffusion of cadmium. To override these shortcomings, we chose atomic layer deposition of Al_2O_3.

3.5.1 ALD deposition of Al_2O_3 as passivation layer

Atomic layer deposition (ALD) has been considered as a promising technique for creating high-quality uniform thin films with control over thickness and composition. In this work, Al_2O_3 is deposited on top of CdS NP's by using a TFS500 system from Beneq having a temperature range of 25-500°C. The typical route followed for the deposition is using the precursors trimethylaluminium (TMA) and water vapour (H_2O). The reaction chamber is equipped with resistive metal plate heaters to heat up a loaded substrate. Trimethylaluminium, an aluminium precursor, was kept at a constant temperature (25°C) using a heated metal enclosure. The deposition temperature is maintained at 130°C. ALD of Al_2O_3 was

carried out in a hot-wall flow-type reactor from the sequential pulses of TMA(98% , Aldrich) and H_2O. The seed layer is formed by a 1 ms pulse time for TMA, 5 s purge using nitrogen, N_2 and then 750 ms pulse time for water vapour, followed again by purging with N_2 for 6 s. This cycle is continued until the desired thickness is reached. The rate of growth of the film on the CIGSe surface is 1 nm/10 cycles. The thickness measurements were done with ellipsometry. Different thicknesses of Al_2O_3 were tested to find the best thickness for the passivation layer. The thickness selected for this study are 5 nm, 10 nm and 15 nm. The high directionality of Al_2O_3 helps to deposit Al_2O_3 only on the area unmasked by CdS NP's, without any pinholes formation, making it easy for the fabrication of the point contacts.

3.5.2 Etching process of the CdS NP's

The next step involved in the process of making point contacts is etching out the CdS NP's. A suitable etching solvent is needed for selective etching of CdS by keeping Al_2O_3 intact with CIGSe surface. In CIGSe etching chemistry, hydrochloric acid (HCl) is widely used as an etching solvent for studying the interface between CIGSe and CdS. Taking this into account, we found an optimum method to dissolve CdS NP's and followed the protocol for the rest of the experiments.

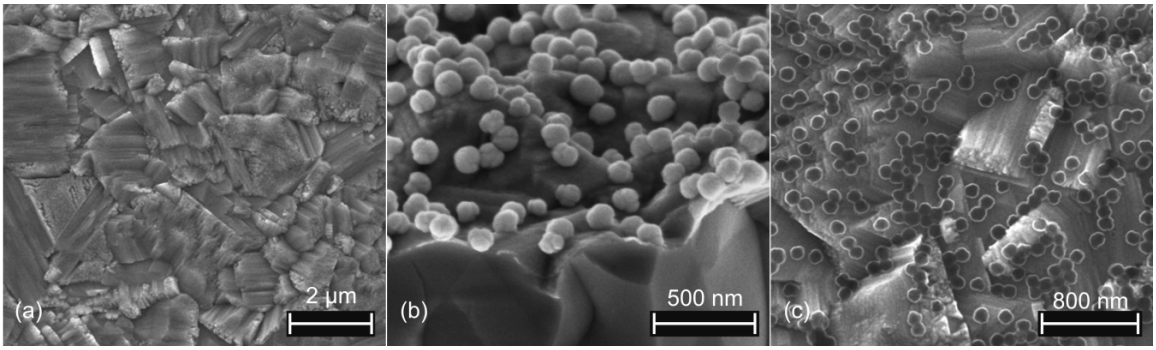

Figure 3.10: Realization of the schematic diagram shown in 3.9 (a) CIGSe bare absorber, (b) CIGSe absorber with CdS nanoparticles and 10 nm of Al_2O_3 deposited on top of it, and (c) establishing perforated Al_2O_3 layer after etching CdS NP's with HCl solution.

For etching, a 5% HCl solution is prepared in a beaker and placed in an ultrasonic bath at 40°C. By raising the temperature to 40°C, the HCl solution can diffuse through the Al_2O_3, in case it covers the CdS. The samples are treated in the solution for approximately 5 minutes.

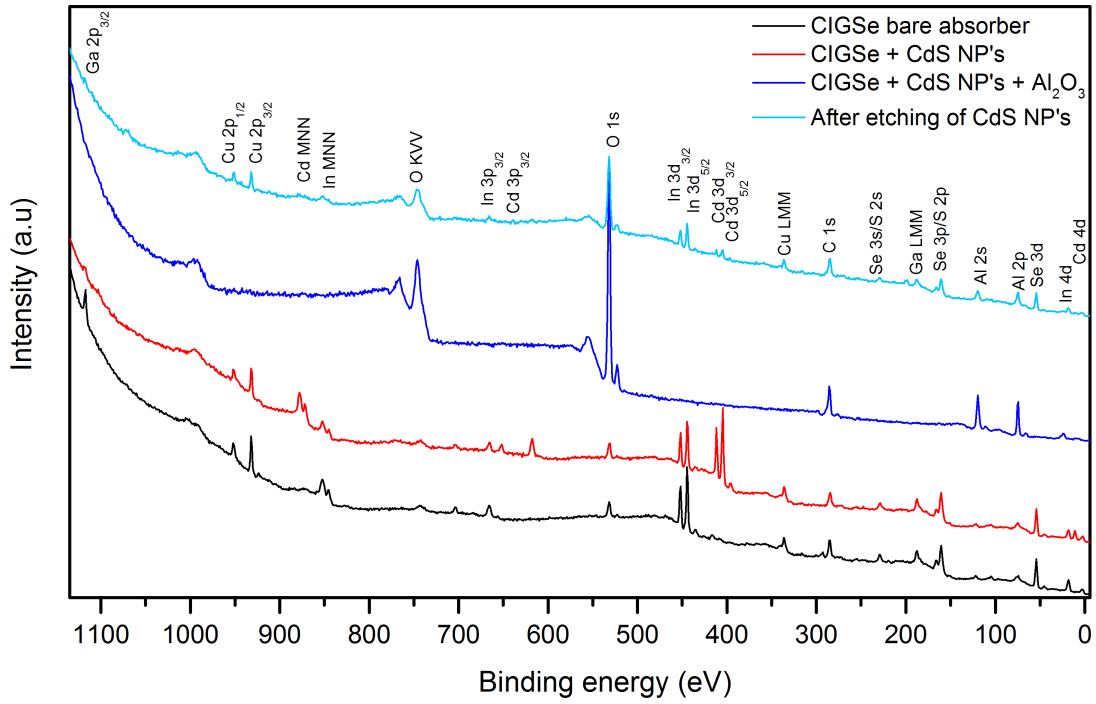

Figure 3.11: XPS spectra corresponding to the steps involved in point contacts fabrication presented in Figure 3.9, measured using a Mg Kα X-ray source.

Then they are transferred to a solution of 0.1% HCl: this intermediate step is followed to avoid any sudden changes to the surface while transferring from an acidic medium to a neutral medium. This was followed by washing the samples with deionized water and drying with a nitrogen blower. Figure 3.10 (c) shows the SEM images of the formation of point contacts on CIGSe surface before and after etching with HCl. The white glow around the circles is due to the edge effect. Because of the topographical change around the nano-contact and the passivation layer, Al_2O_3, an enhanced emission of electrons results in brighter regions around the circumference of the point contacts. To be clear about the point contact formation, the samples are also investigated using XPS, and corresponding XPS spectra are shown in Figure 3.11, which clearly shows the removal of CdS NP's during the etching process, and the return of core-level peaks establishes the point-contact formation on CIGSe surface.

3.6 Coverage area of point contacts/PaL on CIGSe

The estimation of the coverage area of point contacts or PaL using XPS and ImageJ is discussed in the section 3.4. An approximate area of the passivation layer can also be calculated from section 3.4 by subtracting the CdS NP's coverage from the unity coverage area of Al_2O_3, before the CdS NP's removal. Here, we also use XPS and try to approximate the passivated area/point contact area for different densities of point contacts on CIGSe corresponding to a different number of cycles of CdS NP's deposition. Figures 3.12 (a) – (d) show the corresponding SEM images of point contacts formation for 1, 2, 4, 6 dipping cycles. These point contacts can even handle CIGSe samples with low diffusion length, because it can be clearly seen than the distances between the point contacts are smaller in the case of 6 cycles of dipping in CdS NP's solution.

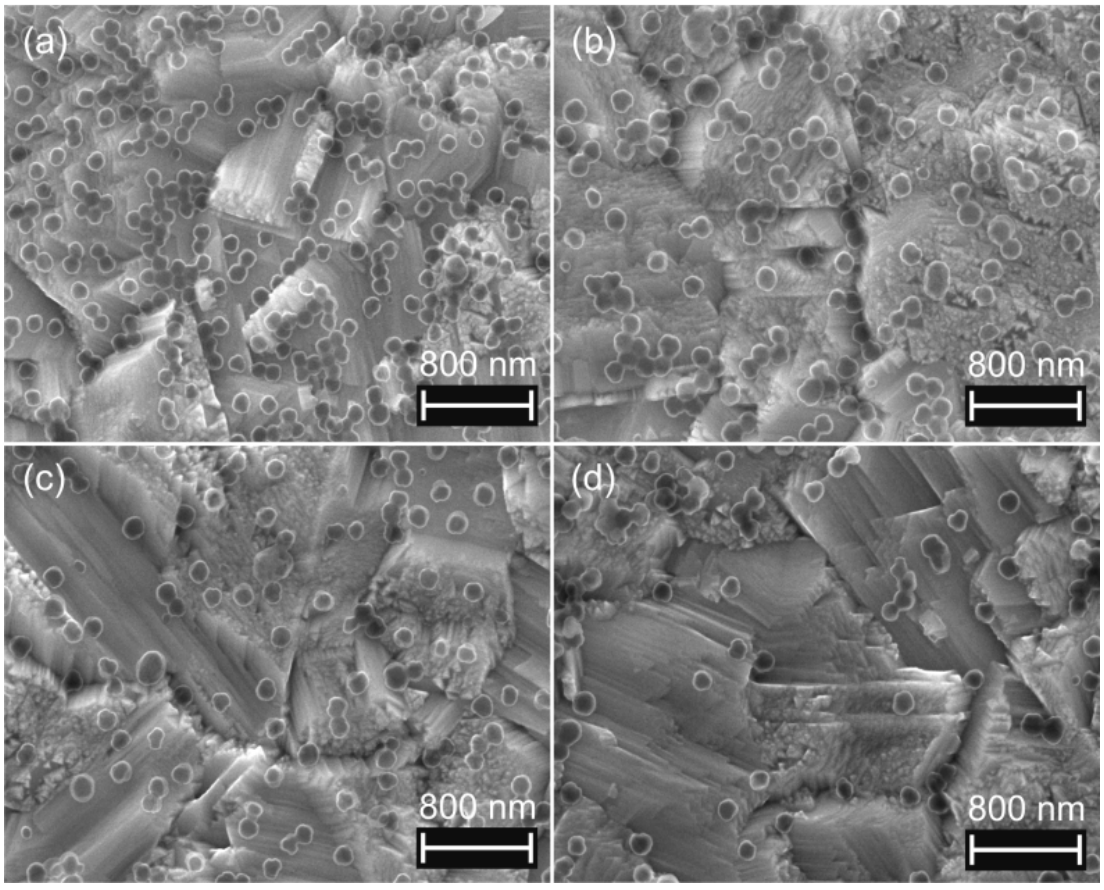

Figure 3.12: SEM images of point contacts on CIGSe illustrating the variation of their density as a function of dipping cycles; (a) 6 cycles, (b) 4 cycles, (c) 2 cycles and (d) 1 cycle.

Figure 3.13 shows the XPS spectra of Al 2p peaks measured using a Mg $K\alpha$ source in the order of decreasing density of point contacts as shown in Figure 3.12: 6, 4, 2 and 1 cycles, before and after the etching of CdS NP's. The intensity of the Al 2p peaks is proportional to the amount of Al atoms present on the CIGSe surface. Also, the thickness of Al_2O_3 is 10 nm, and from the Figure 3.11, it can be observed that no core-level peaks from CIGSe were visible after the deposition of Al_2O_3. Thus the reduction in the Al 2p peak integral can be analysed quantitatively and translated into point contacts/PaL area. Al 2p peaks were fitted using Voigt peak shapes and corresponding areas are tabulated in Table 3.2. It can be observed that the point contact/PaL area is proportional to the number of dipping cycles in the CdS NP's solution, and the area estimation using the ImageJ software also correlates with the XPS calculations.

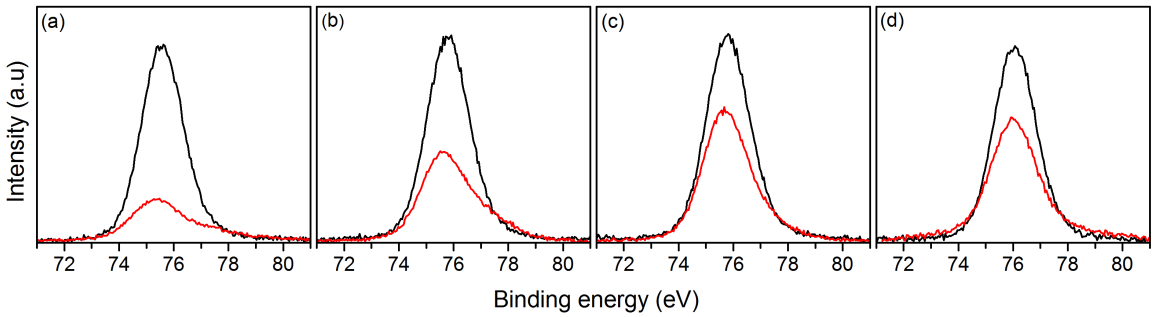

Figure 3.13: XPS spectra showing the Al 2p peaks, corresponding to the dipping cycles presented in Figure 3.12 in the decreasing order: (a) 6 cycles, (b) 4 cycles, (c) 2 cycles and (d) 1 cycle, before (black curve) and after (red curve) the removal of the CdS NP's using HCl.

Table 3.2: Approximate percentage of area covered by point contacts/PaL(Al_2O_3) on CIGSe surface for different cycles as described in Figure 3.13, calculated by taking the fitted area covered by Al 2p peaks.

Dipping cycles (no)	Al 2p area before/after etching (CPS · eV)	Coverage area (ImageJ) (PC/PaL)(%)	Coverage area (XPS) (PC/PaL)(%)
1	1.08 $\times 10^5$/9581	7.6/92.4	11.3/88.7
2	9076/7533	9.4/91.6	17/83
4	1.09 $\times 10^5$/8186	16/84	23/77
6	1.12 $\times 10^5$/6947	28/72	39.4/60.6

Furthermore, to see whether the interface quality has improved, time-resolved photoluminescence (TRPL) spectra were recorded for CIGSe absorbers with point contacts as illustrated in Figure 3.12 and were correlated with a bare CIGSe absorber and CIGSe absorber with Al_2O_3 layer on top. Figure 3.14 shows the TRPL spectra of all samples measured at

room temperature. A bi-exponential function, $I(t) = A_1 \cdot exp(-t/\tau_1) + A_2 \cdot exp(-t/\tau_2)$, describing superposition of two recombination processes with lifetimes τ_1 and τ_2, is used for fitting the TRPL curves. The fit values are listed in Table 3.3. Here, the parameter τ_2 is inversely proportional to the non-radiative recombination and hence to the interface quality [85]. The values of τ_2 and the average carrier lifetime in the Table 3.3 suggest that there is a clear improvement in the carrier lifetime of the absorbers due to the Al_2O_3 layer and point contacts compared to reference CIGSe bare absorbers. Moreover, there exists a decreasing trend in the carrier lifetime in relation to the coverage area of the Al_2O_3 layer or the point contact density.

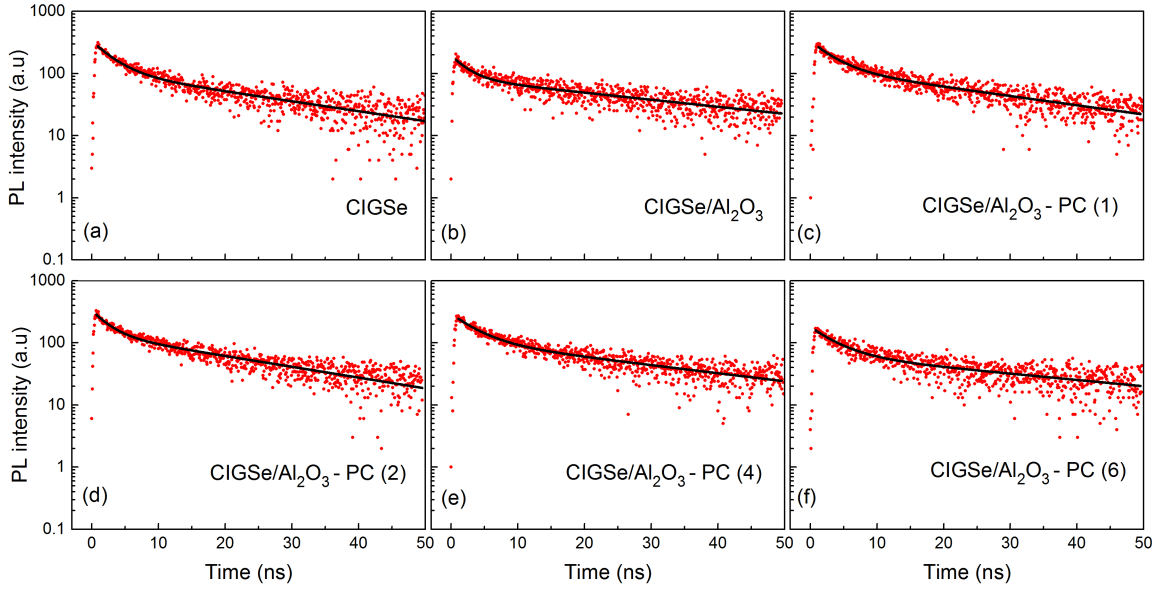

Figure 3.14: PL decay curves of the CIGSe samples with point contacts shown in Figure 3.12 (a) CIGSe bare absorber, (b) CIGSe absorber with Al_2O_3, (c) CIGSe/Al_2O_3–PC (88.7%), (d) CIGSe/Al_2O_3–PC (83%), (e) CIGSe/Al_2O_3–PC (77%), and (f) CIGSe/Al_2O_3–PC (60.6%)

Table 3.3: Summary of the TRPL data obtained for samples shown in Figure 3.14 in the same order; a bi-exponential curve is used to fit the TRPL decay: the black lines in Figure 3.14 represents the corresponding fit.

Sample	τ_1 (ns)	τ_2 (ns)	A_1	A_2	Average carrier lifetime $\frac{A_1 \cdot \tau_1^2 + A_2 \cdot \tau_2^2}{A_1 \cdot \tau_1 + A_2 \cdot \tau_2}$ (ns)
CIGSe	3.07	26.7	227.9	109.24	22.12
CIGSe/Al_2O_3 (100%)	3.35	41.29	94.35	78.19	37.90
CIGSe/Al_2O_3-PC (88.7%)	3.97	42.86	116.72	64.34	37.26
CIGSe/Al_2O_3-PC (83%)	3.80	33.46	187.01	107.37	28.55
CIGSe/Al_2O_3-PC (77%)	3.03	29.82	157.40	99.18	26.10
CIGSe/Al_2O_3-PC (60.6%)	3.04	32.67	144.69	82.81	28.52

3.7 Summary

In this chapter, a low temperature method is designed for producing monodispersed CdS nanospheres. The nanospheres are formed from the constitution of small nanocrystallites by the mechanism of the Ostwald ripening process [84]. The obtained particles, using precursors cadmium acetate and thiourea, show a hexagonal phase and have radii of 45 nm and 60 nm. The size is dependent on the temperature of the water bath, and it decreases as the temperature goes down. The growth rate of particles was dependent on the initial concentration of thiourea. The roughness of the CIGSe surface is another factor which influences the ordering of CdS NP's on the CIGSe surface. A maximum of 40% coverage area, the parameter of interest concerning point contacts, is calculated using XPS—realising any value beyond that may enhance agglomeration.

The size of the CdS particles is suited as a masking template for creating nano-point contacts on CIGSe surface . For realizing point contacts, 5 nm, 10 nm and 15 nm of Al_2O_3 are deposited using atomic layer deposition. A thickness beyond 15 nm is not chosen as it can work against the etching process of CdS NP's and also, this could increase the series resistance when the whole device is fabricated. Using 5% HCl solution, a suitable etching process was devised for removing CdS NP's and hence the point contacts are fabricated. Moreover, the density of the point contacts is varied and correspondingly different passivated coverage areas are attained, making the technology suitable for even CIGSe samples with low diffusion length. Further, TRPL measurements on these samples showed an increase and a dependence of coverage area on the charge carrier lifetime.

4

Simulation of point contact junctions at the CIGSe/buffer or Mo/CIGSe interface

In a hetero-junction solar cell like CIGSe, introducing point junction contact at CIGSe interfaces (CIGSe/buffer of 2 μm thick or Mo/CIGSe interfaces of thinner absorbers) influences a set of parameters — starting from electronic properties of the passivation layer, interface properties like band alignment, interface recombination, defect density, passivation layer thickness, surface recombination velocity, coverage area of passivation, point contact junction radius— determines the conversion efficiency. Attempting to tune any one of these, keeping the other parameters constant, perturbs the whole system, which sways the device performance positively or negatively. Controlling all these elements in an experiment will be difficult; on the other hand, studies employing computer simulation give an extra degree of freedom to change the parameters and to visualise their effects on the device performance. In this chapter, we theoretically monitor the effect of the passivation layer and point contact junctions at the CIGSe interfaces in order to understand their prospects and limitations on the device performance.

To address this problem, we took the help of two finite element method (FEM) based softwares: SCAPS, developed at the university of Gent [86], a one-dimensional software exquisitely used for simulating CIGSe solar cells and the two/three-dimensional WIAS-TESCA [87], developed at the Weierstrass-Institute für Angewandte Analysis und Stochastik. The simulated solutions of point contact junctions are the topic of discussion of this chapter.

4.1 Simulation model and input parameters for CIGSe devices

The transport of charge carriers in a p-n junction is described by a system of drift-diffusion equations. A real solution to these kind of partial differential equations (PDE's) is often unattainable by analytical methods. In these scenarios, a useful mathematical tool is the finite element analysis. The philosophical approach of FEM is rather simple. Instead of taking the problem as whole, FEM divides the problem into smaller fragments, and approximate equations are modelled for them and then they are assembled into a larger set of equations that models the entire problem [88]. Finally, using calculus of variations and by minimising the error function, an approximate solution is reached. SCAPS and WIAS-TESCA take advantage of FEM to solve the system of drift-diffusion equations.

SCAPS is a custom based open source software used extensively in thin-film solar cells research [86]. It is equipped with a wide range of simulation options for CIGSe solar cells. One can include absorption profiles of the materials, spectra, contact properties, interface recombination, series and shunt resistance that the WIAS-TESCA software is unable to handle. However, its application is restricted to one-dimensional problems.

On the contrary, WIAS-TESCA can solve the equations with two space variables as well as three dimensional models with the aid of a cylindrical symmetry [87]. The research code is written in Fortan and features less options compared to SCAPS, for example, the surface recombination is simulated using thin layers with high volumetric defects. In addition to this, the meshing is controlled by the users which could create convergence problems and at the same time gives the benefit of defining the area of particular interest in the simulation for better accuracy of the solution [87]. In the simulation, as we are interested in the developments close to the interface, meshing is made considerably denser in this region, about 3000/10000 points.

For simulating the bulk and interface recombination, we followed the recombination model (recombination of electrons and holes through the mechanism of trapping in the forbidden energy gap) formulated by Shockley, W. T. Read and R. N. Hall [40] (refer to Eqs., (2.2), (2.3) and (2.4)).

Due to the limitation in WIAS-TESCA to add the AM 1.5 spectrum to the computation, current density (J-V) graphs are executed with a single wavelength of 650 nm with its corresponding intensity, 83.1 mW/cm^2. Since two applications are employed in this work, a calibration between them was done to reduce the error in the simulation. We achieved this target by setting the SCAPS as the baseline for the WIAS-TESCA, by matching results with a cell without a passivation layer (PaL). Having said that, we would like to point out some factors we didn't take into consideration; neither reflection losses nor optical losses by the cell with and without the PaL, assuming that the high band gap PaL will not absorb any light. In addition, the series resistance of the PaL is also not taken into account. Now, the question is what happens if the PaL covers grain boundaries, since there were several reports on grain boundary assisted photo-current collection in CIGSe solar cells [89, 90]. Theoretically this is a valid question, but when realising point contacts in reality, it is impossible to control whether the PaL covers it or not, because point contacts are created by a random arrangement of particles in the sub-micrometer scale, as demonstrated in Figure 3.12.

4.2 Point contacts at CIGSe/buffer interface

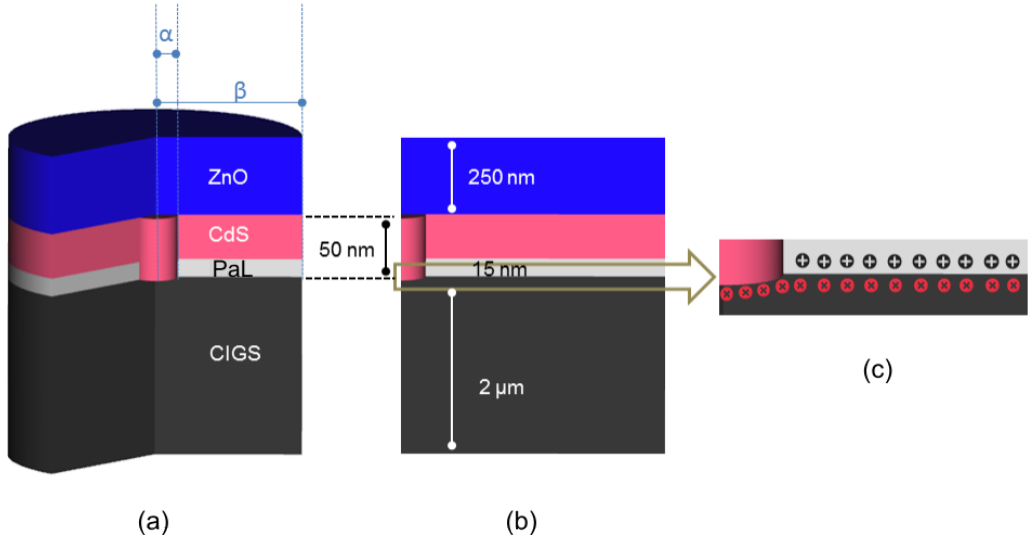

Figure 4.1: Three-dimensional diagram of a point-contact CIGSe solar cell: α is the variable point-contact radius, variable, β represents the cell radius, which is constant at 500 *nm*. (a) Three-dimensional overview, (b) two-dimensional cross-section and (c) Interface charges/defects at the CIGSe/PaL

For simulating point contacts at the CIGSe/buffer interface, a three-dimensional cylindrical symmetry with the rotation axis fixed at the centre of the contact junction is designed using WIAS-TESCA. This is illustrated in Figure 4.1. The contact radius, defined as α, is varied throughout the simulation, while the cell radius $\beta = 500$ nm is kept constant. When $\alpha = 0$, a complete coverage of the PaL is achieved, while no PaL is on the top of the CIGSe when $\alpha = 500$ nm. The typical thickness of 2 μm (average thickness of standard absorbers made at the PVcomB) is adopted for the CIGSe absorber with a band gap energy of 1.15 eV. The thickness of the PaL was chosen to be 15 nm, after noticing that it is not influencing the solar cell performance: a probable reason is the negligence of series resistance in the simulation. The CdS/Zn(O,S) buffer layer is fixed at 50 nm at the contact junction, whereas only a thickness of 40 nm is applied on regions with PaL. Table 4.1 gives a detailed information about the most significant parameters used in the simulation.

Now, focusing the attention to the interfaces, to have an equivalent recombination model with a certain density of surface defects N_s, very thin surface layers, 2 nm each (for CIGSe and PaL surface), are modelled with a high density of volumetric defects, N_d, because of the software limitation to include any surface charges. Using this arrangement, surface densities can be achieved using the equation: N_s [cm^{-2}] = $2 \times 10^{-7} \times N_d$ [cm^3]. The introduction of these layers, on the bottom of the PaL and top of the CIGSe, creates three interfaces:

- CdS/PaL interface — assumed to be free of defects.
- junction interface (CIGSe/CdS) including CIGSe surface layer
- passivated interface (CIGS/PaL) including CIGSe surface layer and passivation layer surface layer.

While discussing surface or interface recombination, it is noteworthy to consider the schemes of passivation: chemical and field-effect passivation. The former works under the principle of reduction of interface or surface defects [91], while the latter works on the reduction of either electrons or holes at the interface [92, 93]. The reduction of defects is directly related to the surface recombination velocity, S_{rec}; for modelling the same, a high density of neutral defects N_s^N is placed at the mid-band gap of the CIGSe, inducing S_{rec} from 10^4 to 10^7 cm/s.

Table 4.1: Simulation input parameters. d : thickness, $N_{D/A}$: donor/acceptor doping, E_g : band gap, χ : electron affinity, N_c/N_v : density of states, μ : mobility, τ : bulk lifetime, N_s^N / E_d^N : Neutral defects' density and energetic level below CIGSe conduction band, N_s^D / E_d^D / N_s^A / E_d^A : same for donor and acceptor traps. (a) CBO variation, (b) S variation, (c) defects' energetic position and (d) defects' density variation

Layer properties		CIGSe	buffer (CdS or Zn(O,S))	i-ZnO	n-ZnO
d	μm	2	0.05	0.05	0.2
$N_{D/A}$	cm^{-3}	$N_A : 10^{16}$	$N_D : 4 \times 10^{15}$	$N_D : 10^{18}$	$N_D : 1.01 \times 10^{18}$
ϵ/ϵ_0	13.6	13.6	13.6	9	9
E_g	eV	1.15	2.4	3.3	3.4
χ	eV	4.5	4.4/4.6 (a)	4.4	4.4
N_c	cm^{-3}	7×10^{17}	4×10^{18}	4×10^{18}	4×10^{18}
N_v	cm^{-3}	1.5×10^{19}	9×10^{18}	9×10^{18}	9×10^{18}
μ_n	$cm^2V^{-1}s^{-1}$	100	100	100	100
μ_p	$cm^2V^{-1}s^{-1}$	25	25	25	25
τ_n	ns	50	33	10	10
τ_p	ns	50	0.033	0.01	0.01
v_{th}	$cm.s^{-1}$	10^7	10^7	10^7	10^7
Interface properties		CIGSe/buffer	CIGSe/PaL Donor		CIGSE/PaL Donor/Acceptor
N_s^N	cm^{-2}	$5 \times 10^{12}/2 \times 10^{13}$ (b)	$5 \times 10^{12}/2 \times 10^{13}$ (b)		$5 \times 10^{12}/2 \times 10^{13}$ (b)
E_d^N	eV	0.55	0.55		0.55
N_s^D	cm^{-2}	0	$2 \times 10^{10}/2 \times 10^{12}/2 \times 10^{14}$ (d)		2×10^{13}
E_d^D	eV	0	0.08		$0.13/0.33$ (c)
N_s^A	cm^{-2}	0	0		2×10^{13}
E_d^A	eV	0	0		$0.08/0.28$ (c)

.

We structured the scheme of the simulation in a way to decouple the effects of chemical passivation and band bending assisted field-effect passivation. At the start, an ideal CIGSe/CdS solar cell with $\alpha = 500$ nm, i.e., without the PaL is designed; no defects are introduced at the interface. And then, to change the quality of the interface, the lifetime of the charge carriers and CIGSe/CdS band offsets (cliff or a spike) is altered. Following this, a porous PaL is applied in between the absorber and the buffer, and its effect on device performance is investigated. In addition to the electronic properties of the PaL, its geometry is also a parameter considered in this model. The contact area radius, α, is varied from 2 nm to 400 nm, while the distance between them is fixed constant, which is valued to be $2\beta = 1$ µm. Thus the percentage of covered area by PaL is given by : $\Pi = 1 - \alpha^2/\beta^2$.

To create surface charges at the passivated interface, we used either donor/acceptor pairs or donor defects and their densities, and energetic positions are also varied in a precise pattern. The neutral defects can't be ionised and are independent of the trap energy level if they are situated close to the mid-band gap. In short, our simulation model includes shallow and deep defect charges, surface recombination inducing neutral defects over the whole area consisting of the PaL and the contact interfaces.

4.3 Impact of passivation schemes on device performance

In the beginning, a non-passivated ($\alpha = 500$ nm) standard cell with an ideal CIGSe/CdS interface is simulated and set as the baseline. The baseline solar cell had a low density of neutral defects over the CIGSe surface layer and an efficiency of 22.45%, which is close to the record CIGSe solar cell [1]. Following, a surface limited solar cell is designed out from the baseline. This is done by increasing the neutral defects over the CIGSe surface and placing donor defects energetically close to the CIGSe mid-band gap, along with two conduction band offsets (CBO), a cliff or spike ($\Delta E_C \pm 0.1$), at the CIGSe/CdS interface; the donor trap models are equivalent to $(In,Ga)_{Cu}$ defects near the CIGSe surface [94]. By their combined effect, the efficiency drops to 14.52% for a cliff based device due to a reduction in V_{oc} (188 mV) and FF (10%).

Now, to answer the question whether a perforated PaL can recover the losses encountered, we introduced it between the CIGSe/CdS interface, enabling the contact junction formation through the openings. Initially, the nano-contact opening, α is selected to be 50 nm — close to the radius of nano-openings through Al_2O_3 described in Figure 3.4 — leading to a PaL coverage area of 96% on the CIGSe surface; this structure is set to address two types of passivation schemes: chemical passivation and surface charge induced band bending.

4.3.1 Chemical passivation of the blocking layer

In chemical passivation, the density of active defects, impurities or dangling bonds on a surface get reduced by the application of a PaL [91]; one can argue about an identical case in CIGSe with alkali fluoride post-deposition treatment [1, 2]. A pragmatic treatment of this type of passivation scheme is tackled in the simulation by reducing the defects at

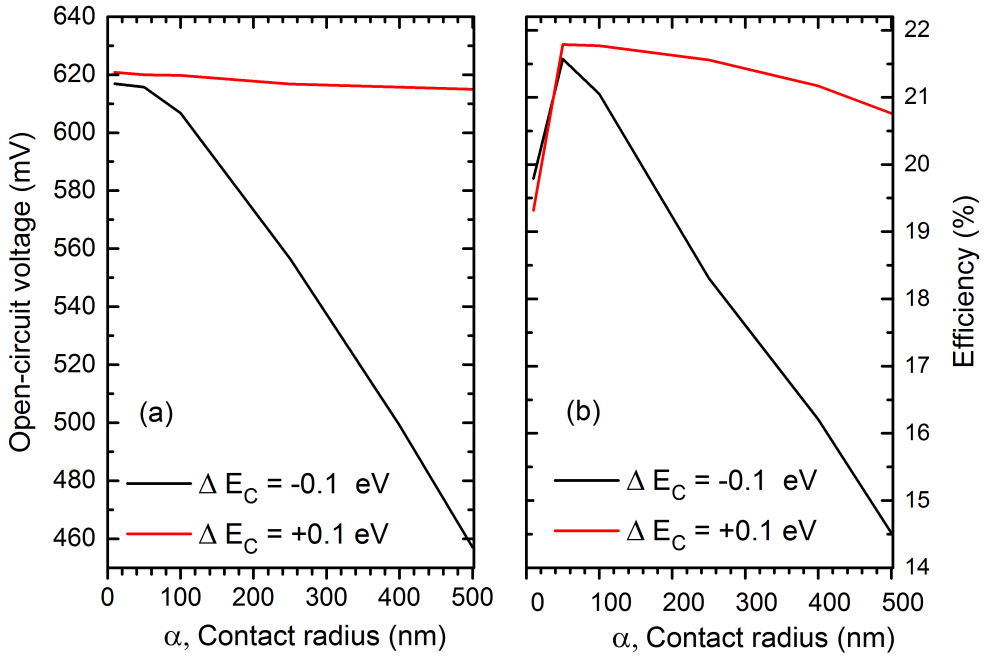

Figure 4.2: (a) Simulated open-circuit voltages and (b) corresponding efficiencies for point contact solar cell under chemical passivation scheme at the CIGSe/PaL interface. $\alpha \in [10, 400]$.

the CIGSe/PaL interface and unchanging its concentration at the point contact junction, i.e. at the CIGSe/CdS interface. To encompass different interface properties, two conduction band-offsets at the CIGSe/CdS interface are chosen: a spike and a cliff ($\Delta E_C \pm 0.1$). A realistic value of S_{rec} — 5×10^4 cm/s — is set at the CIGSe/PaL interface, reckoning that the PaL can't reduce the defect density at the CIGSe/PaL interface to zero. The thickness of the PaL is chosen from the experimental values of the ALD-deposited Al_2O_3; hence γ is set to be 5 nm, 10 nm, 15 nm and 20 nm. However, we didn't observe a dependence of solar cell performance on γ — possibly due to the drawback of WIAS-TESCA to include series resistances of the layers. Similarly, the experimental values of the contact radii of point contact junctions, α, — 45 nm and 60 nm — are also considered, but the simulation is not limited to these values, instead, α is varied from a low value of 10 nm to 500 nm, where 500 nm corresponds to an un-passivated solar cell.

The simulation mainly focuses on the interface between CIGSe/CdS and CIGSe/PaL, and therefore, V_{oc} and η will be the solar cell parameters of concern; while the former is directly related to the interface quality. Figure 4.2 illustrates the simulated V_{oc} and η of a cliff and spike based CIGSe/buffer system with point contacts through a PaL. The performance of

both interface limited solar cells (S_{rec} = 2 $\times$ 10^5 cm/s) starts to improve as the passivated area grows. Also, it can be noted that the rates of increase of both parameters for the two CBO are entirely different. For $\Delta E_C =$ + 0.1eV, the growth rate is slower and reaches a maximum η of 21.8% and a V_{oc} of 620 mV. Note that for the baseline solar cell, for a spike, η and V_{oc} are 22.45% and 645 meV respectively; whereas for a cliff, V_{oc} and η accounted to be 502 meV and 16.17%. It is obvious that the PaL tends to improve solar cell parameters, but for $\Delta E_C =$ + 0.1 eV, the CIGSe layer was not able to achieve the baseline device performance, whereas $\Delta E_C =$ - 0.1 eV surpass its corresponding baseline cell and V_{oc} and η climbed to 616.85 meV and 21.57% respectively.

The surge in the performance for the interface limited $\Delta E_C =$ - 0.1 eV can be ascribed to the impact of PaL, which raises the effective interface band gap and reduces band to band gap and cross recombination channels. But for $\Delta E_C =$ +0.1 eV, these loss channels are already impeded, and the impact of PaL is ineffective compared to the cliff condition, $\Delta E_C =$ - 0.1 eV. For both CBOs an ideal value of α is reached for 50 nm and the V_{oc} remained constant thereafter, while the efficiency began to drop. This can be attributed to the jamming of electrons as the only current path in the absorber is limited through the contact opening, leading to an increased series resistance at these points. At the other extreme, when $\alpha \rightarrow \beta$, the device approached the surface limited case. When figuring out the best configuration, it should be a balance between Π and α. An efficient point contact structure should be of very low radius — in our case this lies between the openings $50 - 100$ nm corresponding to a passivated area of 98 – 94%, and 2β should be less than the diffusion length of CIGSe.

4.3.2 Field-effect passivation of the blocking layer

Another way to achieve low S_{rec} or higher $\tau_{p/n}$ is to reduce one type of charge carriers close to the interface via an electric field induced by a PaL at the interface. In case of a p-type absorber like CIGSe, since minority carriers are moving towards the front contact, a high density of positive charge at the interface is required to generate an inversion at the CIGSe surface. We tested some possible PaL candidates (Al_2O_3, ZnS, SiO_2) which can generate positive charges and Al_2O_3 is kept as the PaL for the rest of the studies as we saw a strong increase in the photo-luminescence from these layers on top of CIGSe (refer

to appendix Figure 8.5). Other possible candidates that could provide positive charges found in the literature are HfO_2 layers or stacks of $SiO_2/HfO_2/Al_2O_3$ [95]. In the simulation, we replicated this scenario by placing a high density of donor charges close to the CIGSe conduction band, equivalent to positive charges in a PaL. They will not ionize and contribute to parasitic recombination.

The simulation is started with an $\alpha = 100$ nm, corresponding to a $\Pi = 96\%$ and N_s^D in the range $10^{10} - 10^{14}$ cm^2. For N_s^D >10^{12}, we observed a surge in the efficiency, surpassing even the baseline solar cell; the efficiency climbed up to 23.2% along with an upgrade in V_{oc} to 665 mV.

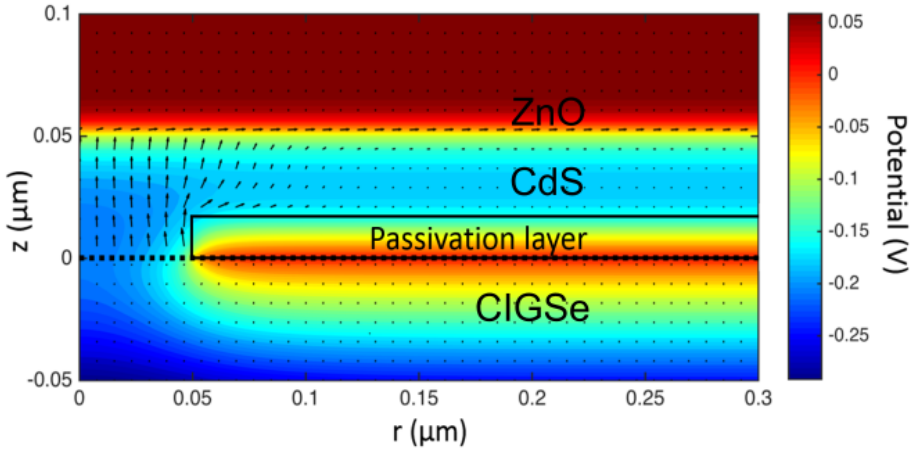

Figure 4.3: Simulated potential (color scale) and electron current (arrows) for contact junction radius, $\alpha = 50$ nm. $z = 0\mu$m corresponds to the CIGSe front interface.

The strong rise in the η prompted us to zoom near interfaces — CIGSe/CdS and CIGSe/PaL — of the simulated solar cell under illumination. The zoomed-in version of the potential diagram is displayed in Figure 4.3. The potential diagram exhibits a gradient in the electric field close to the interfaces. Compared to the CIGSe/CdS interface, the rate of change in potential was higher at the CIGSe/PaL interface, depicted by the colour change from blue to red. This is expected, but what was more interesting is the extension of the field gradient into the CIGSe/CdS interface. It is guaranteed that the change in potential in these regions will bring a change in CBO and VBO. A crude estimation of these offsets can be calculated using Anderson's rule [96], even though this model does not account for interface charges.

$$CBO = \chi_{\mathrm{CIGSe}} - \chi_{\mathrm{CdS/PaL}}$$
$$VBO = E_{g,CdS/PaL} - E_{g,CIGSe} \tag{4.1}$$

To see the modification of the electronic properties brought by the PaL, we checked the band alignment and band bending near the interface. It is experimentally evident that a spike at the CIGSe/CdS interface is favourable for CIGSe based solar cells [97, 98]. The band diagram close to the interface at z=0 as a function of the perpendicular distance to the interface is shown in the Figure 4.4. The bands were plotted by taking two vertical cross sections bisecting the CIGSe/CdS interface and CIGSe/PaL interface on the potential diagram.

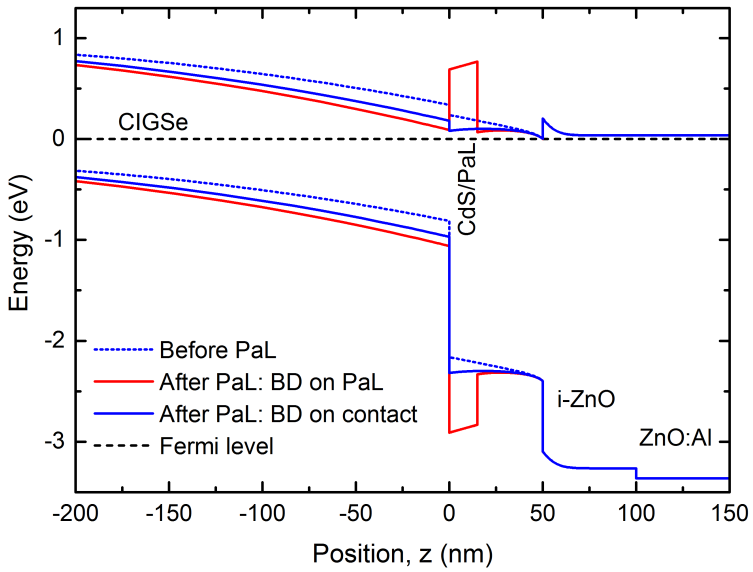

Figure 4.4: Simulated band diagram for a point-contacted solar cell (ΔE_C = -0.1 eV). Cross-section along the z-axis close to the interface before the application of point contacts (blue dashed lines), after the introduction of point contact: at the contact (blue curve) and on the passivation layer (red curve). $\alpha = 50$ nm and $S = S_{max} = 2\times10^5$ cm/s.

As anticipated, a big spike is visible at the interface on the conduction band showing the current blocking behaviour of the PaL. Moreover, a strong inversion is generated at the CIGSe/PaL interface. Comparing the band bending at both junctions, the inversion at the PaL interface accounted to be 0.2 eV more than at the contact junction, drawing the conduction band closer to the Fermi level near the CIGSe/PaL interface, altering the charge carrier transport and their environment.

In this context, quantifying the position of the Fermi-level at the interface can give a better understanding of the band bending at the interface. As discussed in the last paragraph, the band bending at the interface and the point contact junction can be calculated by taking a horizontal cross-section of the valence band across them, followed by taking the difference between the valence band energetic level in the bulk ($E_{v,bulk} = -0.19eV$) and at the first discontinuity at the CIGSe/PaL interface.

$$\begin{aligned} \phi_{PaL} &= Ev_{bulk} - Ev_{PaL} \\ \phi_{C} &= Ev_{bulk} - Ev_{C} \end{aligned} \tag{4.2}$$

Note that the simulated CIGSe solar cell under discussion has a cliff type band alignment at the CIGSe/CdS interface with $\alpha = 100$ nm and $\Pi > 96\%$, and an inversion is witnessed at the contact junction influenced by the PaL. This motivated us to look further into the effect of the band bending at the contact junction if $\alpha < 100$ nm or $\Pi > 96\%$.

Figure 4.5 shows the effect of the passivated area or the contact radius on the band bending at the contact junction, along with potential diagrams for α = 10 nm, 50 nm and 100 nm. As Π began to grow (α shrinking), the transition of the band bending at the contact junction, ϕ_c, began to rise and a maximum impact is reached when $\lim_{\alpha \to 0} \phi_c = \phi_{PaL}$, $\alpha = 10$ nm. Between the two extremes of α, the value of 200 meV in band bending is calculated from the Figure 4.5. Even if the passivated area is smaller, 250 nm $< \alpha <$ 400 nm, a beneficial effect is always visible. However, a significant influence ensued when it crosses the threshold value, α =100 nm with Π= 96%. Here, Π is greater than the experimental Π calculated using XPS measurements in Table 3.2 (despite considering errors from the quantitative analysis), where the openings are achieved by random arrangement of CdS NP's. A possible way to simulate the real case scenario is to generate random openings using a random distribution.

As shown in Table 4.2 (the band bending values at the point junction are calculated from Figure 4.5), an optimal configuration for a band bending assisted passivation is reached for a cell with α = 10 nm and $\Pi > 96\%$. The efficiency is increased by almost 1.69% from the baseline cell and V_{oc} climbs up to 677 mV. Also, a relaxation in α is observed (modest changes in cell performance when $\alpha <$ 100 nm) compared to the chemical passivation.

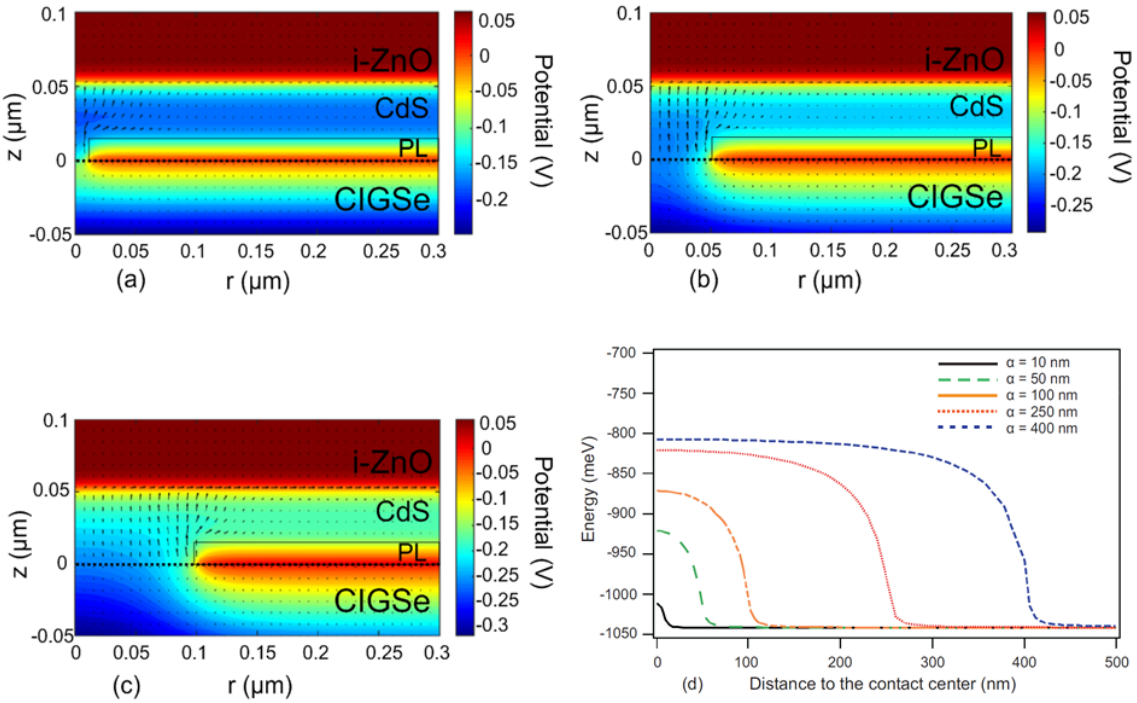

Figure 4.5: Simulated potential (color scale) and electron current (arrows) for contact junction radius, α:(a) – (c) = 10, 50, 100 nm respectively. $z = 0$ μm corresponds to the CIGSe front interface. (d) Distance from the valence band to the Fermi-level 2 nm below the CIGS front interface. $\alpha \in [10, 400]$. PaL defect structure, interface recombination velocity and CBO at CIGSe/CdS interface and CIGSe/PaL interface is same as in Figure 4.4; the semiconductor parameters are listed in the default Table 4.1.

Yet, losses appear when Π reaches 99%. A possible explanation is the gradual increase in series resistance seen by the charge carriers. However, the mechanism of the transport of the carriers is entirely different from the chemical passivation. Here, the electrons are driven to the passivated surface and the holes are repelled from the interface by the electric field generated from interface charges. Thus, the lifetime of the charge carriers at the interface and at the junction is enhanced, and the jamming of charge carriers in comparison to the chemical passivation is considerably diminished. And on reaching a new equilibrium, the diffusion assisted transport mechanism comes into act and the electrons are directed to the nano-contacts.

In the previous analysis, we used a CIGSe/CdS standard solar cell with donor defects lying close to the mid-band-gap and witnessed a recovery in η and V_{oc}. This motivated us to extend this approach further to CIGSe cells with different interface qualities. We handled

Table 4.2: Band bendings calculated for the simulated cell in Figure 4.5. Π is the percentage of passivated area, ϕ_C is the band bending at the contact center, ϕ_{PaL} at the passivation layer

α (nm)	Π (%)	ϕ_C (eV)	ϕ_{PaL} (eV)
10	> 99	0.82	0.85
50	99	0.81	0.85
100	96	0.68	0.85
250	75	0.61	0.85
400	36	0.60	0.85

four types of solar cells for this purpose, with different conduction band offset (± 1) and S_{rec}. Introducing a cliff at the CIGSe/CdS interface minimises the effective band gap seen by the numerous interface recombination sites [37]. And if a passivation layer can annihilate these defects, this would give more options for the selection of buffer layers.

Table 4.3: Matrix showing the four types of investigated solar cells. *CBO* refers to conduction band offset at CIGS/CdS. S_{rec} refers to interface recombination velocity. S_1 and S_2 denotes high and low recombination velocity, and C_1 and C_2 represents spike and cliff respectively.

CBO and S_{rec}	$S_1(5 \times 10^4 cm.s^{-1})$	$S_2(2 \times 10^5 cm.s^{-1})$
$C_1(0.1$ eV (spike)) [97–99]	1	0
$C_2(-0.1$ eV (cliff)) [100, 101]	0	1

Taking this into account, we designed four baseline standard cells for the four cases as described in Table 4.3 (1) $S_1 \cdot C_1$ (2) $S_2 \cdot C_1$ (3) $S_1 \cdot C_2$ (4) $S_2 \cdot C_2$ and followed the same route as in the previous analysis.

Figures 4.6 (a) and (b) show the simulated V_{oc} and corresponding η for values of α from 10 nm to 500 nm, and Figure 4.8 shows the simulated $J-V$ curves for α = 50 nm including all types of devices considered. We chose V_{oc} as the parameter to be investigated because it gives the direct information about recombination. The findings were similar to the previous case, but we noticed a rapid recovery in the case of a cliff, $S_2 \cdot C_2$, in comparison with high quality surface cell, $S_1 \cdot C_1$. In both cases the passivation had positive effects on the solar cell. As α started to get smaller, V_{oc} rose independently of the quality of interfaces considered at the beginning and converged to the same limit for all the solar cells. The same trend was followed by the efficiency. The effect of an increase in series resistance

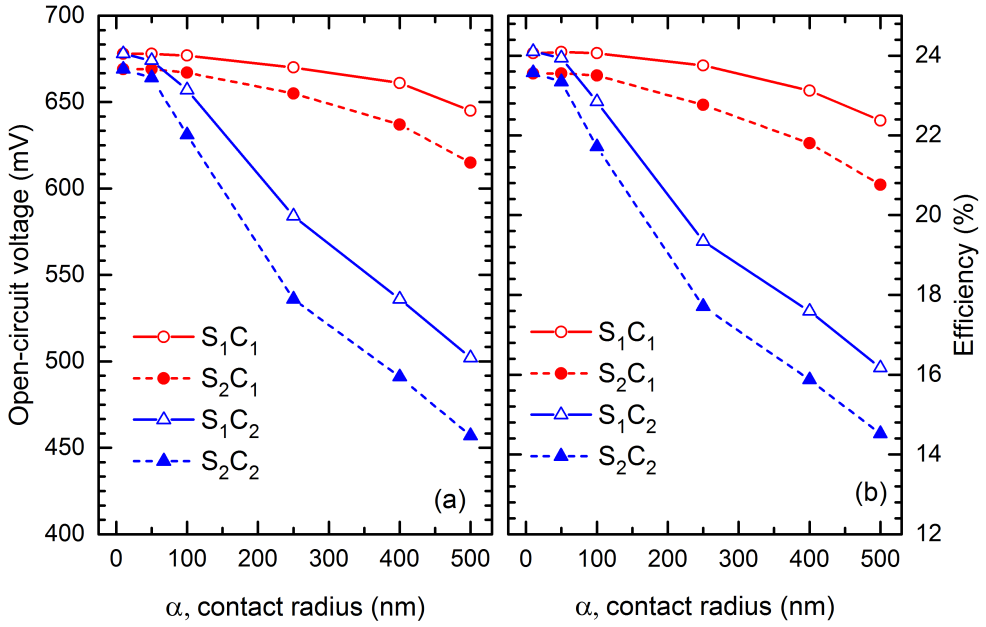

Figure 4.6: (a) Simulated open-circuit voltages, and (b) corresponding efficiencies for different values of α under field effect passivation scheme: $\alpha \in [10, 500]$, $S_1 \cdot C_1$, $S_2 \cdot C_1$, $S_1 \cdot C_2$ and $S_2 \cdot C_2$ take the values as described in Table 4.3.

and FF losses was noticed below α = 10 nm. These results indicate which kind of CIGSe interfaces will get a beneficiary effect from a point contact structure; a high defective surface would be able to exploit the point contact structure, while it brings gentle effects on high quality surfaces. Adding to this, a complete elimination of the negative influence of the cliff at the CIGSe/CdS can challenge the role of a buffer layer; the main feature of which is to align the band between the absorber and the window layer. However, the modelling of S_{rec} through a thin layer with high N_d could be the reason for these results, which doesn't reckon the tunnelling recombination between charge carriers coming from different layers.

Unlike in the case of the cliff and spike, when S_{rec} is taken into consideration, the results didn't have substantial changes; even with an ideal PaL, V_{oc} and η didn't climb up to the same level. An explanation for this behaviour can be given by the partial passivation of defects as assumed in the model. And concerning the retrieval of the performance, a better performance was shown with devices having low S_{rec}, showing what kind of devices would get benefited from point contacts configuration. Still, a slight improvement was observed for all devices with high S_{rec} when $\alpha > 250$ nm — in these devices the efficiency is limited by the recombination in the quasi-neutral region. Figure 4.7 (a) shows the impact of charge density on the V_{oc} of the four devices considered. It can be observed that all devices V_{oc}

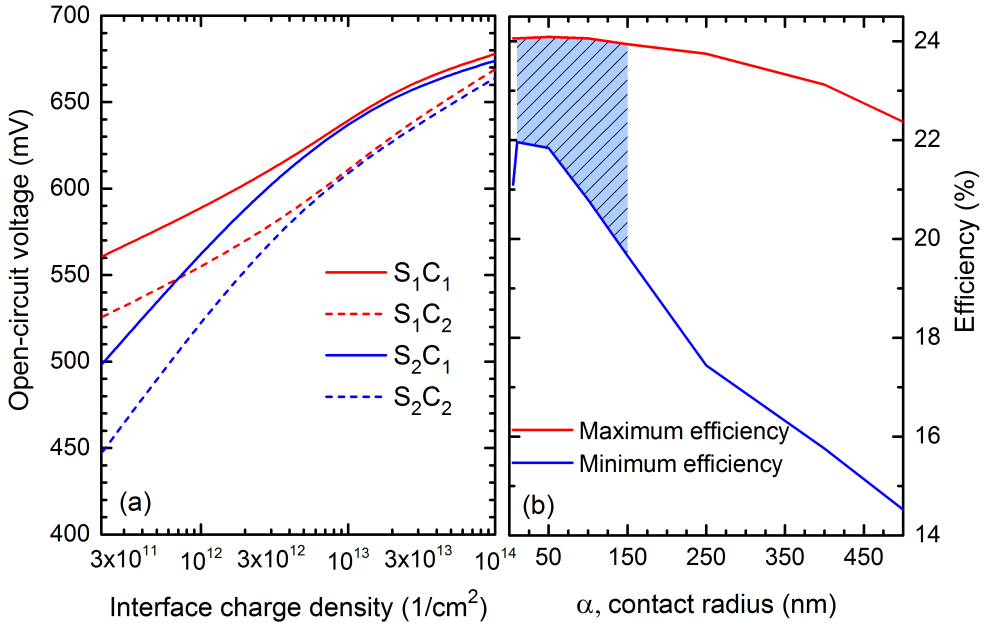

Figure 4.7: (a) Simulated open-circuit voltage as a function of charge density in the passivation layer for four types of solar cells considered in Table 4.3. (b) Minimum and maximum efficiency for different values of α and defect structures studied as described in Table 4.1; the simulated data follows the same set of parameters used in Figure 4.6

converged to the same point when interface charge density is close to 10^{14} cm^{-2}. And the effect of band-offsets became insignificant when it crossed 3×10^{12} cm^{-2}. The boundaries of efficiencies of four solar cells is illustrated in Figure 4.7 (b). The shaded part shows the range of α that can be beneficial for a point contact structure. Combining Figures 4.6, 4.7 and 4.8, we summarised the limits of efficiency that can be achieved by CIGSe devices with a point contact structure, and this could be used as a framework for future experiments.

Until now, for all the cases considered , a strong n-type inversion at the CIGSe/PaL interface is the deciding parameter attenuating the influence of interface recombination. Experimentally, it can be activated by the diffusion of atomic elements into the Cu vacancies in a Cu-poor CIGSe absorber, similar to Zn diffusion from a ZnS passivation layer [102] or the removal of Cu from the interface and occupation of potassium with the KF treatment [47]. Since these are found to be advantageous for CIGSe absorbers, their energetic level should lie closer to the CIGSe conduction band. Furthermore, we examined what happens if they turn into deep defects and modelled it by changing the defect energy level closer to the mid band gap and plotted as a function of band bending they induced. These results are displayed in Figures 4.9 (a) and (b).

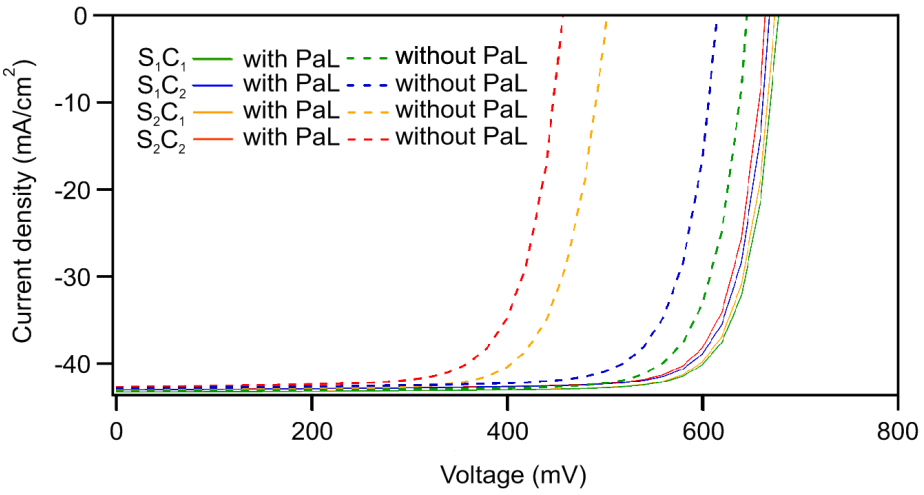

Figure 4.8: Simulated current-voltage curves for unpassivated (dotted lines) and passivated solar cells (solid lines) for $\alpha = 50$ nm for different type of solar cells considered in the table 4.3. The PaL has a charge density $N_s^D = 2 \times 10^{14}/\text{cm}^2$ and rest of the semiconductor parameters follows table 4.1.

Figures 4.9 (a) and (b) show that the band bending at the passivation layer, ϕ_{PaL} is not controlled by S_{rec} and CBO, and from the Table 4.2, it can be concluded that ϕ_{PaL} is independent of α. Summing up the three,

$$\frac{\partial \phi_{PaL}}{\partial \alpha} = \frac{\partial \phi_{PaL}}{\partial CBO} = \frac{\partial \phi_{PaL}}{\partial S_{rec}} = 0 \tag{4.3}$$

Hence, ϕ_{PaL} is considered as the deciding parameter. It has significant influence on V_{oc} and η, and independent of S_{rec} and CBO values at CIGSe/CdS, $V_{oc}(\phi_{PaL})$ and $\eta(\phi_{PaL})$ are monotonically increasing functions. But, a closer look will decipher the parasitic behaviour of the defects depending upon their positions in the band gap. In these cases, they play a double agent role: influencing band bending and enhancing recombination. Therefore, the position of these defects and their density should be the factors to be reckoned, while considering a point contact structure. Leaving aside these negatives, when $\alpha = 100$ nm, $\phi_{PaL} > 0.85$ eV and for each value of S_{rec} and CBO, a PaL significantly enhances the device performance by at least 10%.

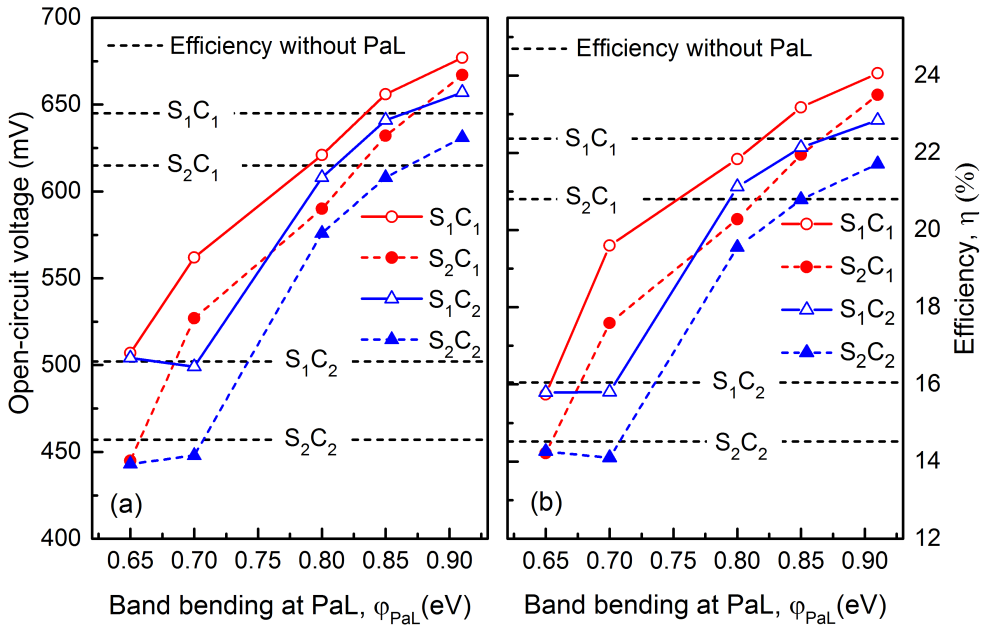

Figure 4.9: Impact of band bending at the passivation layer, ϕ_{PaL} on the V_{oc} and efficiency of solar cells studied (the values of S_1, S_2, C_1, and C_2 are tabulated in Table 4.3) for α =50 nm. Semiconductor parameters follows the default values in Table 4.1. Horizontal dotted lines represent the unpassivated device performance in each category mentioned in Table 4.3.

Summarising the results from the simulation, a point contact structure through a pasivation layer is beneficial when it meets the following conditions:

- $\Phi_{PaL} > 0.85eV$, i.e. sufficient band bending is generated by the PaL
- $99\% > \Pi > 95\%$, i.e. more than 95% of the interface is passivated. In our case, this corresponds to $\alpha \leq 50nm$

The first factor depends on the defect structure at the interface or in other words the interface charges. The density of these interface charges should be sufficient to induce a favorable band bending. This also includes donor defects introduced to the absorber through diffusion; however, a distinction between the two is not executed in the simulations. In the field-effect passivation, the main parameter that describes the influence of the PaL is the band bending it induces at both interfaces. For a good inversion at the CIGSe/CdS interface, in addition to the interface charges, the passivation area should lie between 95 – 99%. Also, another important thing we noticed is that the relaxation of requirements in case of the field-effect passivation as compared to the chemical passivation. In the lower

regime of the contact junction openings, the efficiency almost stayed constant. Field-effect passivation could also relax the diffusion length parameter. A perfect example for this is the passivated emitted rear CIGSe ultra-thin solar cells, where even with the pitch width of 2 μm [103] and 10 μm [54], an improvement is reported; the same can be applied to the front-end passivation, thus challenging the diffusion length requirement.

The PaL is more beneficial to a poor interface quality absorber (a cliff at CIGS/CdS and a high S_{rec}). An optimum buffer layer, in addition to an appropriate band line-up, should also generate shallow defects at the interface carrying the required positive charge. The standard CdS buffer layer might do so via ionised Cd within the Cu-free surface reconstruction of CIGSe [104]. As our model includes charged defects only at the PaL but not at the contact interface, it may be argued that the benefit of the PaL layer is exaggerated. However, additional calculations (not shown here) suggest that a cell with full area contact even with charged defects will still be worse than the point contact cell, in particular with the cliff-type band alignment. If nothing else, using two different materials (contact, PaL) to fulfil one requirement (band line-up, positive charge) each should provide more flexibility in designing the best possible interface.

The results highlight the fact that the most efficient passivation layer works through the field-induced passivation. Instead of looking at the defect density or the defect energetic level, the surface charge density at CIGS/PaL should be investigated for improving efficiency. Correlating experimental results from chapter 3 — refer to Figures 3.4, 3.12 and Table 3.2) — and simulation results, it can be seen that the contact radius condition is satisfied, while the coverage area is marginally less; yet, PaL and point contact is a promising aspect to implement in tangible CIGSe devices. The results also give insights on the factors that should be addressed while creating an innovative point contact technology on the CIGSe surface.

4.4 Point contacts at the Mo/CIGSe interface

An incomplete absorption and back contact recombination are the main limiting factors in achieving high efficiency ultra-thin CIGSe solar cells. With the aid of 2D simulations Nerat [105] showed that localized point contacts at the back interface have the potential to boost

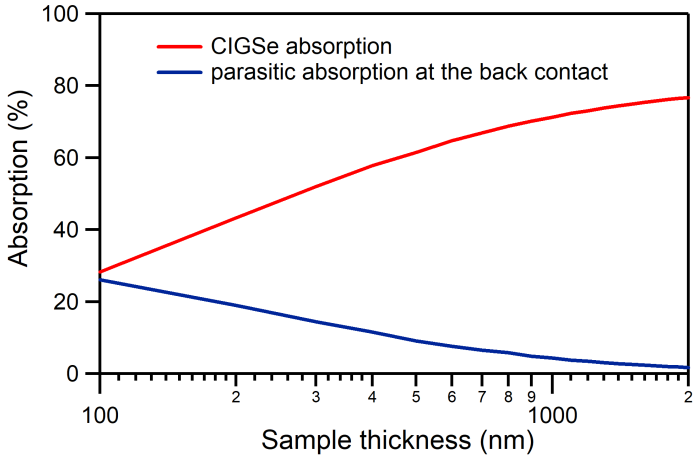

Figure 4.10: Simulated absorption plot as a function of CIGSe absorber thickness.

the performance of absorbers by 15% compared to the standard CIGSe solar cell with whole back contacts. In this simulation work, we tried to get a qualitative understanding of the optical and electrical influence of the point contacts at the back interface of thinner absorbers using SCAPS. Since the recombination velocity at the back contact influences the diode current and photo-current, we varied the back contact recombination velocity over a wide range from 10^3 cm/s to 10^7 cm/s, equalling the electron thermal velocity. Also, SCAPS gives the option to study the effect of reflection at the back interface; the lowest reflection at the Mo back contact is chosen to be 20%, as reported in the literature [106]. The semiconductor parameters used in this simulation follow the values in the Table 4.1, to which variation of absorber thickness and reflection at the back contact are to be considered.

Figure 4.10 demonstrates the influence of absorption as a function of CIGSe absorber thickness. Optical losses in thinner CIGSe occur mainly in the infra-red region and are expected due to the material reduction. The significant drop in the absorption starts at 1 μm, which is also the limiting absorber thickness. Also, it should be noted that the parasitic absorption at the back contact is increasing with decreasing absorber thickness and converges to the absorption value for a 100 nm CIGSe layer, which is evidently due to poor Mo reflectivity. Figure 4.11 covers the electrical influence for a range of interface recombination velocities and reflection at the back contact in relation to absorber thickness. The enhancement in the rear contact recombination, at the CIGSe/Mo interface, occurs when the absorber thickness is comparable to the diffusion length of the carriers. It can be seen that the V_{oc} is negligibly affected by the change in reflection at the back contact, but

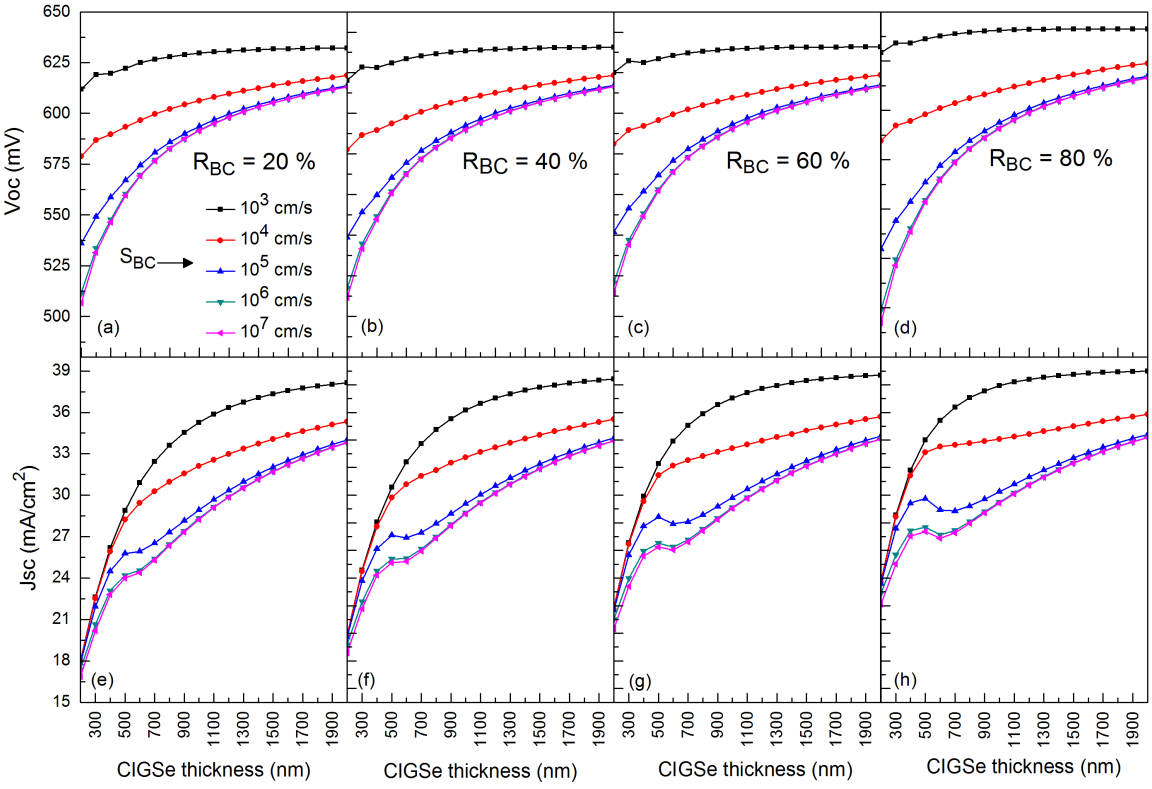

Figure 4.11: Simulated V_{oc} and J_{sc} values for CIGSe solar cells as a function of absorber thickness. The interface recombination velocity at the back contact is varied from 10^3– 10^7 cm/s and reflection from 20 – 80%.

heavily depends on the interface recombination velocity. It reduces steeply for recombination velocities greater than 10^5 cm/s. In the case of J_{sc}, reflection influences its trend over the whole range of thickness and also for all recombination velocities; it exhibits a similar behaviour and converges to a lowest value of J_{sc}. With an increase in the reflection at the back contact, these convergence points are shifted to higher J_{sc} values. In summary, the simulation shows that reducing the back interface defect concentration can lead to an increase in V_{oc}. On the contrary, an increase in J_{sc} is related with an increase in rear optical reflection.

4.5 Summary

For correlating experimental results and to find optimum cases, a three-dimensional simulation investigation was done on a wide range of solar cells with nano point contacts through a PaL at the CIGSe/buffer or Mo/CIGSe interface. A distinction between the chem-

ical and the field-effect passivation was addressed, along with different band alignments at the CIGSe/buffer interface, foreseeing the effect of other buffer layer applications.

Both the chemical and the field effect passivation showed a positive influence on CIGSe device performance. However, the latter induces band bending at the CIGSe/PaL interface and influences the band bending across the contact layer, altering its electronic properties. The maximum effect is achieved for a density of interface charges greater than 10^{12} cm^{-2} and a contact radius under 100 nm (coverage area = 95%). Passivation through band bending gives more flexibility on the contact radius and diffusion length compared to the chemical passivation and performed better than the baseline solar cells. On extending this approach to cells with favourable and unfavourable conduction band offsets (a cliff or a spike) at the CIGSe/CdS interface, a strong rise in the cell parameters is observed in case of the cliff in contrast to the spike, pointing towards which kind of cells could get more beneficial effect from defect passivation. The recovery in the cliff based interface also questions the role of buffer layers and offers more freedom in its selection. The CdS layer or other potential buffers can be constrained only to the contact openings as there is no need for CdS on top of the passivation layer. This will certainly reduce the absorption and enhances the fill factor and current density. Incorporating the point contacts at the back interface can lead to an increase in the V_{oc} if the PaL decreases the interface defect density, and even a J_{sc} enhancement is possible if PaL provides an effective reflection compared to Mo. To conclude, the simulation defines the box in which point contacts parameters should lie to have a beneficial effect on CIGSe device performance, and gives significant input for designing point contacts through an efficient passivation layer.

5

Incorporation of point contacts at the CIGSe/buffer interface

This chapter expands the work of the theoretical modelling of the point contacts at the CIGSe/buffer interface in section 4.2 by combining it with experimental investigations to compare their predicted effect on the device performance. The theoretical model predicts that the point contacts at the CIGSe/buffer interface can bring a positive influence on efficiency compared to the unpassivated reference CIGSe solar cells, provided that the interface charges are greater than 10^{12}cm^{-2}, and the contact radius should be less than 100 nm (refer to Table 4.2). The point contacts fabricated using CdS NP's, synthesised by the solution based approach, have radii of 45 nm and 60 nm (see Figure 3.4), which meets the above requirement. A successful application of the point contacts through a suitable passivation layer can passivate the defects chemically or electrically at the interface, and then, the impact will be visible in the V_{oc} of the devices according to the Eq. (2.11).

To separate the effect of passivation and point contacts on efficiency, five different configurations of CIGSe solar cells with point contacts and their corresponding reference cells were considered in this work. The photo-voltaic properties of reference cells were compared with a numerical model to explain the device performance. Then, the point contacts were applied at the CIGSe/buffer interface and conversion efficiency compared with the reference cells. Since the focus is on the effect of point contacts, no post deposition treatment using potassium fluoride was done on any samples prepared.

5.1 Modelling of CIGSe reference solar cells

In order to qualitatively understand the behaviour of the reference CIGSe solar cells without any point contacts, numerical simulations are done with SCAPS, keeping the interface as the region of focus. The recombination rate due to a defect at the interface is determined by the interface band gap and its energetic position, E_t, to the CBM and VBM. And in a hetero-interface, the interface band gap is determined by the electron affinity and the CBM and VBM of both materials. For realising an effective band gap, $E_{g,IF}$, at the CIGSe/buffer interface (refer to Figure 5.1), the buffer layer should have a higher band gap and low electron negativity compared to the CIGSe. CdS and Zn(O,S) have higher band gaps of 2.4 eV and 3.3 - 3.6 eV [107] compared to the high efficiency CIGSe device (1.15 - 1.2 eV). Experimentally, different values of conduction band offsets, ΔE_c^{IF}, at the CIGSe/buffer interface are reported with CdS [108] and Zn(O,S) [109–111], ranging from a cliff to spike. Figure 5.1 encompasses the simulated band diagrams for three cases. For a cliff case at the CIGSe/buffer interface, the inversion is reduced, the electron quasi-Fermi-level is receded from the CBM, the $E_{g,IF}$ is lowered and the band to band and the defect assisted recombination are enhanced (refer to Figure 5.1 (c)). In contrast, as shown in Figure 5.2 (a) – (d), ΔE_c^{IF} between 0.0 - 0.3 eV is advantageous for CIGSe solar cells. In this range, ΔE_c^{IF} impedes the effect of interface recombination velocity and V_{oc} starts to converge to a higher value due to the a higher concentration of electrons at the interface at all voltage biases; however, all other device parameters start to decline drastically for $\Delta E_c^{IF} > 0.3$ eV, irrespective of the recombination velocity. A further increase in the ΔE_c^{IF} will result in an electron barrier at the interface, affecting the electron extraction and injection. This condition is shown for $\Delta E_c^{IF} \geq 0.4$ eV in Figure 5.2 (e); this is similar to the case when the passivation layer completely covers the CIGSe surface.

An electron barrier can also be induced by the acceptor states at the interface, if a sufficient density of acceptor states (simulated value corresponds to $N_{A,IF} > 2 \times 10^{11}$ cm^{-2} is present as shown in Figure 5.3. The acceptor defects placed at an energetic position of 0.6 eV from the VBM reduce the inversion, the space charge area, and the potential drop in the absorber. This leads to an upward rise of the CBM, creating an electron barrier above the energetic position of the acceptor defect, increasing the distance between the electron quasi-Fermi level and the CBM. The result is reduced extraction efficiency, increased bulk and interface recombination. The same phenomenon is applicable for the acceptor states

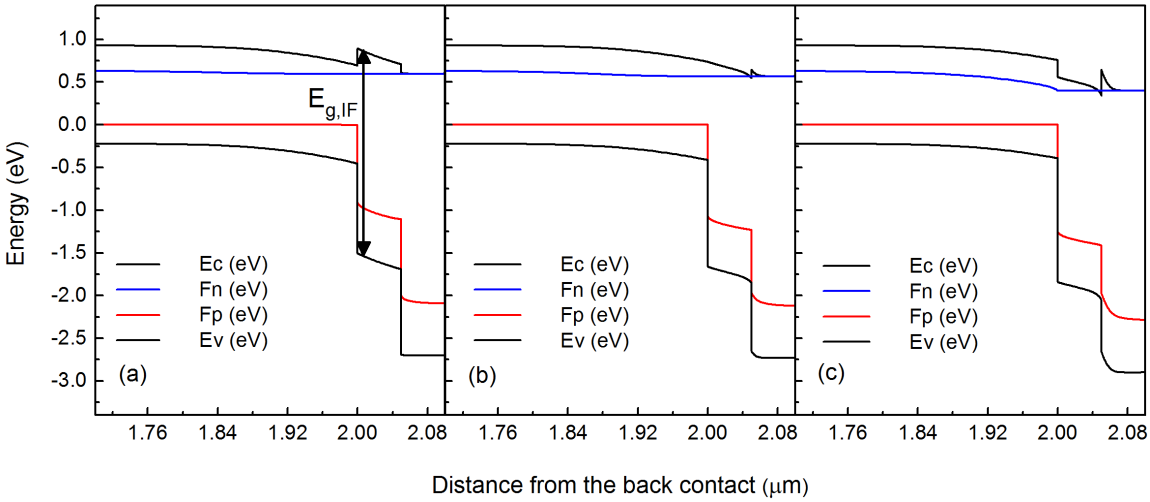

Figure 5.1: Simulated energy band diagrams for different band alignments for reference CIGSe solar cells close to the CIGSe/CdS interface: (a) spike (ΔE_c = 0.1 eV), (b) flat band (ΔE_c = 0 eV) and (c) a cliff (ΔE_c = -0.1 eV).

in the buffer layer. But compared to the N_A^{IF}, the V_{oc} starts to increase for higher acceptor defect concentrations. This is due to a relatively high hole density compared to the electron density near the interface as shown in Figure 5.3 (e), and as a consequence, V_{oc} is unaffected. Also, it is apparent from the Figure 5.3 (e) that the minimum in the V_{oc} in Figure 5.3 (c) corresponds to the stage where electron and hole densities are equal. On the other hand, donor defects close to the conduction band can reverse the accumulation to an inversion, if a sufficient amount of donor defects is present at the CIGSe/buffer interface. This is shown in Figure 5.3 (f).

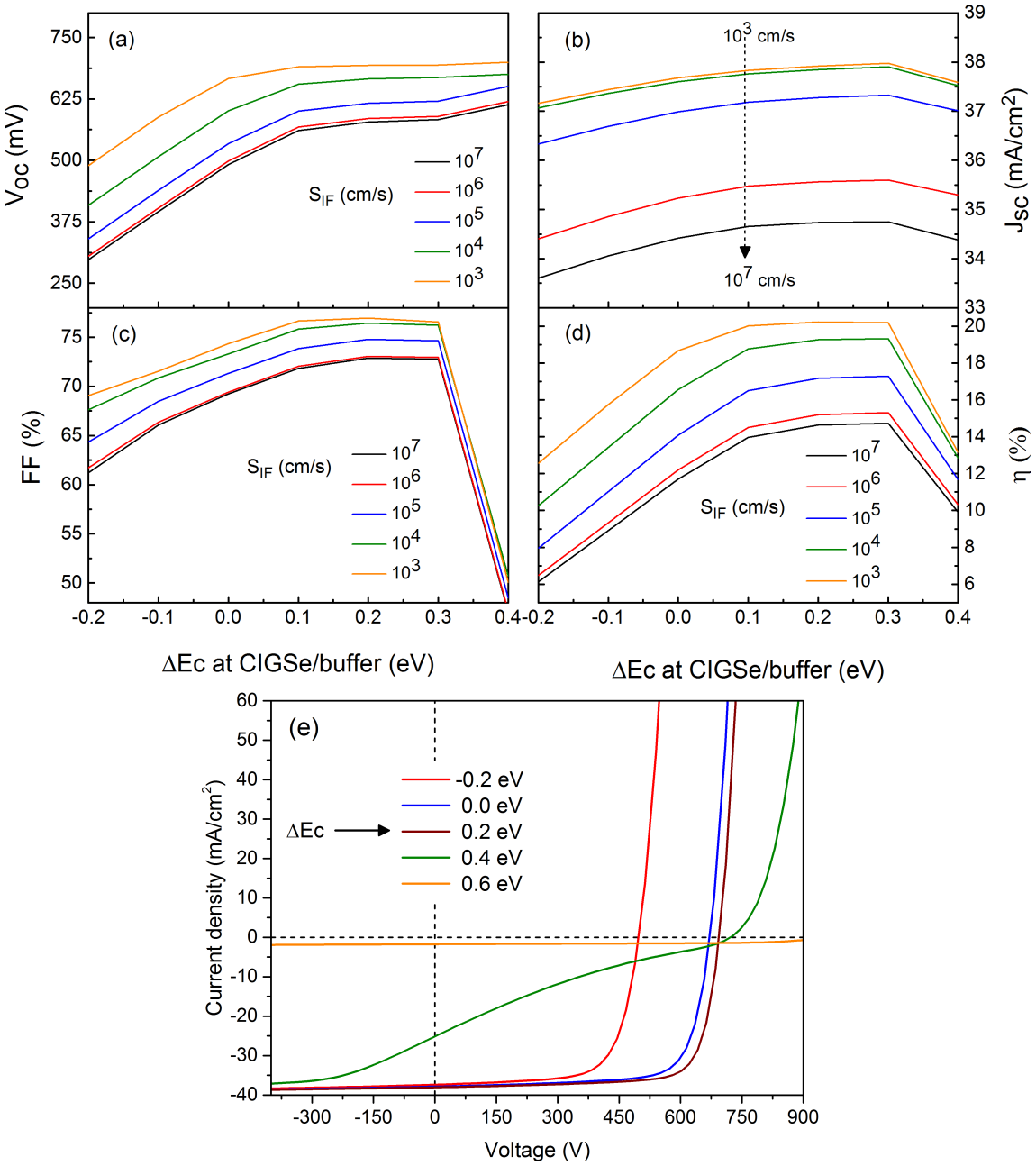

Figure 5.2: (a) – (d): simulated device parameters as a function of conduction band offsets, ΔE_c, at CIGSe/buffer interface for different interface recombination velocities and (e) their corresponding J–V curves.

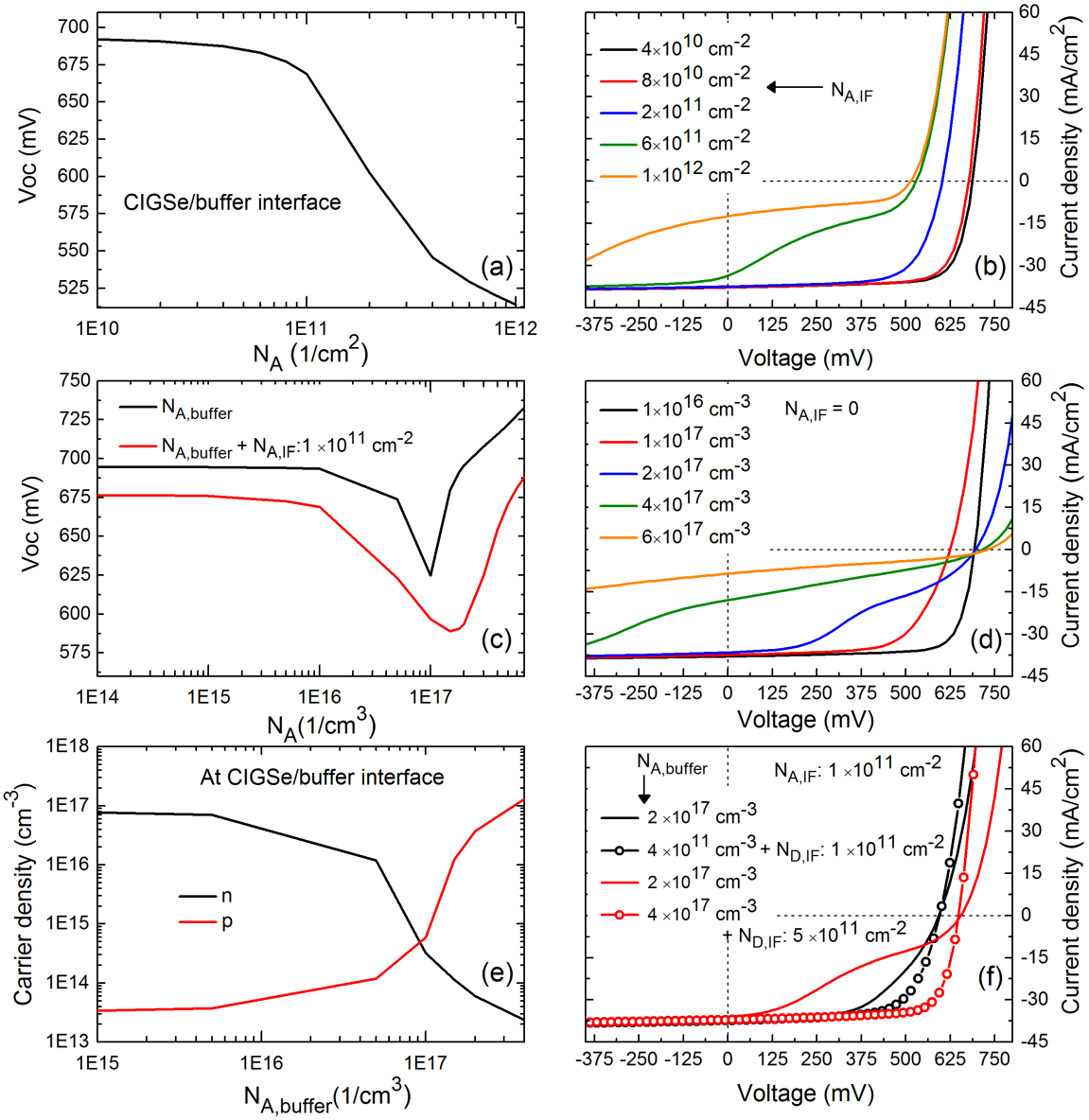

Figure 5.3: (a) and (b): simulated values of V_{oc} as a function of acceptor defect density, N_A, at the CIGSe/buffer interface and corresponding J–V curves, (c) and (d): V_{oc} as a function of N_A in the buffer and corresponding J–V curves, (e) carrier density as a function of N_A in the buffer and (f) J–V curves of CIGSe devices with N_A at the CIGSe/ buffer interface and in the buffer (solid lines), and after the introduction of donor states close to the CBM at the interface (solid lines with open circular dots).

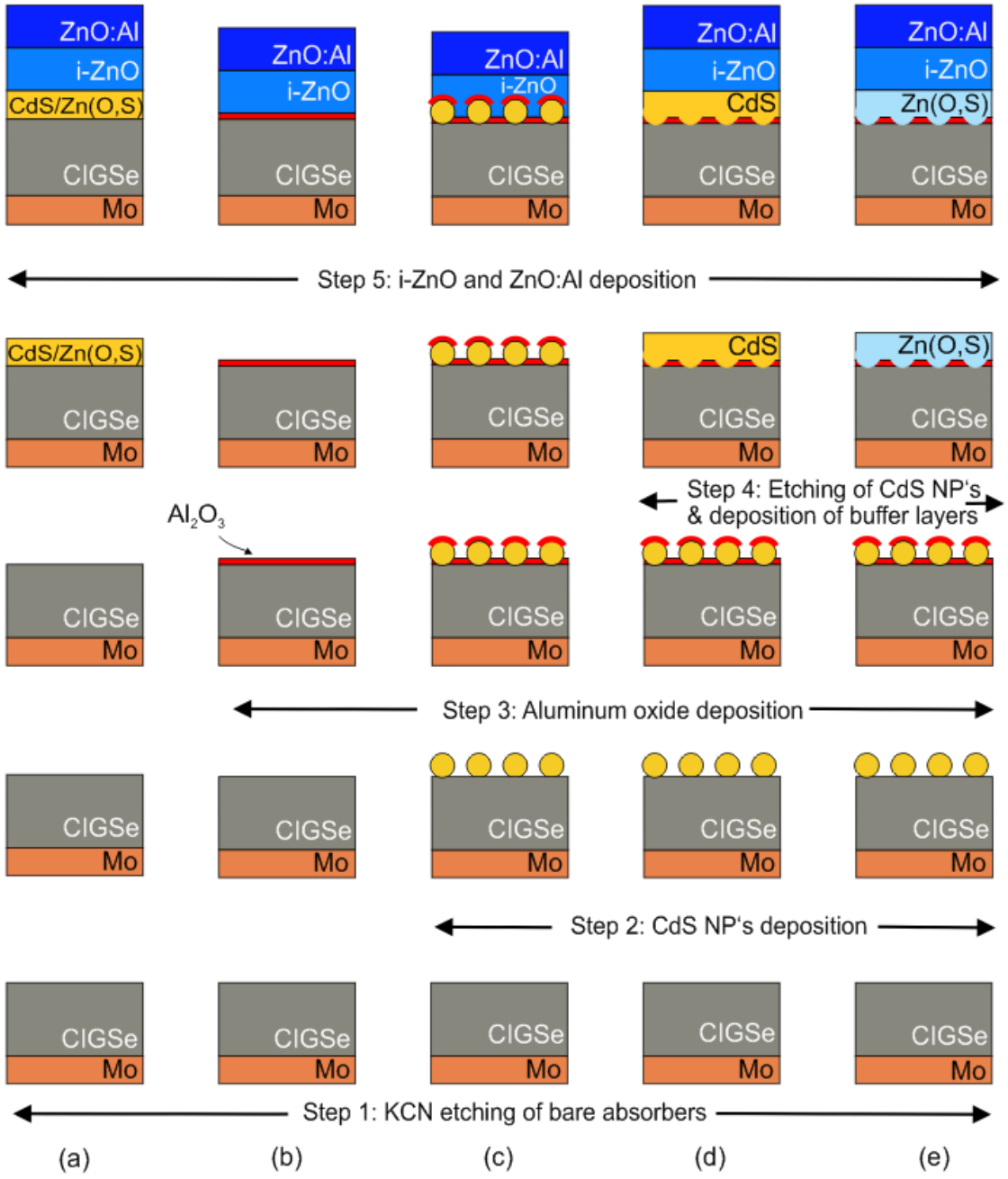

Figure 5.4: Bottom to top: schematic diagram showing the fabrication of the four different types of solar cells and reference solar cells used in this thesis: (a) Reference solar cells with standard fabrication procedure as discussed in section 2.2, (b) CIGSe solar cells with a passivation layer (Al_2O_3) and buffer layers (either CdS or Zn(O,S)) on top, (c) CIGSe solar cells with CdS nanoparticles acting as the point contacts and the buffer layer (no etching out of CdS NP's) with a layer of Al_2O_3, (d) CIGSe solar cells with point contacts and CdS as the buffer layer and (d) CIGSe solar cells with point contacts and Zn(O,S) buffer layer.

5.2 Point contacts at the CIGSe/buffer interface

Figure 5.4 illustrates the schematic diagram of the five different configurations of CIGSe solar cells including the reference CIGSe cells used in this work. The buffer layers, CdS and Zn(O,S), were deposited by chemical bath deposition, and atomic layer deposition and reactive sputtering respectively. Reference CIGSe solar cells with CdS or Zn(O,S) as the buffer layers: the configuration is Mo/CIGSe/CdS or Zn(O,S)/ZnO/ZnO:Al (Figure 5.4 (a)). CIGSe cells with a layer of Al_2O_3 covering the CIGSe surface: the configuration is Mo/CIGSe/Al_2O_3/ZnO/ZnO:Al (Figure 5.4 (b)). CIGSe solar cells establishing point contacts by CdS NP's and Al_2O_3 (no CdS buffer layer): the configuration is Mo/CIGSe/CdS NP's/Al_2O_3/ ZnO/ZnO:Al (Figure 5.4 (c)). CIGSe solar cells with point contacts and CdS as the buffer layer: the configuration is Mo/CIGSe/PC-Al_2O_3/CdS/ZnO/ZnO:Al (Figure 5.4 (d)). CIGSe solar cells with point contacts and Zn(O,S) as the buffer layer: the configuration is Mo/CIGSe/PC-Al_2O_3/Zn(O,S)/ZnO/ZnO:Al (Figure 5.4 (e)).

5.2.1 Reference CIGSe devices with CdS and Zn(O,S) buffer layers

In order to study the effect of point contacts and passivation layer on CIGSe solar cell performance, 2 μm reference CIGSe solar cells are fabricated with CBD CdS and atomic layer and reactively sputtered deposited Zn(O,S), and their performance was analyzed. Depositing Zn(O,S) using ALD and RF sputtering will certainly change the interface quality (see Table 5.1). Hence, the theoretical prediction in the section 4.3.2 (refer Figure 4.6) that the quality of the interface will have an impact on the effect on the performance of the point contacts can be easily examined. For the solar cell fabrication, Cu-poor samples grown with a bulk composition of [Cu]/[[Ga] + [In]] = 0.92 were used: this corresponds to the composition for high-efficiency devices in our lab [112].

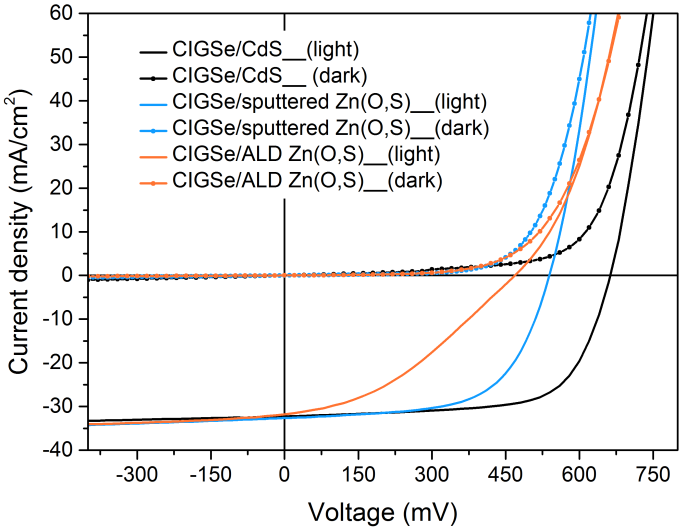

Figure 5.5: Light and dark measured $J-V$ curves of the best reference Cu(In,Ga)Se_2 solar cells with CBD CdS (black), r.f.-sputtered Zn(O,S) (blue) and ALD Zn(O,S) (orange) buffer layers.

Table 5.1: Average of the extracted $J-V$ parameters of reference CIGSe (4-13) solar cells

Sample	J_{sc} (mA/cm^2)	Voc (mV)	FF (%)	η (%)	R_s (Ωcm^2)	R_p (Ωcm^2)
CIGSe/CdS	32.1 ± 0.1	658 ± 0.2	63.3 ± 0.2	13.4 ± 0.1	0.5 ± 0.01	318 ± 150
CIGSe/ALD-Zn(O,S)	30.4 ± 0.1	421 ± 13	31.2 ± 0.4	4 ± 0.2	0.7 ± 0.1	22.3 ± 1.2
CIGSe/sputtered-Zn(O,S)	32.9 ± 0.2	537 ± 3	61.5 ± 0.1	10.9 ± 0.1	0.38 ± 0.01	364 ± 64

Figure 5.5 represents the current density–voltage graphs of the Cu(In,Ga)Se_2 solar cells, with CBD CdS, sputtered Zn(O,S) and ALD Zn(O,S) as the buffer layers, measured in dark and illumination (AM 1.5 spectrum); these cells don't have any passivation layer and will serve as the reference solar cells for the work presented in this chapter. Table 5.1 compares the corresponding cell parameters extracted from the $J-V$ curves; all solar cells have a total area of 1 cm^2.

Assuming that no Fermi-level pinning is occurring at the interface, V_{oc} is the parameter mostly affected by recombination losses at the interface. Therefore, the significant difference in the V_{oc} (refer to Table 5.1) of the devices can be attributed to the different interface formation of each buffer layer with the CIGSe; in that case, the CdS buffer layer provides the best interface quality. The layer by layer assembly of ALD Zn(O,S) is expected to provide a better interface quality with CIGSe than the sputtered Zn(O,S), however, here the

sputtered layers led to better devices. This might be because of the non-optimised deposition of ALD Zn(O,S) compared to the sputtered Zn(O,S) in our lab. The barrier in the ALD Zn(O,S) graphs might be due to an increased density of acceptor traps at the CIGSe/ALD-Zn(O,S) interface, which also explains the reduction in the V_{oc} and J_{sc}. Consequently the fill factors and the efficiencies of these devices are rather low compared to the devices with CdS and sputtered-Zn(O,S) devices. By comparing these results with those in the section 4.3.2 (see Figure 4.6), these three reference cells could represent CIGSe/buffer interfaces with three different interface qualities (refer to Figure 4.6). The device performances are well below the record efficiency CIGSe solar cells; simulations in Chapter 4 (see Figure 4.6) demonstrate that the effect of point contacts is more pronounced in interface limited solar cells. Therefore, these solar cells are suitable for validating the theoretical predictions of the influence of the point contact at the CIGSe/buffer interface.

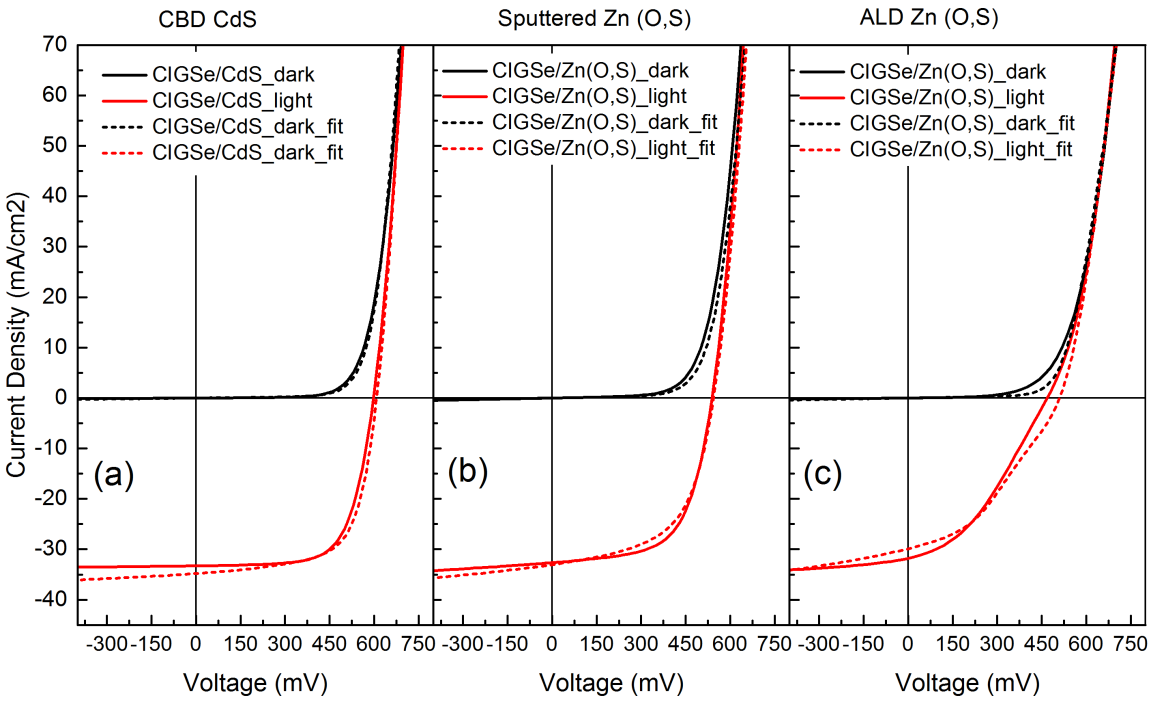

Figure 5.6: Dark and illuminated J–V curves of the reference cells (solid lines) taken from Figure 5.5 with corresponding simulated fits (dotted lines); (a) CIGSe/CdS solar cell, (b) CIGSe/sputtered Zn(O,S) and (c) CIGSe/ALD–Zn(O,S)

When comparing the numerical simulations of the experimental and fitted dark and light J–V curves of the reference solar cells (refer to Figures 5.5 and 5.6), with the illuminated J–V curves of ALD Zn(O,S), the latter is characterised by the 'S' shape anomaly, which is a clear signature of an electron barrier in the conduction band at the CIGSe/ALD–Zn(O,S)

interface. According to the simulations, refer to Figures 5.2 (e) and 5.3 (b) and (d), an electron barrier could result either from a high spike in the conduction band at the interface or from acceptor states at the CIGSe/buffer interface. Since the barrier is determined by the difference in electron affinity, χ, and $\Delta\chi$ between CIGSe and Zn(O,S) was experimentally recorded to be 0.2 eV [109], acceptor states must be responsible for the 'S' shape behaviour. This is also evident from their higher J_{01} (which is a measure of bulk and interface recombination) values of ALD Zn(O,S), extracted from the two-diode model, compared to CdS and sputtered Zn(O,S): CdS (8.17×10^{-8} mA/cm^2), sputtered Zn(O,S) (4.2×10^{-4} mA/cm^2), ALD Zn(O,S) (7.2×10^{-3} mA/cm^2). The acceptor defects could also be the reason for the reduction in V_{oc} in sputtered Zn(O,S), but indeed the concentration of these defects is much smaller compared to ALD Zn(O,S) (refer to Figures 5.2 (b) and (d)). Comparing the experimental value of V_{oc} at the CIGSe/CdS interface to the simulated values in Figure 5.2 (a), it can be estimated that the interface recombination velocity lies between 10^5 and 10^7 cm/s, which could be a reason for the low efficiency.

5.2.2 CIGSe device performance with a layer of Al_2O_3

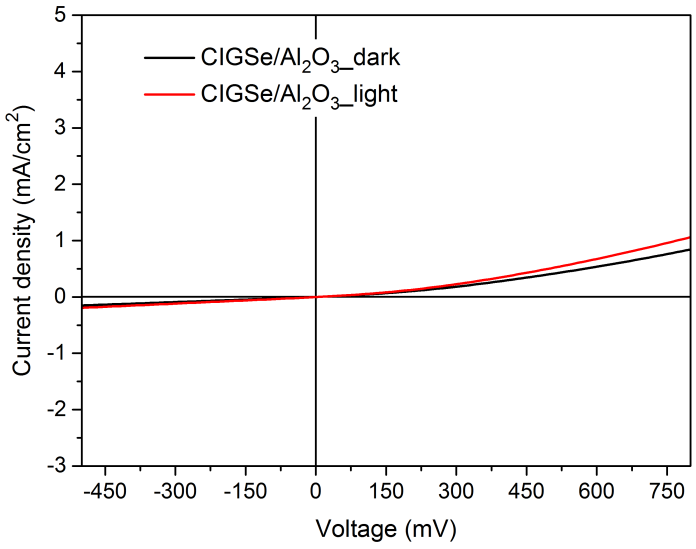

Figure 5.7: Dark and illuminated J–V curves of the solar cells with the passivation layer, Al_2O_3, covering the CIGSe absorber surface. The cell configuration is Mo/CIGSe/Al_2O_3/i-ZnO/ZnO:Al

In order to check the effectiveness Al_2O_3 as a insulating passivation layer, a layer of Al_2O_3 is deposited on top CIGSe absorber and the solar cell performance is analysed. The corresponding CIGSe solar cell configuration is Mo/CIGSe/Al_2O_3/i-ZnO/ZnO:Al as shown in Figure 5.4(b).

Table 5.2: Extracted diode parameters from the dark and light $J-V$ measurements from Figure: 5.7

Sample	J_{sc} (mA/cm^2)	Voc (mV)	FF (%)	η (%)	R_s (Ωcm^2)	R_p ($k\Omega$cm^2)
CIGSe/Al_2O_3	0	≈ 0	0	0	257 ± 87	1.6 ± 0.5

Figure 5.7 shows the J-V curves of the solar cell with Al_2O_3 covering the CIGSe surface, without any buffer layers. It can be seen that both light and dark J–V curves don't show any diode like characteristics and are non-linear at higher voltage biases, which could be from a superposition of an ohmic contact and a Schoktty barrier. The light and dark curves nearly overlap, indicating that the Al_2O_3 layer is creating a huge electron barrier at the CIGSe/Al_2O_3 interface and hence it is not photo-conductive. This is expected from the $\Delta\chi$ (> 0.4 eV) and ΔE_g (≈ 5 eV) of CIGSe and Al_2O_3 at the interface. The same behaviour is observed for all the devices with a complete layer of Al_2O_3 on CIGSe from all set of experiments with point contacts at the front interface, and hence will not be discussed separately in the following experimental sections.

5.2.3 CIGSe device performance with CdS NP's acting as the buffer layer and PC's

The configuration for this experiment follows the device structure as shown in the Figure 5.4 (c) — CIGSe/CdS- NP's/Al_2O_3/i-ZnO/ZnO:Al. In this experiment, the suitability of a configuration with CdS NP's acting as the buffer layer has been examined; if the CdS NP's could replace the state of art CdS buffer layer, then, an extra step — etching the CdS NP's — for making point contacts can be eliminated because the point contacts were already established with the deposition of a thin layer of Al_2O_3 (see Figure 5.4 (c)). CIGSe absorbers with a bulk composition of [Cu]/[[Ga] + [In]] = 0.92 were used in this experiment. The nanoparticles were deposited using the chemical bath deposition as described in section 3.5, and then, a thin film of Al_2O_3 of about 10 nm thickness is deposited using ALD. This will cover the space between the CdS particles and also above them. After this

process, the CdS NP's were not etched away. Since the ratio of nanoparticle size to the thickness of the Al_2O_3 is very large, CdS will not get completely covered by Al_2O_3 during the ALD deposition process, and the uncovered part will act as a contact with i-ZnO, enabling the current flow.

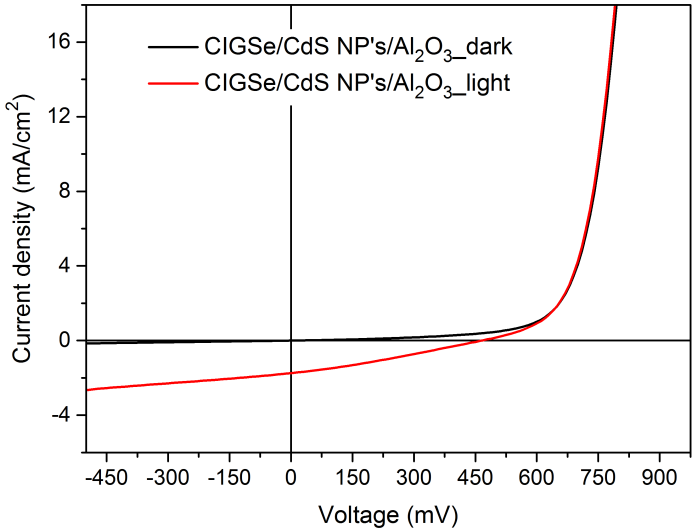

Figure 5.8: Light and dark measured J–V curves of the Cu(In,Ga)Se_2 solar cells with CdS NP's acting as the buffer layer and establishing point contacts at the CIGSe/CdS interface.

Table 5.3: Average of diode parameters of four CIGSe solar cells from the dark and light $J-V$ measurements with CdS NP's as the buffer layer

Sample	J_{sc} (mA/cm^2)	Voc (mV)	FF (%)	η (%)	R_s (Ωcm^2)	R_p (Ωcm^2)
CIGSe/CdS NP's	4 ± 1.4	418 ± 32	27.8 ± 1	0.4 ± 1	2.7 ± 0.1	292 ± 95

Figure 5.8 shows the J–V curves of the devices with point contacts established using CdS NP's under dark and on illumination. On comparing with the reference CIGSe/CdS cell (refer Table 5.1), the point contact cell has brought overall a negative impact on the electrical characteristics of the solar cell, affecting the open-circuit voltage the least. The devices exhibit poor fill-factor (27.8 ± 1), very low J_{sc} (4 ± 1.4 mA/cm^2) and as a consequence low efficiency ($\eta = 0.4 \pm 0.1$). Also, the cells exhibit a faint 'S' shape behaviour and a less prominent cross-over of the dark and light J–V curves. The cross-over arises from an electron barrier in the conduction band, which could be due to the combined effect of the barrier created by the high-band gap Al_2O_3 and the acceptor states at the interface, as shown in Figures 5.2 (a), (e) and 5.3 b. Comparing Figures 5.3 (b) and 5.8, the 'S' shape

behaviour can be shifted depending upon the acceptor density at the interface which leads to a significant decrease in J_{sc}. The barrier effect is similar to the increase in the series resistance, R_s and this is evident from the increase in the R_s (2.7 $\pm$ 0.1 Ωcm^2), and the action of defects and increased recombination at the interface lead to a decrease in the shunt resistance, R_p to 292 $\pm$ 95 Ω cm^2. However, the possibility of shunts due to a direct contact between CdS NP's and ZnO:Al can't be ruled out as the size ratio of the i-ZnO thickness to the CdS NP's is small [113].

5.2.4 CIGSe device performance with CdS buffer layer and point contacts

In this experiment, standard CdS deposited by CBD is used as the buffer layer. The device has a stack structure of Mo/CIGSe/PC-Al_2O_3/CdS/ZnO/ZnO:Al as shown in Figure 5.4 (d). CIGSe samples with a bulk composition of [Cu]/[[Ga] + [In]] = 0.94 were used in this experiment. The preparation process is outlined in section 2.2. Contrary to the standard configuration, CIGSe/CdS/i-ZnO/ZnO:Al, the point contacts are applied at the CIGSe surface as described in the section 3.5.

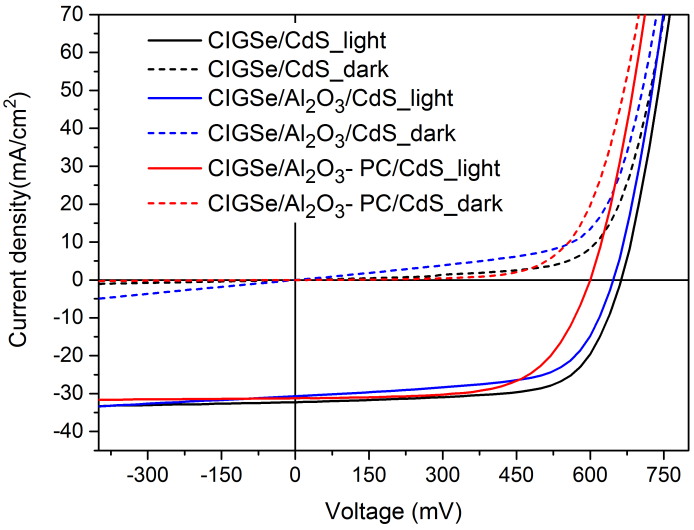

Figure 5.9: Dark and light measured current–voltage characteristics of CIGSe solar cells with CdS buffer layers, with and without point contacts. Here CIGSe/CdS corresponds to reference solar cells, CIGSe/Al_2O_3/CdS to CIGSe absorbers with a layer of Al_2O_3 and CdS over it, and CIGSe/Al_2O_3–PC/CdS to CIGSe solar cell with point contacts. The cell configurations corresponds to Figure 5.4 (a) for CIGSe/CdS light and dark and Figure 5.4 (d) for CIGSe/Al_2O_3–PC/CdS dark and light

Table 5.4: Extracted diode parameters from the light $J-V$ measurements from Figure 5.9

Sample	J_{sc} (mA/cm^2)	Voc (mV)	FF (%)	η (%)	R_s (Ωcm^2)	R_p ($k\Omega$cm^2)
CIGSe/CdS	32.1 ± 0.1	658 ± 0.2	63.3 ± 0.2	13.4 ± 0.1	0.5 ± 0.01	0.318 ± 0.15
CIGSe/Al_2O_3/CdS	31.5 ± 0.3	641 ± 1.1	60.8 ± 0.5	12.3 ± 0.0	0.52 ± 0.01	0.390 ± 0.14
CIGSe/Al_2O_3-PC/CdS	31.2 ± 0.5	589 ± 15	59.3 ± 5.5	10.9 ± 1.4	0.47 ± 0.01	0.347 ± 0.15

Figure 5.9 shows the dark and light $J-V$ characteristics of the reference and point contacted solar cells, and table 5.4 summarises their performance. Interestingly, the graphs and the cell parameters seem to show that a closed Al_2O_3 layer is conducting current, which is contrary to the non-diode characteristics seen on the Figure 5.7. In the back contact configuration, there have been reports that even after the deposition of a closed thin layer of Al_2O_3 (4 nm) layer, current is flowing through the device, but the presence of a strong kink (or S shape) is observed on those devices, from an electron barrier [114]. The electron barrier is similar to the effect of a series resistance, R_s, and R_s in all the three configurations in the Figure 5.9 have equivalent values (0.47 – 0.52 $\pm$ 0.02 Ωcm^2). Here no such barrier is observed, pointing to the fact that some alteration at the interface might have happened; this could be from any process starting from the deposition of CdS, because the point contact formation was evident from the XPS spectra and SEM images (refer to Figures 3.11 and 3.10). Whatever change had happened at the interface, it doesn't affect the solar cell performance in a positive way; the current density remains almost constant, open circuit voltage and fill factor decreases; hence, efficiency dropped compared to reference solar cells in Table 5.1.

Notably, the current density, from the $J-V$ graphs, in the case of cells with Al_2O_3 layers is getting low in the third quadrant. A possible explanation is the voltage dependence of photo-current and collection function. This means that the electron diffusion length becomes smaller and the interface recombination velocity is larger [11]; the effect of acceptor defect density on both, on reducing the space charge region extension into CIGSe can be seen in Figures 5.3 (b) and (d), and this affects the photo-current under forward bias in the fourth quadrant and therefore FF decreases. This argument is further validated by the higher leakage current in CIGSe/Al_2O_3/CdS (see Figure 5.9) compared to the reference and point-contact devices. In summary, the different behaviours of the $J-V$ curves hint towards different types of interface formation of CIGSe with Al_2O_3. This certainly puts

forwards two important questions: (1) Have the point contacts formed at the CIGSe/Al_2O_3–P.C/CdS interface? and (2) Will Al_2O_3 offer a better passivation than CdS on the CIGSe surface?.

To answer the first question, a simple experiment mimicking the experimental conditions of the CBD deposition of the CdS buffer layer is performed. Because if the interface has changed, it is most likely from the basic ammonium solution, NH_4OH, used in the CBD solution, which acts a complexing agent for the CBD reaction and a cleansing agent for the CIGSe surface oxides [115]. Under room temperature conditions and for a shorter etching time, the rate of removal of Al_2O_3 is very small in NH_4OH solution [116], but the standard CdS CBD process at 60°C might have changed the reaction kinetics.

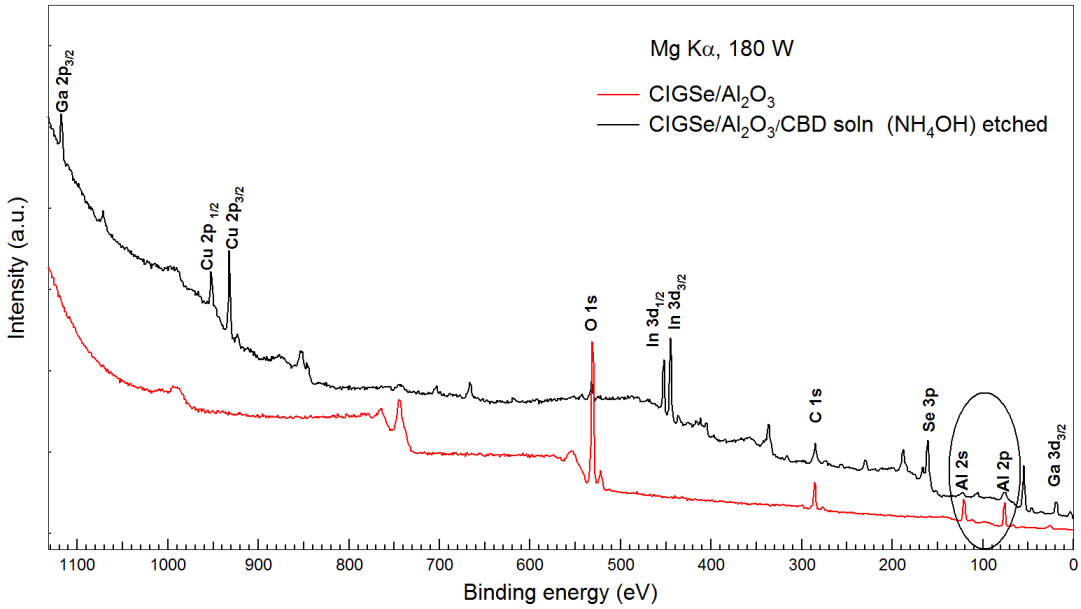

Figure 5.10: XPS survey spectra of a Cu(In,Ga)Se_2 sample, measured with Mg Kα X-ray source (hν=1253.6 eV), before and after dipping the CIGSe samples in CBD solution containing NH_4OH; the resurgence of core peaks can be clearly seen.

A CIGSe absorber with a thin closed layer of Al_2O_3 (10 nm) is taken and dipped in a solution with the same concentration and amount of NH_4OH as used in the CBD solution, keeping the same deposition time and temperature and without using the precursors, $Cd(acac)_2$ and thiourea. Then, the sample is examined under XPS to see the differences before and after the CBD reaction. The XPS spectra of the absorber with a thin closed layer of Al_2O_3 before and after the CBD treatment is depicted in Figure 5.10. Note that any signal from

Cd was absent in the spectrum because $Cd(acac)_2$ and thiourea were not mixed in the solution. The XPS spectra have revealed that during the chemical bath deposition, the thin layer of Al_2O_3 got severely etched — a significant reduction in the O1s peak and almost complete removal of Al 2s and Al 2p peaks is observed, leading to the reappearance of the elemental core peaks in CIGSe. The attack of OH^- ions from the NH_4OH etch the Al_2O_3 layer and produce $Al(OH)_3$. Therefore, the presence of NH_4OH in CBD solution changes a passivated CIGSe/CdS interface with Al_2O_3 to an unpassivated CIGSe/CdS interface: this explains the conducting behaviour in the fully passivated CIGSe surface. However, etching will not bring back the original interface character of an unpassivated CIGSe/CdS interface because there is still Al present on the surface, and this could be correlated to the negative influence on the cell properties of a fully passivated and partially passivated point contacts devices.

5.2.5 CIGSe device performance with Zn(O,S) buffer layer and point contacts

Since NH_4OH in the CBD solution for depositing CdS buffer layer is not suitable for the Al_2O_3 layer, in this section, dry deposition methods like sputtering and atomic layer deposition are considered for the buffer layer deposition. Zn(O, S) is the buffer layer chosen for this experiment because it is the most promising buffer layer after CdS and has reached efficiencies up to 20% [117]. The devices have the following stack structure: Mo/CIGSe/PC-Al_2O_3/Zn(O, S)/ZnO/ZnO:Al, as shown in Figure 5.4 (d). Like in the previous experiments, the thickness of the Al_2O_3 was maintained at 10 nm. Using Zn(O, S) as the buffer layer also gives the opportunity to validate the theoretical outcome from the chapter 4 (refer Figure 4.6) that the point contacts are more effective when there is a cliff at the interface — under oxygen rich conditions during the deposition of Zn(O, S), a cliff can be formed at the CIGSe/Zn(O, S) interface, otherwise a spike is formed [109–111]. The influence of the distance between the point contacts was also studied and moreover depositing the Zn(O, S) using ALD and reactive sputtering will certainly change the interface quality and hence its effect on point contacts is examined.

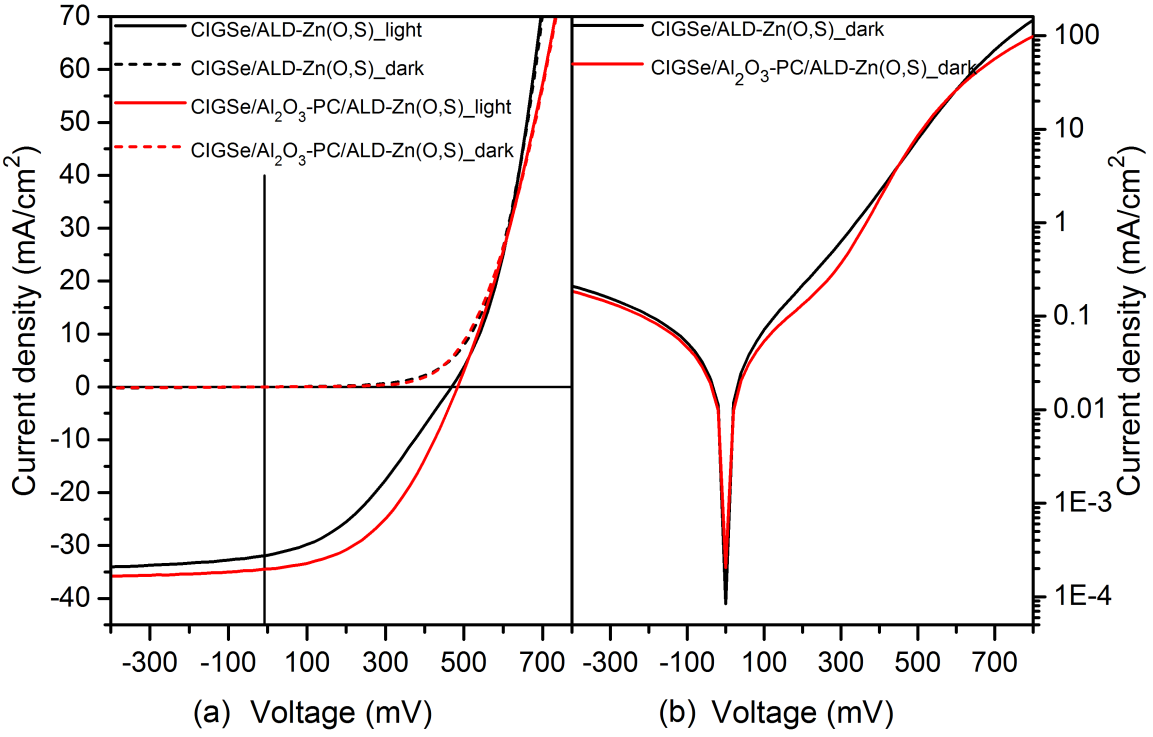

Figure 5.11: Dark and light measured J–V graphs of the best Cu(In,Ga)Se_2 solar cells with ALD Zn(O, S) buffer layer with and without point contacts. Here CIGSe/ALD Zn(O,S) (see Figure 5.4 (a)) stands for reference CIGSe solar cells with Zn(O,S) buffer layers and CIGSe/Al_2O_3–PC/ALD Zn(O,S) (see Figure 5.4 (e)) corresponds to CIGSe absorbers with point contacts and Zn(O,S) buffer layers.

Table 5.5: Average of the extracted $J-V$ parameters of Cu(In,Ga)Se_2 solar cells (13) with ALD Zn(O,S) buffer layer and point contacts.

Sample	J_{sc} (mA/cm^2)	Voc (mV)	FF (%)	η (%)	R_s (Ωcm^2)	R_p (Ωcm^2)
CIGSe/ALD Zn(O,S)	30.4 $\pm$ 0.1	421 $\pm$ 13	31.2 $\pm$ 0.4	4 $\pm$ 0.2	0.7 $\pm$ 0.1	22.3 $\pm$ 1.2
CIGSe/Al_2O_3–PC/ALD Zn(O,S)	30 $\pm$ 1.5	403 $\pm$ 4.8	43 $\pm$ 1.1	5.3 $\pm$ 0.4	0.9 $\pm$ 0.1	239 $\pm$ 50

ALD-Zn(O,S): Figure 5.11 shows the J–V curves of the solar cells with point contacts and ALD Zn(O,S) as the buffer layer in dark and illumination. On comparing with the reference Zn(O,S) cell without an Al_2O_3 passivation layer, there exists a visible change in the J–V curves in the fourth quadrant — the 'S' shape character is removed by the application of the point contacts with the passivation layer. This is quite surprising as a barrier can be only nullified by the influence of donor charges (refer to Figure 5.3 (f)) at the interface or by a reduction of acceptor defects. By analysing the dark J–V curves the leakage current, J_{01} was found to be one order lower as compared to reference cells — 7.28 $\times$ 10^{-3} mA/cm^2

for reference and 6.54$\times$ 10^{-4} mA/cm^2 for point contact devices. Another expected change is in the series resistance of the devices; it has increased from 0.656 Ωcm^2 to 2.07 Ωcm^2; however this didn't affect the current collection in the devices. The effect of removal of the 'S' shape anomaly can be seen in the increased value of the FF, and thus efficiency is increased by 1.3%. Yet, it is not clear whether the interface quality is improved, as we can see that the V_{oc} is affected on the contrary (refer to Table 5.5).

Sputtered Zn(O,S): The interface quality also depends on the method with which the buffer layers are deposited. Reactive sputtering of Zn(O,S) buffer layer could bring a different interface quality compared to ALD. Since ALD is considered to create layer by layer assembly of the depositing material on the substrate, the substrate surface is expected to have a reduced number of defects, whereas sputtering brings the opposite effect. And hence the theoretical prediction in the Figure 4.6 that a interface limited device will get a more beneficial effect from point contact solar cell than a high efficiency solar cell can be validated. Figure 5.12 represents the $J-V$ graphs of sputtered Zn(O,S) on top of point contacts,

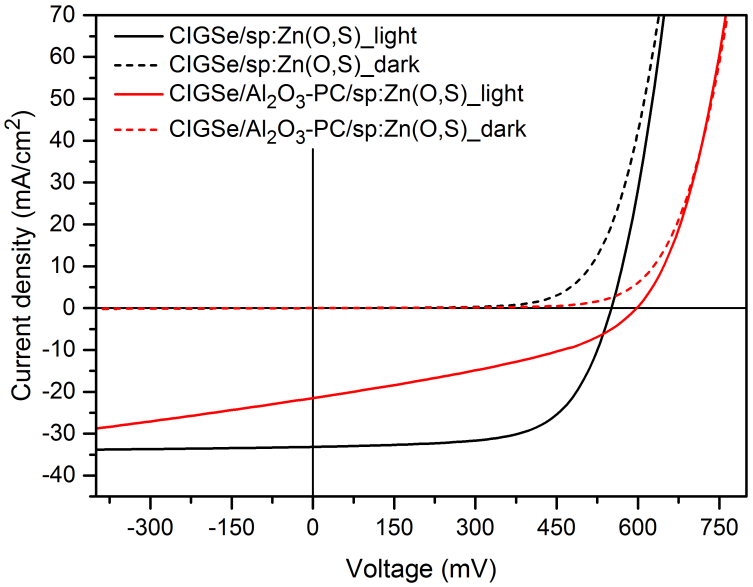

Figure 5.12: Current voltage characteristics of reference CIGSe solar cell (CIGSe/sp:Zn(O,S)) and point contact CIGSe solar cell (CIGSe/Al_2O_3–PC/sp:Zn(O,S)) with sputtered Zn(O, S) as the buffer layer, measured under dark and light conditions.

and their corresponding data are tabulated in Table 5.6. At a first glance, a reduction in the shunt resistance is observed in samples with point contacts at low voltage biases [V$<\approx 0.5$ V]. However, in contrast to ALD Zn(O,S), a clear enhancement in V_{oc} (56 mV) is observed, pointing towards an improvement in interface quality. This must be due to the protection

given by the Al_2O_3 layer to the CIGSe surface from the defects formation while sputtering. But a drastic reduction in efficiency is observed from 10.9% to 3.7%, mainly arising from the decrease in current density and shunt resistance.

Table 5.6: CIGSe solar cell parameters extracted from the dark and light measurements from Figure 5.12

Sample	J_{sc} (mA/cm^2)	Voc (mV)	FF (%)	η (%)	R_s (Ωcm^2)	R_p (Ωcm^2)
CIGSe/sp:Zn(O,S)	32.9 ± 0.2	537 ± 3	61.5 ± 0.1	10.9 ± 0.1	0.38 ± 0.01	364 ± 64
CIGSe/Al_2O_3-PC/sp:Zn(O,S)	17.1 ± 2.5	593 ± 3	35.5 ± 1.1	3.7 ± 0.6	0.47 ± 0.2	54 ± 6

The devices with point contacts show a shift in the photo-current decay in the fourth quadrant; also, the injection current is shifted to higher voltages. This means that the photo-current and hence the collection function are voltage dependent. Moreover, the dark and illuminated J–V curves cross each other at higher injection, which is an indication of an electron barrier in the conduction band. According to the simulations results presented in Figures 5.2 and 5.3, these barriers could arise from two possibilities; because of the strong $\Delta\chi$ (0.6 eV) between CIGSe and Al_2O_3 or due to an increased number of acceptor states shifting the photo-current decay by raising the photo-barrier at the point contacts. It is explained in the Chapter 4 (refer to Table 4.2) that the donor charges from the passivation layer can influence the band bending at the CIGSe/point contact interface. This is valid for the acceptor too; here instead of a band bending leading to an inversion, these charges reduce inversion and create an accumulation of electrons at the interface. This will invert the quasi-electron Fermi-level at the interface and the electrons will flow back to the absorber, where they will recombine.

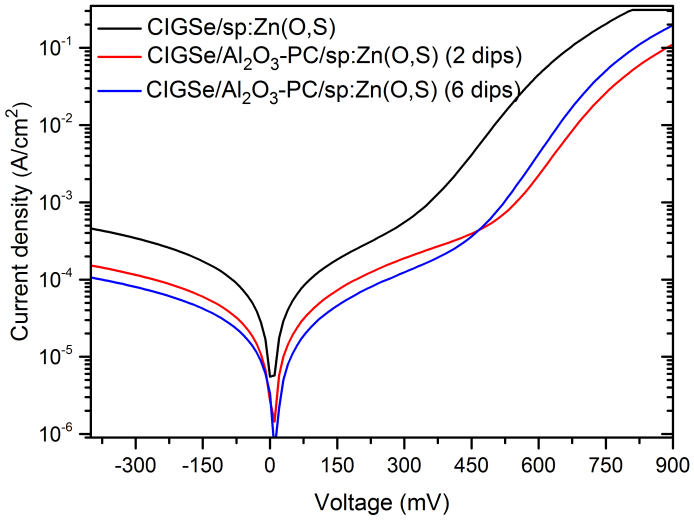

Figure 5.13: (a) Logarithmic plot of dark J-V characteristics of CIGSe reference (CIGSe/sp:Zn(O,S)) and point contacts solar cells (CIGSe/Al_2O_3–PC/sp:Zn(O,S)) with sputtered Zn(O,S) buffer layer for different surface area coverage; here 2 dips and 6 dips stands for the number of cycles the CIGSe absorbers are dipped in CdS NP's solution for point contacts fabrication, which corresponds to a high and low coverage area of passivation layer of 83% and 61% respectively.

Table 5.7: Fit parameters, according to the two-diode model, of the dark $J-V$ curves of front point contact CIGSe solar cell with sputtered Zn(O,S) as the buffer layer extracted from Figure 5.13. The percentage values in the brackets represents coverage area of the passivation layer.

Sample	A_1	J_{01} (mA/cm^2)	A_2	J_{02} (mA/cm^2)	Rs (Ωcm^2)	Rp (kΩcm^2)
CIGSe/sp:Zn(O,S) (0%)	1.98	5.17×10^{-4}	14.66	6.66×10^{-2}	0.503	1.043
CIGSe/Al_2O_3-PC/sp:Zn(O,S) (83%)	1.51	3.23×10^{-7}	9.04	4.43×10^{-2}	1.857	4.265
CIGSe/Al_2O_3-PC/sp:Zn(O,S) (61%)	1.64	2.68×10^{-6}	7.04	1.5×10^{-2}	0.928	5.070

The increase in the V_{oc} can also be related to the increase in the acceptor states. In Figures 5.2 (d) and (f), we discussed this phenomenon. This means that under illumination, a high recombination zone is created for the photo-generated minority carriers, because the the concentration of holes exceeds that of the electrons, and they will be the majority carriers at the interface too. As shown in simulations, the recombination has a maximum when n=p, but if one of the carrier concentrations dominates the other, recombination is reduced; this is clearly shown in Figures 5.2 (d) and (e). This is also clear from the analysis of the dark J–V curves of the reference and point contact solar cells using a two-diode model; as displayed in Table 5.7, the saturation current density, J_{01} is reduced by three decades, the main diode quality factor, A_1 also got improved compared to the reference device.

Consequently, V_{oc} is enhanced. This also depends on the percentage of area passivated; for a lower coverage of Al_2O_3 on the CIGSe surface, the V_{oc} is clearly mitigated (see Table 5.6). Also, in this case the potential barrier created by the acceptor density flattens the 'S' shape characteristic and shifts it to the third quadrant. The increase in V_{oc} is further

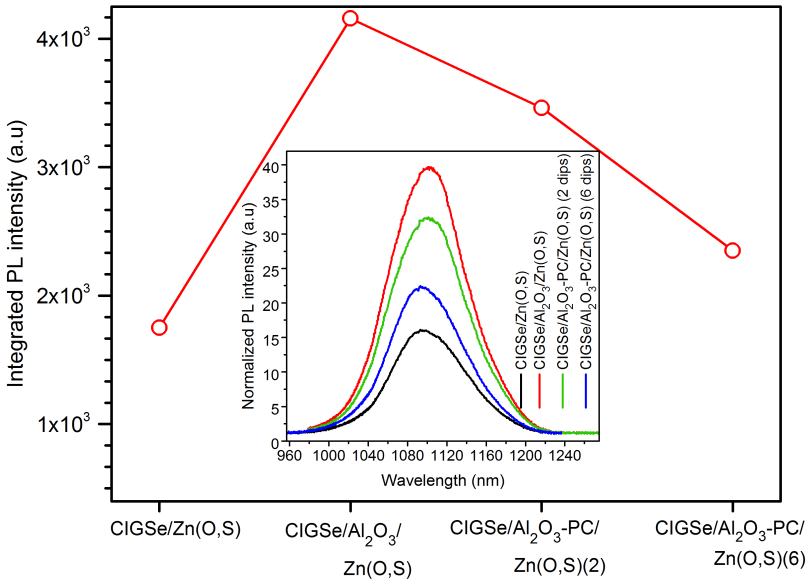

Figure 5.14: Integrated photoluminescence intensities of the samples from 5.7; inset shows the photoluminescence intensity versus energy; 2 dips corresponds to approx. 83% and 6 dips to 61% coverage area of PaL.

correlated with the photoluminescence intensity, as both are proportional to an increase in charge carrier density; hence the photoluminescence yield is a direct measure of interface quality. So to clear out the ambiguity, photoluminescence measurements were done on all samples. The results are in agreement with above discussion because an enhancement in photoluminescence is observed for devices having an Al_2O_3 passivation layer or Al_2O_3 with point contacts compared to the reference CIGSe devices as shown in Figure 5.14. From Figures 5.3 (c)–(e), it was evident that the acceptor states at the interface or in the buffer can raise the hole concentration at the interface and affect the V_{oc}. Considering this, the increase in photoluminescence and the corresponding V_{oc}, it can be seen that the charge carrier generation is proportional to the Al_2O_3 coverage (see Figure 5.14): the higher the Al_2O_3 coverage, the better is the V_{oc}. This is one of the reasons why a high coverage area of point contacts under-perform in terms of V_{oc} to a low coverage area of point contacts.

Remarkably, the shunt resistances calculated in the dark $J-V$ for the point contact solar cells in Table 5.7 are in contrast with the light $J-V$ measurements presented in Table 5.6. This also indicates the presence of illumination dependent shunt paths responsible for a drastic reduction in the J_{sc}. The reflection losses from the Al_2O_3 layer are also taken into account for the current loss analysis, with the aid of simulations based on the transfer matrix-method. In these simulations CIGSe surfaces and interfaces are considered to be flat. From the simulations, it is found that the new stack structure, Al_2O_3 between CIGSe and buffer layer, slightly increases the amount of reflection. An equivalent reduction of current density of 1 mA/cm^2 is calculated from the absorption profile. Therefore, it can be deduced that reflective losses are not the primary reasons for J_{sc} losses.

5.3 Summary

CIGSe solar cells with point contacts at the front interface $\left(\text{at the CIGSe/buffer}\right)$ were made. Point contacts made through a Al_2O_3 passivation layer are intolerant towards the chemical bath deposition of CdS buffer layer, because of the NH_4OH present in the CBD solution can etch out the Al_2O_3 layer. Also, the point contacts are applied along with Zn(O,S) as the buffer layer (deposited using ALD and sputtering). An improvement in power conversion efficiency is witnessed for ALD Zn(O,S), however, the V_{oc} didn't show any improvement, which can be attributed to an unoptimised ALD Zn(O,S) buffer layer deposition. With a sputtered Zn(O,S) buffer layer, it is found that the point contacts can increase the V_{oc}, mainly due to an upward band bending rather than a needed enhanced inversion at the interface, and also give rise to light-induced voltage dependent shunt paths, which drastically reduces the overall cell performance.

6

Incorporation of point contacts at the Mo/CIGSe interface of thin CIGSe devices

Scaling down 2-3 μm thick CIGSe absorber to a few hundreds of nanometers can help to overcome the problems of material cost — mainly high due to indium and gallium scarcity — and gives the flexibility in the fabrication process, which indeed reduces the manufacturing cost by material reduction and higher throughput [118–120]. So far, this approach hasn't been able to produce high efficiency ultra-thin CIGSe solar cells, because their efficiency is limited by incomplete absorption and back contact recombination [99, 121, 122].

The enhancement in the rear contact recombination, at the CIGSe/Mo interface, occurs when the absorber thickness is comparable to the diffusion length of the carriers. This problem is mainly encountered by grading the Ga/[Ga+In] ratio, which creates a potential barrier for minority carriers diffusion; an alternate technique that could address this problem is a point contact structure through a passivation layer at the rear interface, Mo/CIGSe. The passivation layer creates a back surface field which repels electrons approaching the back contact — a concept that was found to be effective in ultra-thin CIGSe solar cells [52]. Also, simulations in section 4.4 show that a maximum of 50 mV in V_{oc} can be achieved if the interface recombination is reduced from 10^6 cm/s to 10^3 cm/s. In this chapter, we applied an industry viable low cost self-assembled point contact technology method using CdS NP's (refer to section 3.5) at the back interface, and investigate its influence on the solar cell performance.

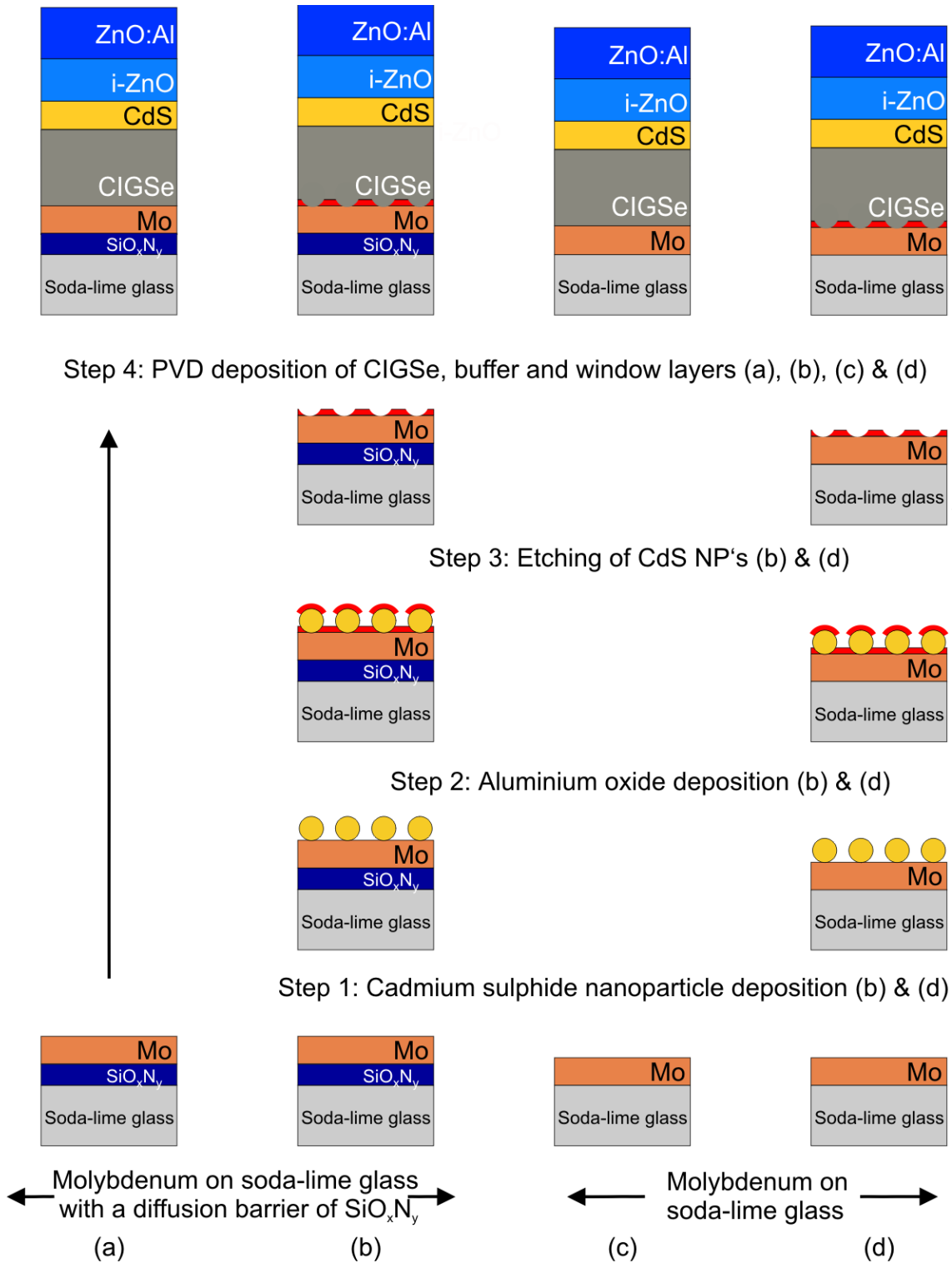

Figure 6.1: From bottom to top: steps involved in making point contacts at the Mo/CIGSe interface: (a) CIGSe reference sample with standard deposition procedure, (b) Sample with molybdenum along with point contacts fabrication.

6.1 Point contacts at the Mo/CIGSe interface

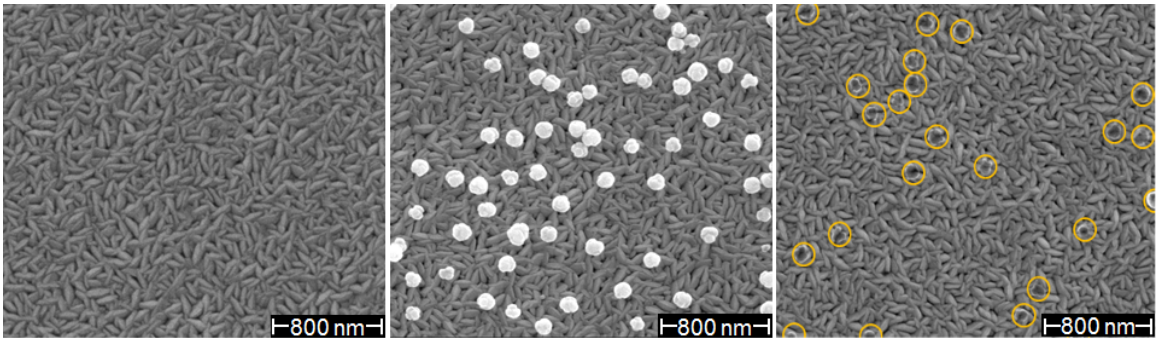

Figure 6.2: SEM images showing different stages of making point contacts (a) Reference sample with molybdenum, (b) CdS NP's on top of molybdenum and (c) point contacts formed after the deposition of Al_2O_3 followed by etching out the CdS NP's.

Figure 6.1 describes the steps involved in the fabrication of a rear passivated ultra-thin solar cell with localized point contacts; the unpassivated reference solar cells are made avoiding the steps 3, 4 and 5 in the sequence. After the deposition of CdS NP's, Al_2O_3 is deposited using ALD for around 100 cycles which leads to approximately 10 nm thickness as estimated by ellipsometry measurements; a higher thickness is not preferred because it impedes the etching process of CdS NP's and also can blister during the three-stage co-evaporation of CIGSe. The CIGSe layer deposited on the top of the Mo/point contact structure fills the nanoholes and enables good electrical contact with the Mo. Figure 6.2 shows the SEM images of different stages in making point contacts at the back interface of CIGSe solar cells; the CdS NP's assembling capability on a relatively smooth surface like molybdenum is better compared to the rough CIGSe. The formation of point contacts is further validated with XPS measurements, which are not shown here.

6.1.1 Thinner CIGSe device performance with point contacts at Mo/CIGSe interface

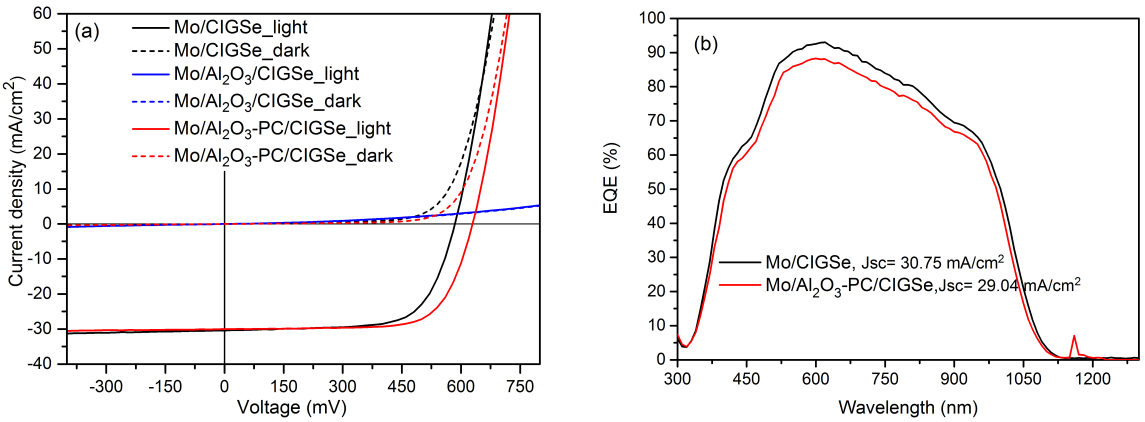

Figure 6.3: (a): current-voltage characteristics of 900 nm thick CIGSe layer solar cells: unpassivated reference cells (black) and reference with Al_2O_3 back interface passivated cells with (red) and without (blue) point contacts measured under dark and light conditions, and (b) corresponding EQE spectra; here PC refers to point contacts.

Table 6.1: 900 nm thin-film CIGSe solar cell parameters, with and without rear passivation, obtained from the $J-V$ curves shown in Figure 6.3; PC refers to point contacts.

Sample	J_{sc} (mA/cm^2)	Voc (mV)	FF (%)	η (%)	Rs (Ωcm^2)	Rp (Ωcm^2)
Mo/CIGSe	30 ± 0.1	575 ± 5	66.3 ± 1.6	11.4 ± 0.3	0.62 ± 0.2	477 ± 69
Mo/Al_2O_3/CIGSe	0	0	0	0	141 ± 33	856 ± 50
Mo/Al_2O_3-PC/CIGSe	29.6 ± 1.4	615 ± 5	71.7 ± 0.7	13 ± 0.1	0.65 ± 0.03	814 ± 49

In this experiment, a CIGSe absorber layer of 900 nm (estimated using confocal microscopy) is deposited on top of the Mo with back point contacts. Before the deposition of the Mo onto the glass substrate, a diffusion barrier of SiO_xN_y is coated on the glass substrates. Since Na is reported to influence the growth kinetics, passivation of the grain boundaries, net carrier concentration, and minority-carrier traps [123], Na is incorporated into the CIGSe by a NaF treatment after the three-stage co-evaporation process of the absorber.

The $J-V$ plots of the champion devices from the unpassivated and localized rear passivated point contact (LRPC) structures, produced in the same deposition batch, are shown in Figure 6.3 (a). Table 6.1 summarizes the averaged data extracted from $J-V$ plots, of 12 such cells. As expected, a current blocking behaviour, due to the increased series resistance (refer Table 6.1)), can be observed on the samples with a closed layer of Al_2O_3. The

overall shape of the unpassivated and rear passivated point contact structures are alike; the J_{sc} values of the both devices are comparable; however, the V_{oc} of the passivated point contact structure is enhanced $\approx$ 39 mV, and the fill factor is increased from 66.3 to 71.7 — could be due to an increase in the shunt resistance and V_{oc}. This led to an overall increase in efficiency from 11.4 to 13%. It is noteworthy that the shunt resistance, R_p, is improved from 439 to 805 Ω cm^2; nevertheless this didn't contribute to an increase in J_{sc}.

To see the range in which the spectral response has negatively affected the J_{sc} values, EQE measurements of the devices were done as shown in Figure 6.3 (b). Overall, there is a slight decrease in the EQE over the entire spectra. This is quite strange for the CIGSe absorbers fabricated in the same PVD process; yet, there might be two possibilities: it could be from a difference in the charge carrier concentration or Ga/[III] profile: Ga/[III] profiles can influence the absorption coefficient [120]. Therefore, both were examined to see their influence on the J_{sc}. The C – V graphs in Figure 6.4 show only a negligible deviation in the capacitance at higher voltage biases, and this doesn't translate into a significant difference in the charge carrier density in the CIGSe bulk, which was calculated (using $N_{CV,d_{SCR}} = -C^3/(\epsilon \cdot \varepsilon \cdot A^2 \cdot dC/dV)$) to be 2.49 e+15 cm^{-3} for the reference and 2.17 e+15 cm^{-3} for the point contact devices. The Ga/[III] depth profiles measured using GDOES is shown in Figure 6.5 (b). Again the curves show similar trends; however, a close look shows a slight difference in the minimum band gap at the notch point. Considering this and correlating with the absorption coefficient dependence on Ga/[III] profiles [120], a slight difference is possible for the J_{sc} values. Also, note the decrease in the spectral response above 700 nm observed for 900 nm thin film solar cells compared to the standard 2μm thin film devices, and this can be ascribed to the incomplete reflection and parasitic absorption of the molybdenum layer; a calculation of J_{sc} values from the EQE curves suggests that a 5 mA/cm^2 deficit is accounted for the 900 nm-thin film CIGSe devices.

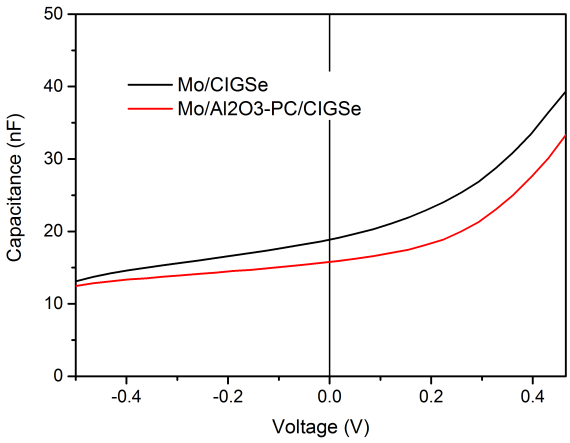

Figure 6.4: Capacitance–voltage curves of reference CIGSe and back point contact CIGSe solar cell recorded at 1 KHz and 293K.

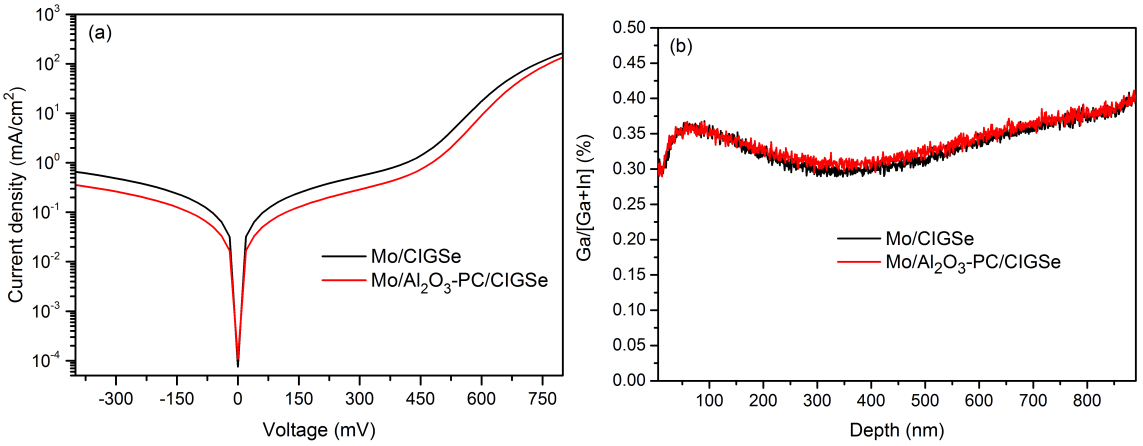

Figure 6.5: (a) Dark J-V characteristics of 900 nm thin CIGSe solar cell with and without point contacts at the Mo/CIGSe interface (b) Glow Discharge Optical Emission Spectroscopy (GDOES) measurements of the corresponding samples.

Table 6.2: Fit parameters according to the two diode model of the dark JV curves of the rear locally passivated solar cells and its corresponding reference CIGSe solar cells with thickness of 900 nm, as shown in the Figure 6.5 (a).

Sample	A_1	J_{01} (mA/cm^2)	A_2	J_{02} (mA/cm^2)	Rs (Ωcm^2)	Rp (kΩcm^2)
Mo/CIGSe	1.50	3.7×10^{-6}	3.29	1.2×10^{-3}	0.760	0.62
Mo/Al_2O_3-PC/CIGSe	1.41	4.9×10^{-7}	2.67	3.3×10^{-4}	0.762	1.2

Referring to the simulations in the Figure 4.11, it can be approximated that the interface recombination velocity gets decreased to the range between 10^3– 10^4 cm/s from a value close to 10^7 cm/s. Further, to corroborate whether the increase in V_{oc} is due to the reduction in the back interface recombination, $J-V$ measurements are conducted in the dark and a two-diode model is used to fit the data as shown in Figure 6.5 (a); the fit parameters are given in the Table 6.2. In order to avoid the ambiguity in gallium grading, the Ga/[Ga+In] ratio is also plotted as a function of depth in Figure 6.5 (b). An identical gallium grading is noted for both. Therefore, this parameter need not be considered in the recombination analysis and hence limits the discussion only to the dark $J-V$ curves. From the Table 6.2, it can be noted that the diode quality factor is improved (1.50 to 1.41 for back point contact devices) and the saturation current density, J_{01}, decreased by a decade. Also, the shunt resistance almost doubled with point contact devices. By expressing V_{oc} of the main diode as $V_{oc} \approx (AkT/q) \cdot In(J_{sc}/J_{01})$ and solving it for the best cells (Reference V_{oc} = 585, point contact device V_{oc} = 629 mV) in each category, a factor of 1.06 rise should be seen in the V_{oc} of the rear point contact solar cells, which amounts to 33 mV, which fits to the experimentally measured V_{oc} of reference and point contact device. Therefore, this gives a clear confirmation that the back interface recombination is reduced by the application of the back point contacts.

Table 6.3: 900 nm thin CIGSe solar cell parameters with and without point contacts at the Mo/CIGSe interface, for different surface area coverage of Al_2O_3 $PC_{H\pi,H\alpha}$ ($\pi \approx 40\%$, $\alpha = 60$ nm), $PC_{H\pi,L\alpha}$ ($\pi \approx 40\%$, $\alpha = 45$ nm), $PC_{L\pi,H\alpha}$ ($\pi \approx 17\%$, $\alpha = 60$ nm) – π denotes area and α denotes point contact opening radius. Here Mo/CIGSe stands for the reference CIGSe solar cells.

Sample	J_{sc} (mA/cm^2)	Voc (mV)	FF (%)	η (%)	Rs (Ωcm^2)	Rp (Ωcm^2)
Mo/CIGSe	30 ± 0.1	575 ± 5	66.3 ± 1.6	11.4 ± 0.3	0.62 ± 0.2	477 ± 69
Mo/Al_2O_3-$PC_{H\pi,H\alpha}$/CIGSe	29.6 ± 1.4	615 ± 5	71.7 ± 0.7	13 ± 0.1	0.65 ± 0.03	814 ± 49
Mo/Al_2O_3-$PC_{H\pi,L\alpha}$/CIGSe	29.4 ± 0.2	595 ± 4	70.6 ± 0.1	12.3 ± 0.1	0.56 ± 0.04	661.8 ± 50
Mo/Al_2O_3-$PC_{L\pi,H\alpha}$/CIGSe	29.8 ± 0.7	592 ± 1	70.2 ± 0.7	12.8 ± 0.2	0.52 ± 0.02	544 ± 42

Influence of surface area coverage: The influence of the surface area coverage, i.e. the distance between the particles is a particular parameter of interest, along with radii of the nano-contact openings (two radii were considered: 60 nm and 45 nm). The particles distances were tuned by varying the dipping cycles during the deposition process of CdS NP's. Thus, three categories were created: (1) a high coverage area, $H_\pi, \pi \approx 40\%$, and large radius, $H_\alpha, \alpha = 60nm$, (2) High coverage area, $H_\pi, \pi \approx 40\%$, and small radius, $L_\alpha, \alpha =$

$45nm$, (3) low coverage area, $L_\pi, \pi \approx 17\%$ and large radius $L_\alpha, \alpha = 60nm$. Here higher π corresponds to six times dipping and low π denotes two times dipping in CdS NP's solution. Table 6.3 shows the tabulated values of the Figure of Merit of solar cells from these three classes. The coverage area π and α had hardly any effect on the solar cell parameters; this is contrary to the belief that the distances between the point contacts should be smaller than the diffusion length. These results points to the fact that in addition to the passivation effect provided by the Al_2O_3, it creates a back surface field, from its negative charges, repelling the electrons approaching the back contact. Thus the hole diffusion length is increased; similar results were reported lately by Casper et al, where they showed a pitch distance of 10 μm didn't affect the diffusion of majority carriers[54].

Influence of Sodium: Sodium is vital for the grain growth in CIGSe and was found to have a direct impact on V_{oc} [124]. It is either diffused from the glass substrate or incorporated into CIGSe by a post deposition treatment. And employing point contact structures could have a negative effect on the the diffusion of sodium from the glass substrate. To study this effect in rear point contact structures, two kinds of substrates were used: substrates with and without a diffusion barrier of $SiNO_x$. Only the glass substrate with a diffusion barrier was given a NaF post deposition treatment. The CIGSe absorbers were produced in the same batch and the thickness was reduced compared to the last experiment (absorber thickness = 900 nm) and estimated to be 650 nm from confocal microscopy measurements.

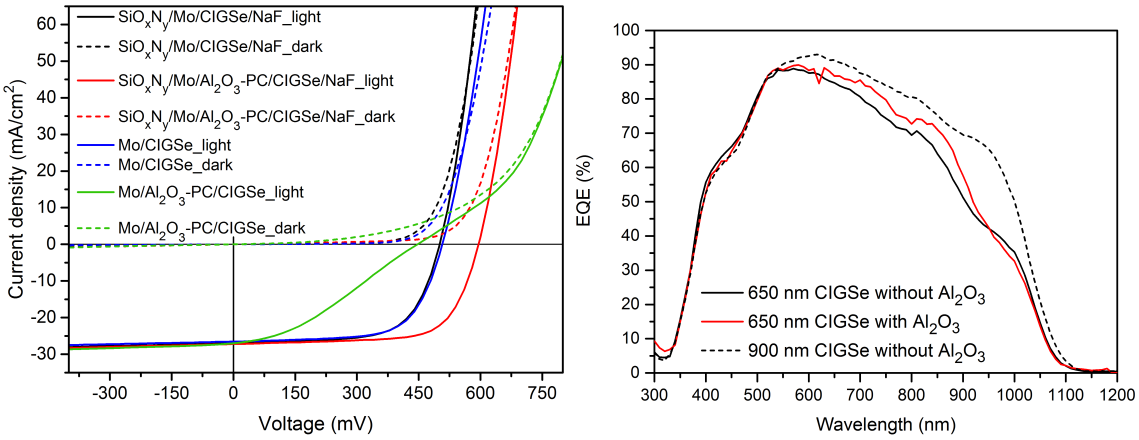

Figure 6.6: (a) $J - V$ curves of a 650 nm thin CIGSe solar cells with and without a SiO_xN_y barrier and point contacts (b) EQE spectra of ultra-thin CIGSe solar cells with a barrier and with (red) and without (black) LRPC's. The dotted lines represent EQE spectrum from a 900 nm thick CIGSe absorber.

Table 6.4: 650 nm thin CIGSe solar cell parameters with and without point contacts at the Mo/CIGSe interface, with and without a barrier against Na diffusion: $PC_{H\pi,H\alpha}$ ($\pi \approx 40\%, \alpha = 60$nm) – π denotes the coverage area and α denotes the point contact opening radius. Here *SiO_xN_y*/Mo/*CIGSe* and Mo/CIGSe are the reference CIGSe solar cells with and without a barrier of *SiO_xN_y* between soda-lime glass and molybdenum.

Sample	J_{sc} (mA/cm^2)	*Voc* (mV)	*FF* (%)	η (%)	Rs (Ωcm^2)	Rp (Ωcm^2)
SiO_xN_y/Mo/*CIGSe*	26.9 ± 0.3	496 ± 11	63.2 ± 0.6	8.4 ± 0.1	0.48 ± 0.03	189 ± 21
SiO_xN_y/Mo/Al_2O_3-PC/CIGSe	27.6 ± 0.1	601 ± 5	66.3 ± 0.5	11 ± 0.1	0.87 ± 0.15	326 ± 27
Mo/CIGSe	27 ± 0.3	480 ± 9	60.1 ± 1.4	7.8 ± 0.3	0.67 ± 0.01	230 ± 18
Mo/Al_2O_3-PC/CIGSe	26.1 ± 0.3	445 ± 36	38.8 ± 1.4	5 ± 0.6	2.7 ± 0.2	250 ± 65

Figure 6.6 shows the $J - V$ performances of ultra-thin solar cells with point contacts at the back interface, and with and without a sodium barrier. The reference cells from both batches, without Al_2O_3 passivation, have comparable cell characteristics. But, the two had entirely different characteristics when point contacts are applied. Mainly the barrier in the fourth quadrant, showing the lack of Na, is observed for the cells without a barrier and no post deposition NaF treatment [125]. Consequently, the V_{oc} is reduced. At the same time, with the barrier case and post NaF treated samples, a surge in V_{oc} (Δ = 0.1 V) is witnessed. Table 6.4 gives an overview of the solar cell parameters. Point contacts at the back interface show a positive effect on the J_{sc} of the cells possibly due to the decrease in the current leakage at the back interface because of the Al_2O_3 layer. This can be seen in the increase in the shunt resistance values (251.2 to 308.3 Ωcm^2). Advantageous effects of point contacts are observed in FF (63.2 to 66.3). Overall, the efficiency jumped from 8.4 to 11%. Comparing the two substrates, it is clear that the Al_2O_3 layer can impede the diffusion of sodium from the glass substrate and it should be supplied to the absorber before or after the co-evaporation process.

Table 6.5: Fit parameters according to the two diode model of the dark J – V curves of the rear locally passivated solar cells and its corresponding reference, as depicted in the Figure 6.5.

Sample	A_1	J_{01} (mA/cm^2)	A_2	J_{02} (mA/cm^2)	Rs (Ωcm^2)	Rp (kΩcm^2)
SiO_xN_y/Mo/CIGSe	1.48	2.5×10^{-5}	6.0	6.2×10^{-3}	0.473	1.1
SiO_xN_y/Mo/Al_2O_3-PC/CIGSe	1.42	1.4×10^{-6}	7.5	2.8×10^{-2}	0.642	0.75

The increase in V_{oc} is a direct indication of the interface improvement. But the overall betterment of the cell is also due to the reduction in the parasitic absorption at the back contact

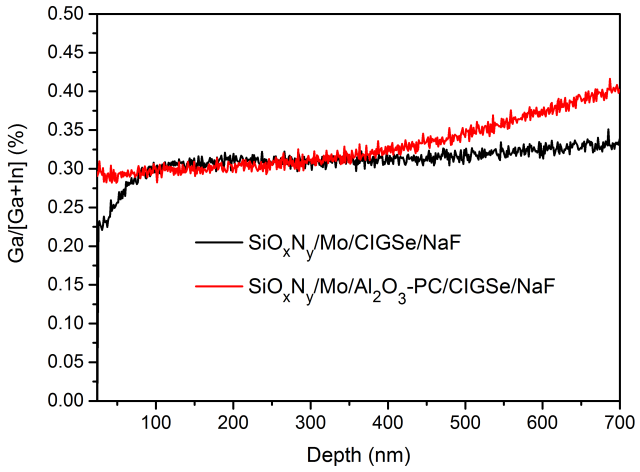

Figure 6.7: Glow Discharge Optical Emission Spectroscopy (GDOES) profile of a 650 nm CIGSe solar cells without a $SiNO_x$ barrier and with (red) and without (black) LRPC's.

and an efficient coupling of light into the CIGSe absorber. This can be confirmed from an enhanced light absorption in the point contact solar cells from the EQE measurements (Figure 6.6). To analyze the rise in V_{oc}, GDOES measurements were done (see Figure 6.7). Notably, a visible change in the Ga grading was found for the point contact devices from the reference solar cells. So, a part of V_{oc} improvement can be conferred to the difference in the Ga grading. Analyzing the dark J-V graphs lead to a prediction of increase in V_{oc} about 80 mV, due to a decade decrease in J_0 and improvement of the diode quality factor, A_1 (see Table 6.5).

In summary, point contacts at the back contact are advantageous to reduce the back interface recombination in ultra-thin CIGSe solar cells. Yet, a deficiency in J_{sc} about 5-7 mA/cm^2 is existing in comparison to the high-efficiency standard CIGSe devices. This could be overcome with the usage of a thicker Al_2O_3 layer and a modified point contact technology fabrication process or the usage of a high reflecting surface (Ag or Cu or Au) coated on top of the Al_2O_3 layer or highly efficient scattering structures at the back interface.

6.2 Summary

Thinner CIGSe solar cells with point contacts at the back interface (between Mo/CIGSe) were fabricated. The point contact configuration is found to be advantageous for the overall performance of the two thinner absorbers, 650 nm and 900 nm, considered in this

work. Simulation and experimental results show a correlation in the improvement of the Mo/CIGSe interface quality, marked by a significant V_{oc} gain of 0.1 V. Furthermore, Al_2O_3 could also act as a better reflector than Mo, and reduces the parasitic absorption at the back contact. Coverage area and opening radius were found to have a negligible impact on the solar cell performance due to the longer lifetime of the holes, which can be ascribed to the back surface field from Al_2O_3. Since the Al_2O_3 passivation layer can impede the diffusion of sodium from the glass substrate, Na should be supplied after the point contact formation or following the co-evaporation process of CIGSe absorbers.

7

Conclusion

The fact that high-efficiency CIGSe solar cells were achieved by an alkali fluoride post-deposition treatment, and the drop in efficiency when reducing the thickness of CIGSe devices led to the following questions. Is the V_{oc} limited by the CIGSe/CdS interface recombination in high-efficiency CIGSe solar cells and can therefore be boosted by interface engineering? How can the V_{oc} deficit caused by the back-contact recombination at Mo/CIGSe in thinner CIGSe absorbers be increased?

The goal of this work was to tackle these questions by using the concept of point contacts through a passivation layer (PaL), proceeding by the following steps: (i) performing simulations to predict the effect of point contacts on the efficiency and V_{oc} in CIGSe devices, (ii) considering theoretical results, choosing and depositing PaL using ALD, ILGAR or sputtering at the front or back interface of CIGSe absorbers, (iii) developing a suitable technique for patterning the PaL and (iv) application of point contacts into tangible devices and comparing them with standard devices.

To see the impact of the point contacts at CIGSe interfaces on device performance, 1D and 3D simulations were done with a large spectrum of CIGSe solar cells. The simulations were focused on point contact sizes, PaL properties and band alignment at the interface. Simulations predicted that an optimum device performance could be achieved if a PaL supplies a positive interface charge density greater than 10^{12} cm^{-2} for inducing a favourable band bending, leading to an n-type inversion at CIGSe/PaL and CIGSe/buffer interfaces. Also, the radius of the nano-contact openings should lie below 100 nm, which is equivalent to a coverage area of 96%. Independent of the interface quality of the CIGSe/buffer interface, a positive impact on cell performance was observed with the application of point contacts. The cliff like conduction band offset (CBO) at the CIGSe/buffer interface showed

a better improvement in conversion efficiency compared to a spiked CBO, and this offers more freedom in the choice of alternative buffer layers to CdS.

Considering the theoretical results, we tried to pattern a PaL using conventional lithographic techniques. The main hurdles we faced with patterning a PaL were the rough surface of the CIGSe and its low diffusion length. This forced us to develop a nanolithography technique using spherical monodispersed CdS nanoparticles (SNP's) for creating point contacts through PaL. The CdS SNP's were synthesised at the lowest temperature (80°C) reported to date. They were constituted of nano-crystallites (diameter $\approx$ 25-40 nm) with a hexagonal phase. Based on the concentration of the precursors and temperature of the reactants, it was possible to synthesis SNP's of radius 45 nm and 60 nm. These CdS SNP's acted as a sacrificial template for making point contacts. After assembling them onto the CIGSe surface by a dip-coating technique, a very thin layer of Al_2O_3 was deposited as the PaL. Al_2O_3 was chosen as the PaL based on the photoluminescence studies in this work that showed a strong increase in PL intensity after deposition of the PaL, and its defects passivation capability as reported in the literature. The point contacts were then obtained by removing the CdS SNP's using an HCl solution. This technique allowed us to create point contacts coverage on CIGSe between 11-40% as estimated by XPS. However, a higher coverage area of CdS SNP's on CIGSe was limited because of nanoparticle agglomeration. Moreover, the coverage of point contacts on CIGSe was uncontrollable due to the self-assembling property of CdS SNP's.

We found that the coverage area of PaL required for an optimum CIGSe device performance predicted by the theory (>96%) is higher than the experimentally (89%) obtained coverage area. However, from simulations, it is understood that a positive influence on efficiency and V_{oc} could be also seen with a coverage area of 89%. Therefore, we applied the point contact technology on CIGSe with CdS and Zn(O, S) buffer layers. The CdS buffer layer was found to be incompatible with a point contact application through Al_2O_3 PaL, because the NH_4OH present in the CBD solution also etched out the Al_2O_3, and hence the point contacts. Hence, we used dry deposition methods like sputtering and ALD for depositing buffer layers. ALD Zn(O,S) buffer layer with point contacts showed an improvement in efficiency, without a major change in V_{oc}. This could be due to an unoptimised ALD Zn(O,S) buffer layer deposition. The application of point contacts with a sputtered Zn(O, S) buffer layer improved the V_{oc} pointing to a reduced interface recombination. But

this didn't translate into an improvement of the device performance, most likely because Al_2O_3 was providing acceptor charges at the interface, contrary to the theoretical finding. Consequently, a spike was created at the CIGSe/Zn(O, S) interface and the effective band gap at the interface increased, enhancing the V_{oc} and impeding the current flow. This further correlated with photoluminescence measurements, where the V_{oc} was found to be proportional to the coverage area of Al_2O_3.

Point contacts were also applied to raise the V_{oc} in thinner CIGSe absorbers at the back interface, Mo/CIGSe. They were found to be advantageous for the overall performance of thin CIGSe absorbers. The interface quality was improved along with the optical properties of the stack configuration. The impact of the coverage area and the point contact radius on the efficiency was found to be insignificant: this is probably due to the back-surface field from Al_2O_3 which increases the lifetime of the holes. We also observed that the PaL blocks the diffusion of sodium from the soda-lime glass, which could affect the CIGSe material quality. Therefore, Na should be supplied after the point contact formation or as a CIGSe post-deposition treatment.

To conclude, this work gives an outlook on the prospect of point contacts at CIGSe interfaces, with backing from theoretical and experimental results, for achieving high-efficiency solar cells using an industrially viable point contact fabrication technique. Some clear improvements of cell parameters were found due to the application of point contacts.

However, the point contact technique was incompatible with the CdS buffer layer. Therefore, in future experiments, we suggest the usage of either a chemical vapour deposition of CdS or an efficient PaL, which is tolerant towards CBD deposition of CdS. Secondly, the impact of point contacts on record efficiency CIGSe solar cells is unknown, as the efficiencies of the solar cells used in this work were well below record efficiency CIGSe devices. Introduction of new PaLs [126, 127], with positive charges having a higher energetic level relative to the bands, will enhance the efficiency and give more flexibility on buffer layers. One could also try to manipulate the energetic levels of defects in Al_2O_3 by deposition methods like sputtering or controlling the deposition and annealing temperature. Also, modifications in the deposition technique of CdS SNP's on CIGSe surface are needed for achieving a higher coverage area of PaL as predicted by the simulations; eg: by using an electric field. An alternative way to attain the coverage area criteria is to cre-

ate point contacts by anodising PaL. Application of point contacts along with optimisation of the ALD and sputtering deposition of Zn(O,S) buffer layers could be another option for future experiments. Point contacts can also be used to increase the J_{sc} in CIGSe devices by limiting the buffer layer only to the point contact sites, thereby reducing the buffer layer thickness. Finally, at the back interface, it would be advantageous for the J_{sc} if a PaL of high reflectivity or a PaL followed by a reflective coating is applied.

To summarise, we have shown the improvement in certain CIGSs-based devices by using point contacts and we are optimistic that point contacts in CIGS solar cells have the capability to also raise the efficiency of the record efficiency CIGSe devices, if a PaL satisfies the theoretical conditions presented in this work. Also, the efficiency of thin CIGSe devices can be enhanced with an optical optimisation at the back contact along with point contacts, leading to efficient, yet thinner devices using less scarce elements like indium and requiring less time for production.

8

Appendices

8.1 Material and device characterisation techniques

8.1.1 Scanning Electron Microscope (SEM)

Scanning Electron Microscope (SEM) is used to examine specimen surfaces on a microscopic and nanoscopic scale by irradiating with a highly energetic electron beam. This will give rise to different electron-matter interactions and outcomes, as summarized in Fig. 8.1. These outcomes or the generated signals can be utilized to yield information about the morphology, topography and elemental analysis of the specimen. The signals are generated from an interaction volume, which takes a shape of a tear drop to a semi-circle, depending on the incident energy beam, atomic number and density of the atoms present in the specimen.

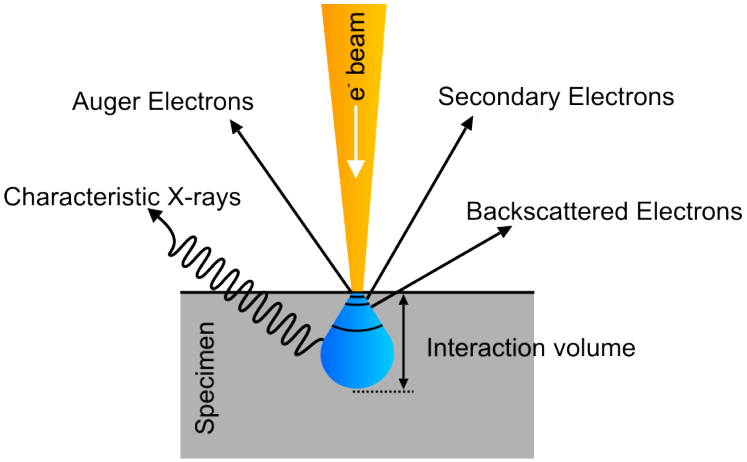

Figure 8.1: Schematic diagram illustrating the electron-matter interactions during SEM imaging.

Most of the incident energy is dispersed as heat; the rest of it is elastically and inelastically scattered. The inelastically scattered secondary electrons, emitted from the valence band of the atoms from the specimen, have low energy (50 eV or less). Therefore, only electrons from the surface are able to escape out of the specimen and can deliver the information about the topography of the specimen. To the contrary, the back scattered or reflected electrons have energy ranging from 50 eV to the incident electron energy and carry information from relatively deep in the specimen compared to secondary electrons; this also depends on the atomic number of the constituent atoms present in the specimen. Hence, they are used to investigate specimen's composition.

In this work, to study the surface morphology and determine the size of the CdS nanoparticles deposited on CIGSe or molybdenum surfaces, and to check the point contacts formation, a scanning electron microscope (SEM) (Leo 1530) operated at an accelerating voltage between 3 and 10 kV is employed.

8.1.2 X-ray Diffraction (XRD)

X-ray diffraction (XRD) is a standard analytical technique for determining the structure of crystalline materials based on their diffraction pattern. XRD occurs when X-rays, of wavelength, λ, comparable to the lattice parameters of a crystal, interact with periodically arranged atoms in a crystal structure. The reflected rays from each plane, from intervals of $2d \cdot cos\Theta$, will produce a constructive interference or a diffraction peak. This condition was formulated by Bragg in 1912 [128]: here Θ is the angle of incidence of the X-rays, *d* is the shortest distance between successive lattice planes, and *n* is the order of the diffraction peak.

$$n\,\lambda = 2d\,sin\Theta \tag{8.1}$$

Each diffraction peak corresponds to a unique phase, and its shape, position and intensity can give information about the structure of the material. To find the XRD pattern of a family of planes with spacing $d_{h,k,l}$ (where *hkl* are the Miller indices of a plane), Θ is varied for a range of angles to satisfy Bragg's angle, $\Theta_{h,k,l}$.

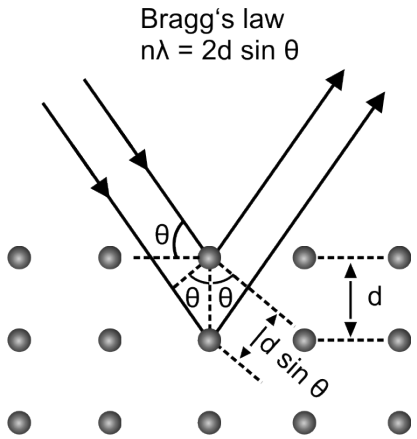

Figure 8.2: Schematic illustration of Bragg's condition for constructive interference from a set of lattice planes.

In this work, X-ray diffraction is used to identify the phase and crystallinity of the CdS NP's nanoparticles. A Bruker D8 diffractometer in grazing incidence mode is used to perform XRD measurements. The Cu-K_α X-rays, having a characteristic wavelength of $\lambda = 1.5406$ Å, are generated at a Cu anode for an acceleration voltage of 40 kV and filament current of 30 mA. In the grazing incidence mode, the detector angle is varied from 10-80°, keeping the X-ray source fixed.

8.1.3 X-ray Photoelectron Spectroscopy (XPS)

X-ray photoelectron spectroscopy (XPS), also known as Electron Spectroscopy for Chemical Analysis (ESCA), is an analytic technique used to examine the surface chemical composition of samples. The basis of XPS is the photoelectric effect. A schematic illustration of different photo-ionisation processes that occur during an XPS measurement is shown in Fig.8.3. Since XPS can reveal information about the elemental composition at the surfaces, in this work, it is mainly used as a tool to determine point contacts formation and surface area coverage of the passivation layer, Al_2O_3. A brief overview of the XPS technique will be presented in this section; further, in-depth information can be found in [129].

In an XPS measurement, the distinguishable parameter is the electron binding energy, BE — the amount of energy that is required to pull out an electron from a core atomic orbital. Each BE is associated with a core atomic orbital, which is specific to an element and depends on the chemical environment of the probed atom. For measuring the BE, a

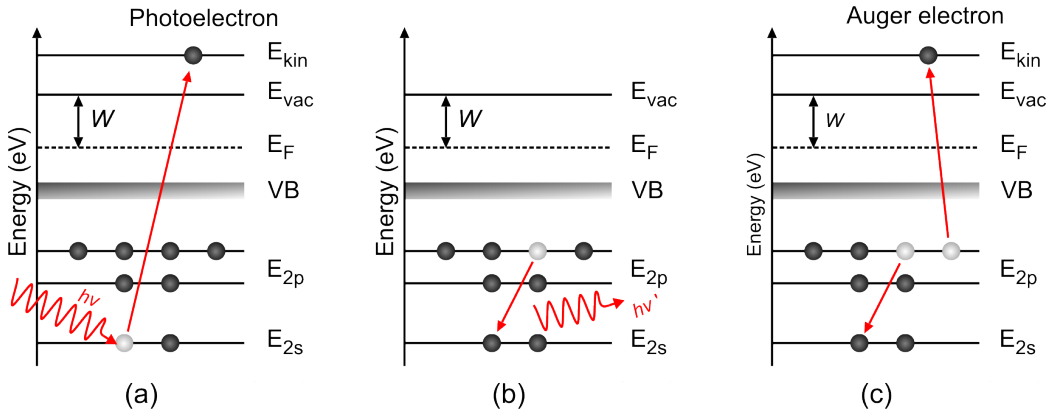

Figure 8.3: Schematic illustration of different XPS processes: (a) incident x-ray of an energy, $h\nu$, creating a photoelectron, (b) a photon of an energy, $h\nu'$, is emitted by the relaxation of an outer electron into the hole, (c) Auger electron emission initiated by the secondary x-ray of energy $h\nu'$, created in the process (b).

known energy source of X-ray photons is used to excite electrons: commonly, Mg K_α ($h\nu$ = 1253.6 eV) and Al K_α ($h\nu$ = 1486.6 eV) are employed in lab based experiments. Therefore, the emitted photoelectrons will have kinetic energies, E_{kin}, in the range of $\approx$ 0 - 1250 eV or 0 - 1480 eV, which are counted with an electron spectrometer. The BE of an electon from an atomic orbital is calculated using the Eq. 8.2, where ϕ_B, is the work function of the spectrometer.

$$E_{kin} = E_{h\nu} - E_B - \phi_B \tag{8.2}$$

The intensity of each isolated peak in XPS is proportional to the amount of atoms present on the sample near-surface region. Quantitatively an XPS measurement is analysed by subtracting the background using an appropriate function (in most cases a Shirley background [130]), followed by fitting the curve using a Voigt profile, which is a convolution of Gaussian and Lorentzian distribution. Care has to be taken in such an analysis, because the error can become quite large ($\approx$ 52%) [131] as other factors also contribute to the intensity of an XPS peak. A widely accepted method to minimise these errors is by comparing peaks having similar kinetic energies as they mainly depend on it. The intensity of an XPS peak is generally described as follows [132]:

$$I = C \cdot n \cdot I_0 \cdot \frac{\partial \sigma}{\partial \Omega}(h\nu) \cdot T(E_{kin}) \cdot \lambda(E_{kin}) \tag{8.3}$$

where C is the concentration of an element in the sample, n refers to the number of XPS scans, I_0 is the intensity of the X-ray beam, $\partial\sigma/\partial\Omega$ refers to the cross-section for the partial subshell photoionization, which describes the probability of absorption of a photon by an electron in a certain shell of an atom. $T(E_{kin})$ is the transmission function of the spectrometer, which defines a spectrometer sensitivity to photoelectrons of different kinetic energies. And $\lambda(E_{kin})$ stands for the mean free path of a free electron.

The XPS measurements in this work were performed using a Mg K_α (1253.6 eV) laboratory radiation source at the CISSY station (CIS + Synchrotron). To minimise the samples surface contamination, the measurements were performed at a base pressure of 5×10^{-9} mbar. The angle between the X-ray beam and the spectrometer axis is aligned at 54.7° [133] — the magic angle at which the angular asymmetry parameter is a constant. The CISSY's spectrometer has a $T(E_{kin})$ = 840.2335 $\cdot(E_{kin})^{-0.9748}$ [134]. The photoelectrons are detected using a hemispherical CLAM 4 electron analyser from Thermo VG Scientific.

8.1.4 Glow Discharge-Optical Emission Spectroscopy

The working principle of GDOES is based on sputtering a sample surface layer by layer using a plasma, and identifying the removed atoms by their characteristic optical emission, resulting from their excitation within the sputtering plasma. Therefore, an experimental setup of a GDOES is separated into two compartments: a glow discharge source for sputtering and an optical detector. The sample under characterization also acts as cathode. A high DC voltage, supplied between the anode and cathode, results in accelerating the ions in the Ar plasma, leading to sputtering of material from the sample surface. Then, the atoms that are removed migrate into the plasma, where they ionize, excite and emit characteristic optical emission, which is focused onto a concave grating and detected using a CCD array. An accurate analysis of the chemical composition of the sample from the intensity of emitted light depends on a suitable calibration of measurement [135].

In this work GDOES is used for determining the Ga-depth profile within the CIGSe layer.

The measurement is performed with a Spectruma GDA 650 spectrometer using a pulsed RF Argon plasma. The anode has a diameter of 2.5 mm. The process pressure of discharge gas pressure was at 3.5 hPa and the applied voltage at 500 V.

8.1.5 J–V measurements

The J–V measurements presented in this work were performed at 25 °C by a four-probe point measurement system (Keithley source measurement unit—max. 3 A and 105 V). The AAA Wacom dual source solar simulator delivers the AM 1.5 spectrum with an illumination intensity of 100 mW/cm^2 (spectral match of $\pm 10\%$). The uncertainity in the homogeneity of illumination area is limited to $\pm 2\%$.

8.1.6 External Quantum Efficiency (EQE)

The EQE measurements were performed at room temperature, using a halogen lamp as light source. A Czerny Turner monochromator was used to narrow the wavelength bandwidth to 10 nm. The lock in technique (SR830) was used to record the J_{sc} amplified by a Stanford Research 560 amplifier. The EQE measurements were calibrated using a Si and GaAs solar cell.

8.1.7 Time-resolved photoluminescence (TRPL)

Time-resolved photoluminescence spectroscopy (TRPL) is an extension of photoluminescence spectroscopy. In addition to the spectral information, TRPL gives the information on the temporal evolution of the emission from a sample. A short light pulse is used to excite the sample, and the emission is recorded as a function of time using a fast detector. In this work, TRPL is employed to understand the interface quality after the point contacts fabrication based on the measured emission time, as it is a direct measure of the material quality. TRPL measurements in this work were performed using a custom made setup which uses a 660 nm pulsed laser source and time-correlated single photon counting with a InGaAs photomultiplier. The instrument has a time resolution less than 250 ps, and an excitation spot size of $\approx$ 40 μm in diameter was used for measurements.

8.2 Nanolithography using polystyrene nanoparticles

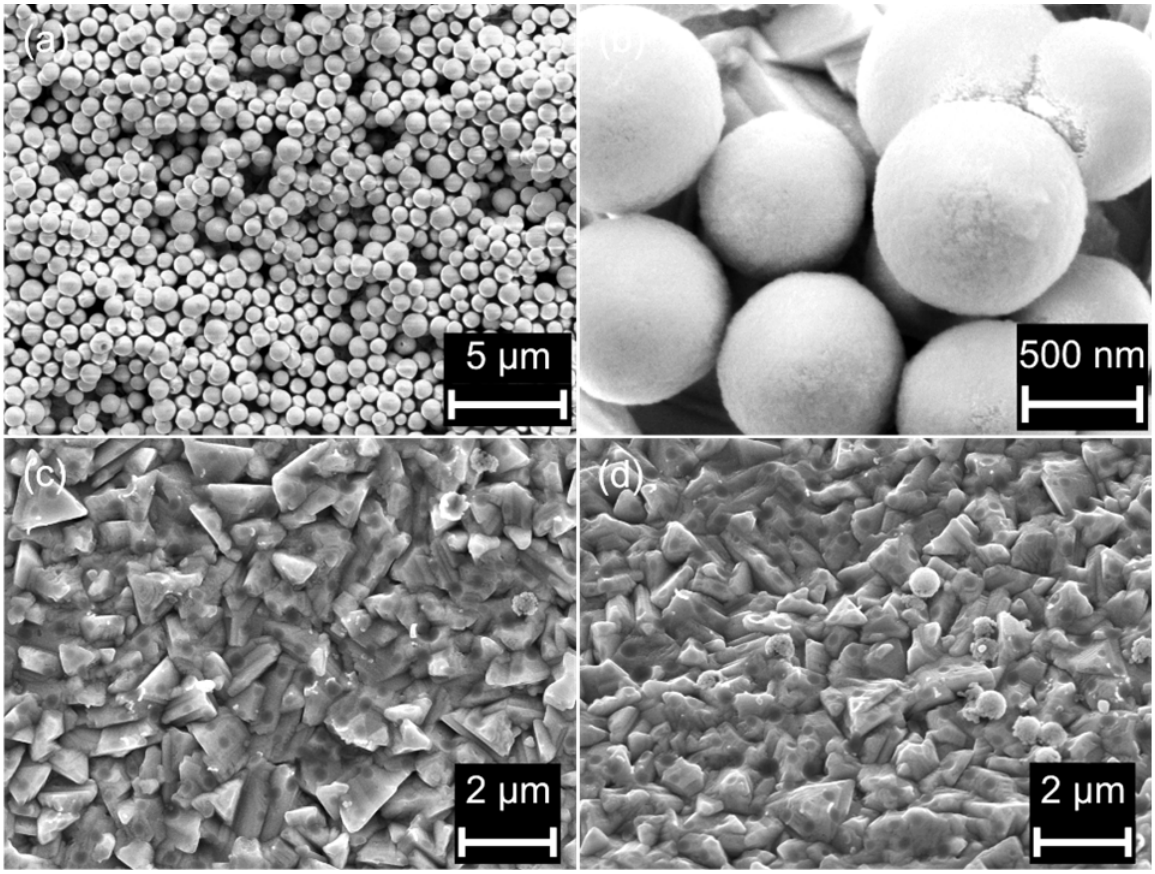

Figure 8.4: SEM images showing the different stages of point contacts fabrication using nanosphere-lithography. Polystyrene nanoparticles (PS NP's) of radius 900 nm are arranged in a closed array onto a CIGSe substrate [136]. Then, 10 nm of Al_2O_3 was deposited using thermal evaporation, followed by removing the PS NP's in an ultrasonic bath. (a) and (b) Array of PS NP's on CIGSe for different magnifications. (c) and (d) Point contacts formation after the removal of PS NP's.

8.3 Supplementary Information

8.3.1 Photoluminescence

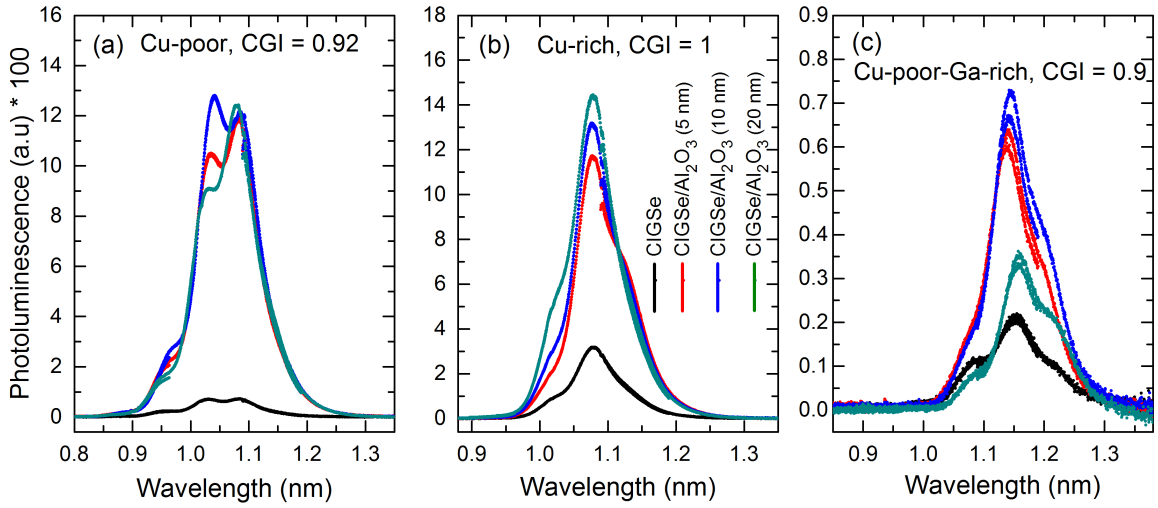

Figure 8.5: Photoluminescence spectra before (reference CIGSe–black) and after the deposition of Al_2O_3 on three different stoichiometric CIGSe substrates: (a) Cu/[In+Ga]=0.92, (b) Cu/[In+Ga]= 1 and (c) Cu/[In+Ga]=0.9.

8.3.2 Time-resolved photoluminescence

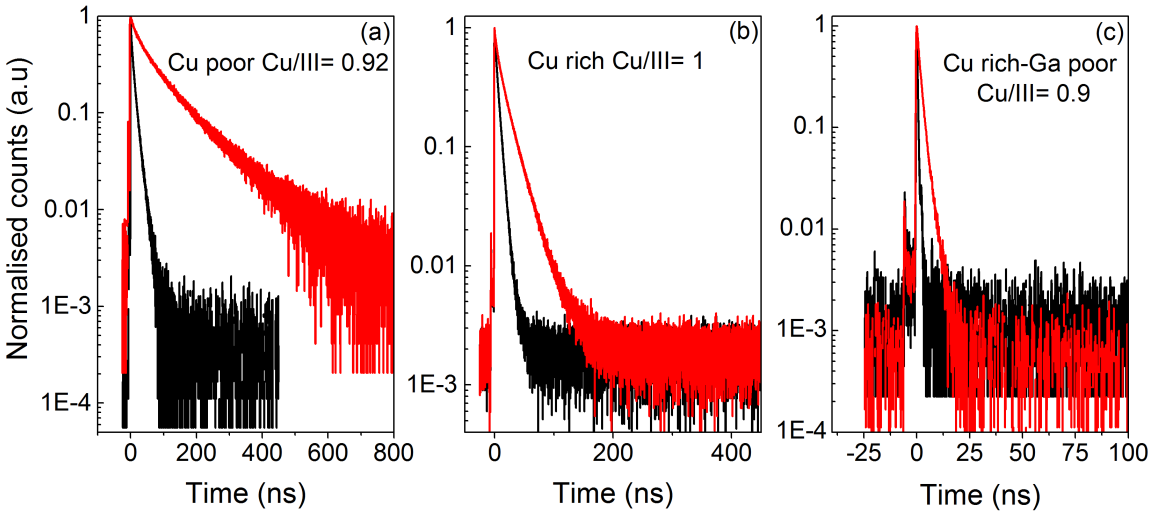

Figure 8.6: Comparison of PL spectra before (reference CIGSe–black) and after the deposition of thin layers of Al_2O_3 of thickness 5, 10 and 20 nm on three different stoichiometric CIGSe substrates: (a) Cu/[In+Ga]=0.92, (b) Cu/[In+Ga]= 1 and (c) Cu/[In+Ga]=0.9.

Table 8.1: Summary of the TRPL data obtained for samples shown in figure 8.6 in the same order; a bi-exponential curve is used to fit the TRPL decay.

Sample	τ_1 (ns)	τ_2 (ns)	A_1	A_2	Average carrier lifetime $\frac{A_1 \cdot \tau_1^2 + A_2 \cdot \tau_2^2}{A_1 \cdot \tau_1 + A_2 \cdot \tau_2}$ (ns)
CIGSe (CGI=0.92)	2.37	11.92	6308.91	10715.92	10.9
CIGSe/Al_2O_3 (CGI=0.92)	21.86	112.05	1898.3	2815	101.56
CIGSe (CGI=1)	1.96	6.72	5458.5	17545.2	6.33
CIGSe/Al_2O_3 (CGI=1)	5.29	22.6	7961.94	13099.06	20.43
CIGSe (CGI=0.9)	3.08	0.35	76.5	5695.8	0.64
CIGSe/Al_2O_3(CGI=0.9)	1.23	2.67	11950	6775.11	2.03

8.3.3 J-V-T analysis

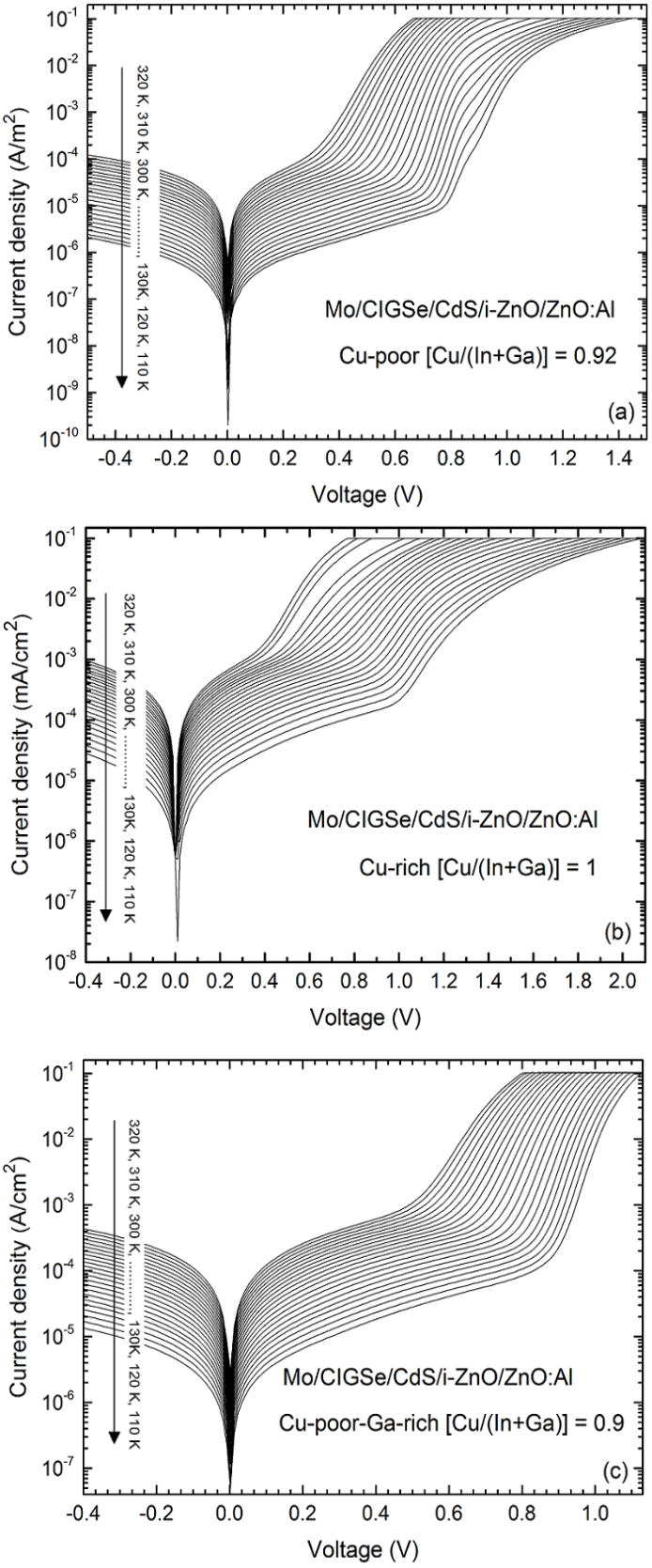

Figure 8.7: J-V curves measured for CIGSe solar cells having different stoichiometric ratios in dark, recorded at temperatures ranging from 300K to 120K (ΔT=10 K):(a) Cu/[In+Ga]=0.92, (b) Cu/[In+Ga]= 1 and (c)Cu/[In+Ga]=0.9.

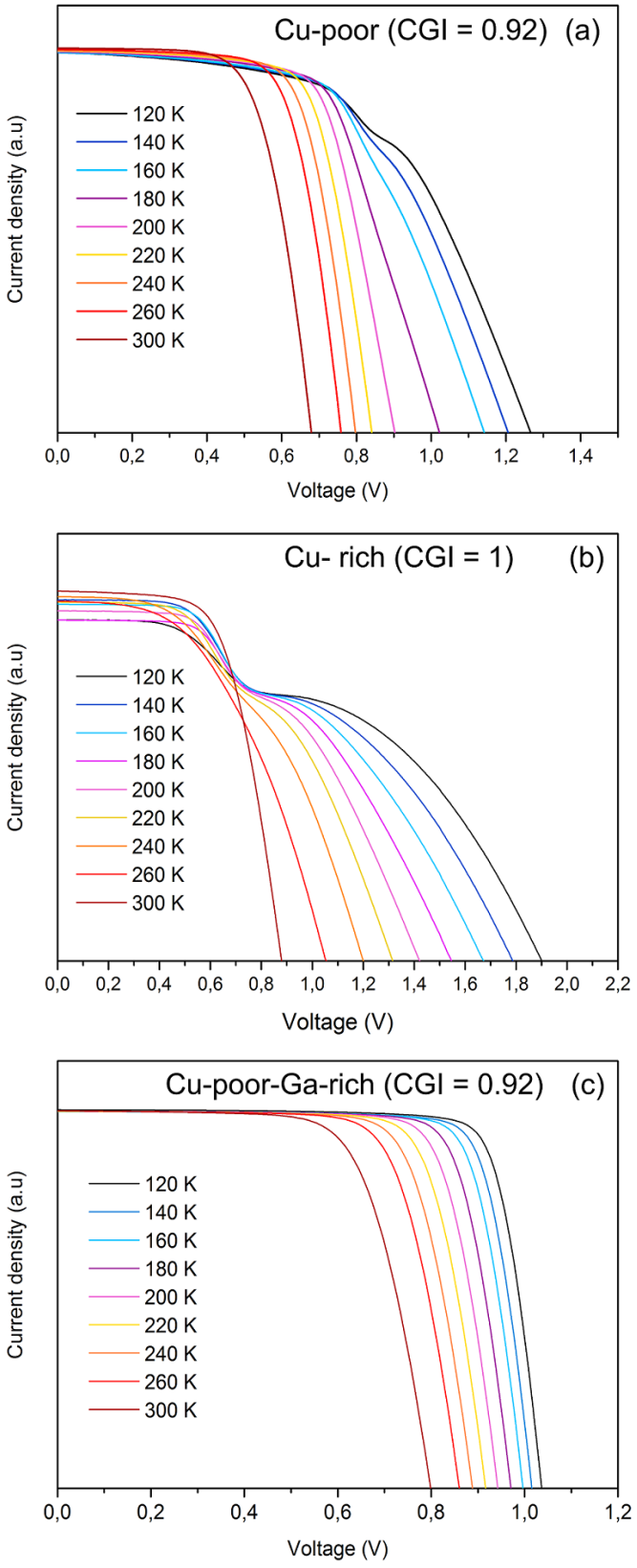

Figure 8.8: J-V curves measured for CIGSe solar cells having different stoichiometric ratios under AM 1.5 spectrum, recorded at temperatures ranging from 300K to 120K (ΔT=10 K):(a) Cu/[In+Ga]=0.92, (b) Cu/[In+Ga]= 1 and (c)Cu/[In+Ga]=0.9.

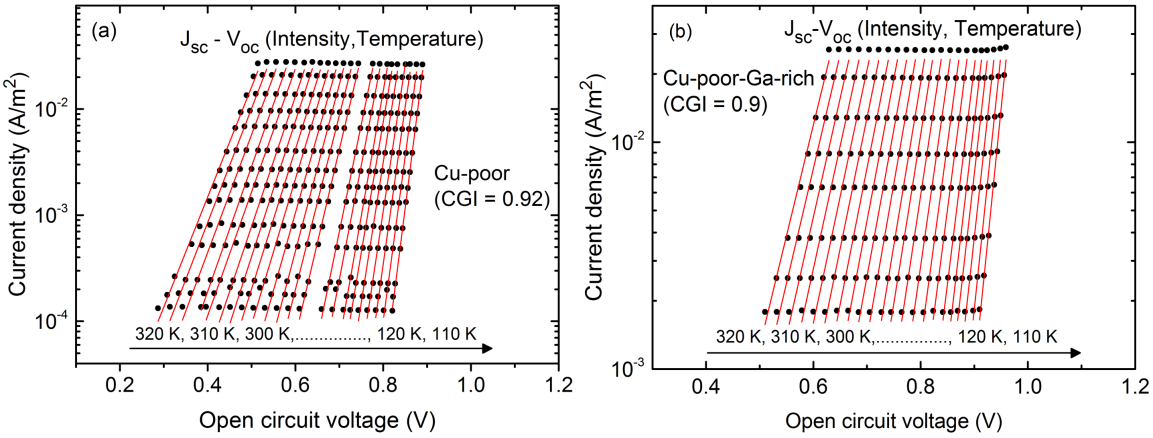

Figure 8.9: $J_{sc} - V_{oc}$ as a function of intensity for temperatures ranging from 300 K to 110 K (ΔT=10 K). The red line represents the linear fitting of $J_{sc} - V_{oc}$ values; (a) Cu-poor (Cu/[In+Ga]=0.92) absorber, (b) Cu-poor–Ga-rich absorber (Cu/[In+Ga]=0.9. The Cu-rich absorber is not shown here as it is measured for only two intensities.

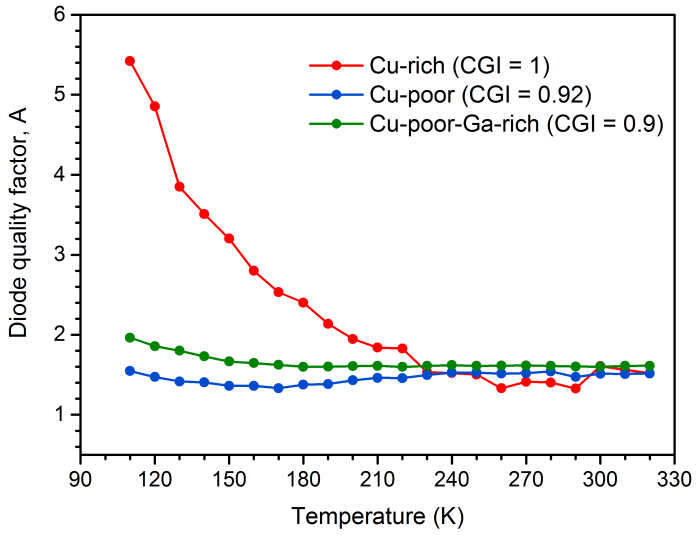

Figure 8.10: Ideality factor of CIGSe solar cells having different stoichiometric ratios (Cu/[In+Ga]= 1, Cu/[In+Ga]=0.92, and Cu/[In+Ga]=0.9), as a function of temperature ranging from 320 to 110K (ΔT=10 K), calculated from J_{sc} - V_{oc} plots.

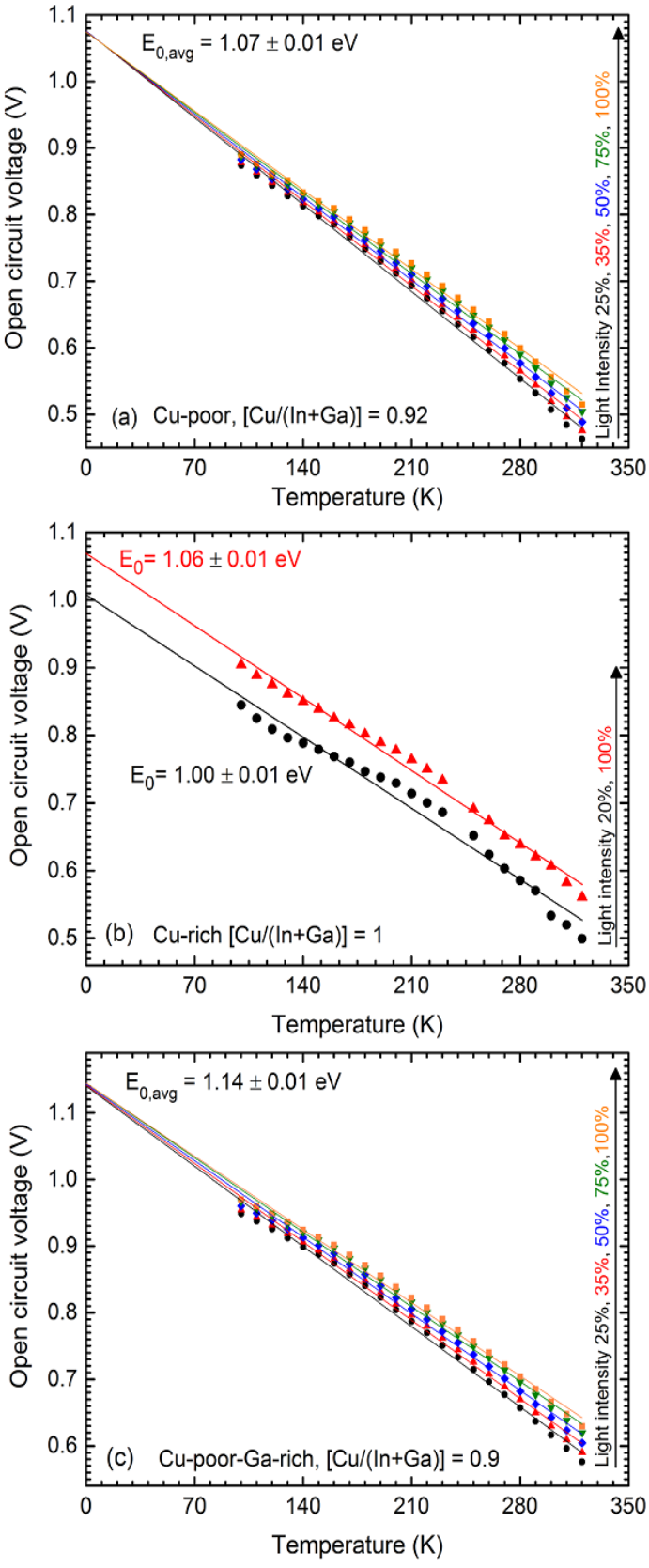

Figure 8.11: V_{oc} as a function of temperature at different intensities. Black lines show the linear extrapolation of the data points to 0 K to estimate the activation energy, AE: (a) Cu/[In+Ga]=0.92, (b) Cu/[In+Ga]= 1 and (c)Cu/[In+Ga]=0.9.

Bibliography

[1] P. Jackson, R. Wuerz, D. Hariskos, E. Lotter, W. Witte, and M. Powalla. Effects of heavy alkali elements in Cu(In,Ga)Se_2 solar cells with efficiencies up to 22.6%. *physica status solidi (RRL) - Rapid Research Letters*, 10(8):583–586, 2016.

[2] P. Reinhard, B. Bissig, F. Pianezzi, E. Avancini, H. Hagendorfer, D. Keller, P. Fuchs, M. Döbeli, C. Vigo, P. Crivelli, S. Nishiwaki, S. Buecheler, and A. N. Tiwari. Features of KF and NaF Postdeposition Treatments of Cu(In,Ga)Se_2 Absorbers for High Efficiency Thin Film Solar Cells. *Chemistry of Materials*, 27(16):5755–5764, 2015.

[3] U.S. Global Change Research Program National Climate Assessment. Our changing climate. *https://nca2014.globalchange.gov/report/our-changing-climate/extreme-weather*, 2014.

[4] United Nations Framework Convention on Climate. The paris agreement - main page. *http://unfccc.int/paris- agreement/items/9485.php*, 2017.

[5] International Renewable Energy Agency. Untapped potential for climate action: Renewable energy in nationally determined contributions. *https://www.irena.org/publications/2017/Nov/Untapped-potential-for-climate-action-NDC*, 2017.

[6] U.S Energy Information Administration. International energy outlook 2017. *https://www.eia.gov/outlooks/ieo/*, 2017.

[7] World Energy Council. World energy resources full report - 2016. *https://www.worldenergy.org/publications/2016/world-energy-resources-2016/*, 2016.

[8] International Renewable Energy Agency. Renewable capacity statistics 2018. *http://www.irena.org/publications/2018/Mar/Renewable-Capacity-Statistics-2018*, 2018.

[9] A. Chirila, P. Reinhard, F. Pianezzi, P. Bloesch, A. R. Uhl, C. Fella, L. Kranz, D. Keller, C. Gretener, H. Hagendorfer, D. Jaeger, R. Erni, S. Nishiwaki, S. Buecheler, and A. N. Tiwari. Potassium-induced surface modification of Cu(In,Ga)Se_2 thin films for high-efficiency solar cells. *Nature Materials*, 12:1107–1111, 2013.

[10] R. Kamada, T. Yagioka, S. Adachi, A. Handa, K. F. Tai, T. Kato, and H. Sugimoto. New world record Cu(In, Ga)(Se, $S)_2$ thin film solar cell efficiency beyond 22%. In *2016 IEEE 43rd Photovoltaic Specialists Conference (PVSC)*, pages 1287–1291, 2016.

[11] R. Scheer and H. W. Schock. Chalcogenide photovoltaics: Physics, technologies, and thin film devices. *John Wiley & Sons*, 2011.

[12] Zhao Jianhua, Wang Aihua, and Green Martin A. 24.5% efficiency silicon pert cells on mcz substrates and 24.7% efficiency perl cells on fz substrates. *Progress in Photovoltaics: Research and Applications*, 7, 2000.

[13] ISE Fraunhofer Institute for Solar Energy Systems. Photovoltaics report. *https://www.ise.fraunhofer.de/content/dam/ise/de/documents/publications/studies/Photovoltaics-Report.pdf*, 2017.

[14] P. Pistor, D. Greiner, C. A. Kaufmann, S. Brunken, M. Gorgoi, A. Steigert, W. Calvet, I. Lauermann, R. Klenk, T. Unold, and M.-C. Lux-Steiner. Experimental indication for band gap widening of chalcopyrite solar cell absorbers after potassium fluoride treatment. *Applied Physics Letters*, 105(6):063901, 2014.

[15] H. Elanzeery, F. Babbe, M. Melchiorre, A. Zelenina, and S. Potassium Fluoride Ex-Situ Treatment on Both Cu-Rich and Cu-Poor $CuInSe_2$ Thin Film Solar Cells. *IEEE Journal of Photovoltaics*, 7(2):684–689, 2017.

[16] T. Kirchartz and U. Rau. Introduction to thin-film photovoltaics. *Wiley-VCH Verlag GmbH & Co. KGaA*, pages 1–32, 2011.

[17] J.L. Shay and J.H. Wernick. *Chapter 2 - The Chalcopyrite structure and crystal growth*, volume 7 of *International Series in the Science of the Solid State*. Pergamon, 1975.

[18] T. Maeda and T. Wada. Characteristics of chemical bond and vacancy formation in chalcopyrite-type $CuInSe_2$ and related compounds. *physica status solidi (c)*, 6(5): 1312–1316, 2009.

[19] S. C. Abrahams and J. L. Bernstein. Piezoelectric nonlinear optic $CuGaSe_2$ and $CdGeAs_2$: Crystal structure, chalcopyrite microhardness, and sublattice distortion. *The Journal of Chemical Physics*, 61(3):1140–1146, 1974.

[20] D. Abou-Ras, R. Caballero, C. A. Kaufmann, M. Nichterwitz, K. Sakurai, S. Schorr, T. Unold, and H. W. Schock. Impact of the Ga concentration on the microstructure of $CuIn_{1-x}Ga_xSe_2$. *physica status solidi (RRL), Rapid Research Letters*, 2(3):135–137, 2008.

[21] B. Ümsür. Surface Engineering of $Cu(In,Ga)Se_2$ by KF and CdS — a Study by High-Energy Photoemission Spectroscopy. *PhD Dissertation*, 2017.

[22] U. Rau and H.W. Schock. llc–4 — $CuInGaSe_2$ thin-film solar cells. *Elsevier Science*, pages 303 – 349, 2005.

[23] C. Morioka, K. Shimazaki, S. Kawakita, M. Imaizumi, H. Yamaguchi, T. Takamoto, S. Sato, T. Ohshima, Y. Nakamura, K. Hirako, and M. Takahashi. First flight demonstration of film-laminated InGaP/GaAs and CIGS thin-film solar cells by JAXA's small satellite in LEO. *Progress in Photovoltaics: Research and Applications*, 19(7):825–833, 2011.

[24] D.A. Keszler and J.F. Wager. Novel materials development for polycrystalline thin-film solar cells. *NREL Report*, 2008.

[25] N. Nicoara, Th. Lepetit, L. Arzel, S. Harel, N. Barreau, and S. Sadewasser. Effect of the KF post-deposition treatment on grain boundary properties in Cu(In, Ga)Se_2 thin films. *Scientific Reports*, 7(41361), 2017.

[26] C.A. Kaufmann, A. Neisser, R. Klenk, and R. Scheer. Transfer of Cu(In, Ga)Se_2 thin film solar cells to flexible substrates using an in situ process control. *Thin Solid Films*, 480:515 – 519, 2005.

[27] A. M. Gabor, J. R. Tuttle, D. S. Albin, M. A. Contreras, R. Noufi, and A. M. Hermann. High efficiency $CuIn_xGa_{1-x}Se_2$ solar cells made from $(In_2,Ga_{1-x})_2Se_3$ precursor films. *Applied Physics Letters*, 65(2):198–200, 1994.

[28] C.A. Kaufmann, R. Caballero, T. Unold, R. Hesse, R. Klenk, S. Schorr, M. Nichterwitz, and H.-W. Schock. Depth profiling of Cu(In,Ga)Se_2 thin films grown at low temperatures. *Solar Energy Materials and Solar Cells*, 93(6):859 – 863, 2009. 17th International Photovoltaic Science and Engineering Conference.

[29] D. Abou-Ras, G. Kostorz, A. Romeo, D. Rudmann, and A.N. Tiwari. Structural and chemical investigations of CBD- and PVD-CdS buffer layers and interfaces in Cu(In,Ga)Se_2-based thin film solar cells. *Thin Solid Films*, 480:118 – 123, 2005.

[30] D. Strauch. CdS: lattice parameters. *Springer*, pages 99–102, 2012.

[31] R.J. Nelmes and M.I. McMahon. *Chapter 3 Structural Transitions in the Group IV, III-V, and II-VI Semiconductors under Pressure*, volume 54. Elsevier, 1998.

[32] D. Liao and A. Rockett. Cu depletion at the $CuInSe_2$ surface. *Applied Physics Letters*, 82(17):2829–2831, 2003.

[33] T. Minemoto, T. Matsui, H. Takakura, Y. Hamakawa, T. Negami, Y. Hashimoto, T. Uenoyama, and M. Kitagawa. Theoretical analysis of the effect of conduction band offset of window/CIS layers on performance of CIS solar cells using device simulation. *Solar Energy Materials and Solar Cells*, 67(1):83 – 88, 2001.

[34] C. Persson, Y. J. Zhao, S. Lany, and A. Zunger. n-type doping of $CuInSe_2$ and $CuGaSe_2$. *Phys. Rev. B*, 72:035211, 2005.

[35] S. Siebentritt. Alternative buffers for chalcopyrite solar cells. *Solar Energy*, 77(6): 767 – 775, 2004.

[36] S. Ishizuka, K. Sakurai, A. Yamada, K. Matsubara, P. Fons, K. Iwata, S. Nakamura, Y. Kimura, T. Baba, H. Nakanishi, T. Kojima, and S. Niki. Fabrication of wide-gap Cu($In_{1-x}Ga_x$)Se_2 thin film solar cells: a study on the correlation of cell performance with highly resistive i-ZnO layer thickness. *Solar Energy Materials and Solar Cells*, 87(1):541 – 548, 2005.

[37] R. Klenk. Characterisation and modelling of chalcopyrite solar cells. *Thin Solid Films*, 387(1):135 – 140, 2001. Proceeedings of Symposium N on Thin Film Photovoltaicmaterials of the E-MRS Spring Conference.

[38] I. Hengel, A. Neisser, R. Klenk, and M.Ch. Lux-Steiner. Current transport in $CuInS_2$:Ga/CdS/ZnO solar cells. *Thin Solid Films*, 361(Supplement C):458 – 462, 2000.

[39] A. Niemegeers, M. Burgelman, and A. De Vos. On the CdS/$CuInSe_2$ conduction band discontinuity. *Applied Physics Letters*, 67(6):843–845, 1995.

[40] W. Shockley and W. T. Read. Statistics of the recombination of holes and electrons. *Phys. Rev.*, 87:835–842, 1952.

[41] I. Hengel. *Ladungsträgertransport und Rekombinationsmechanismen in Chalkopyrit- Dünnschichtsolarzellen.* PhD thesis, Freie Universität Berlin, 2000.

[42] Jenny Nelson. *The Physics of Solar Cells*. Imperial college press-world scientific publishing co., 2011.

[43] M. Turcu and U. Rau. Fermi level pinning at CdS/Cu(In,Ga)$(Se,S)_2$ interfaces: effect of chalcopyrite alloy composition. *Journal of Physics and Chemistry of Solids*, 64 (9):1591 – 1595, 2003. 13th International Conference on Ternary and Multinary Compounds.

[44] R. Scheer. Activation energy of heterojunction diode currents in the limit of interface recombination. *Journal of Applied Physics*, 105(10):104505, 2009.

[45] U.Rau. Electronic loss mechanisms in chalcopyrite based heterojunction solar cells. *Thin Solid Films*, 361(Supplement C):298 – 302, 2000.

[46] V. Nadenau, U. Rau, A. Jasenek, and H. W. Schock. Electronic properties of $CuGaSe_2$-based heterojunction solar cells. Part I. Transport analysis. *Journal of Applied Physics*, 87(1):584–593, 2000.

[47] P. Reinhard, B. Bissig, F. Pianezzi, H. Hagendorfer, G. Sozzi, R. Menozzi, C. Gretener, S. Nishiwaki, S. Buecheler, and A. N. Tiwari. Alkali-templated surface nanopatterning of chalcogenide thin films: A novel approach toward solar cells with enhanced efficiency. *Nano Letters*, 15(5):3334–3340, 2015.

[48] Y. Fu, N. Allsop, S. E. Gledhill, T. Köhler, M. Krüger, R. Saez-Araoz, U. Blöck, M. Ch. Lux-Steiner, and C. H. Fischer. ZnS Nanodot Film as Defect Passivation Layer for Cu(In,Ga)$(S,Se)_2$ Thin-Film Solar Cells Deposited by Spray-ILGAR (Ion-Layer Gas Reaction). *Advanced Energy Materials*, 1(4), 2011.

[49] N. Allsop, R. Nürnberg, M. Ch. Lux-Steiner, and Th. Schedel-Niedrig. Three-dimensional simulations of a thin film heterojunction solar cell with a point contact/defect passivation structure at the heterointerface. *Applied Physics Letters*, 95 (12):122108, 2009.

[50] G. Brown, V. Faifer, A. Pudov, S. Anikeev, E. Bykov, M. Contreras, and J. Wu. Determination of the minority carrier diffusion length in compositionally graded Cu(In,Ga)Se_2 solar cells using electron beam induced current. *Applied Physics Letters*, 96(2):022104, 2010.

[51] R. Kniese, M. Powalla, and U. Rau. Evaluation of electron beam induced current profiles of Cu(In,Ga)Se_2 solar cells with different Ga-contents. *Thin Solid Films*, 517(7):2357 – 2359, 2009. Thin Film Chalogenide Photovoltaic Materials (EMRS, Symposium L).

[52] B. Vermang, J. T. Wätjen, V. Fjällström, F. Rostvall, M. Edoff, R. Kotipalli, F. Henry, and D. Flandre. Employing Si solar cell technology to increase efficiency of ultra-thin Cu(In,Ga)Se_2 solar cells. *Progress in Photovoltaics: Research and Applications*, 22 (10), 2014.

[53] E. Jarzembowski, B. Fuhrmann, H. Leipner, W. Fränzel, and R. Scheer. Ultrathin Cu(In,Ga)Se_2 solar cells with point-like back contact in experiment and simulation. *Thin Solid Films*, 633:61 – 65, 2017. E-MRS 2016 Spring Meeting, Symposium V, Thin-Film Chalcogenide Photovoltaic Materials.

[54] P. Casper, R. Hünig, G. Gomard, O. Kiowski, C. Reitz, U. Lemmer, M. Powalla, and M. Hetterich. Optoelectrical improvement of ultra-thin Cu(In,Ga)Se_2 solar cells through microstructured MgF_2 and Al_2O_3 back contact passivation layer. *physica status solidi (RRL), Rapid Research Letters*, 10(5):376–380, 2016.

[55] H.-W. Schock, T. Walter, and R. Herberholz. Distribution of defects in polycrytalline chalcopyrite thin films. *Solid State Phenomena,*, 51:309–316, 5 1996.

[56] T. Walter, R. Menner, Ch. Köble, and H.W. Schock. Characterization and junction performance of highly efficient ZnO/CdS/CuInS_2 thin film solar cells. *Proceedings of the 12th European Photovoltaic Energy Conference*, 1994.

[57] F. Engelhardt, M. Schmidt, Th. Meyer, O. Seifert, J. Parisi, and U. Rau. Metastable electrical transport in Cu(In,Ga)Se_2 thin films and ZnO/CdS/Cu(In,Ga)Se_2 heterostructures. *Physics Letters A*, 245(5):489 – 493, 1998.

[58] E. Handick, P. Reinhard, J. H. Alsmeier, L. Köhler, F. Pianezzi, S. Krause, M. Gorgoi, E. Ikenaga, N. Koch, R. G. Wilks, S. Buecheler, A. N. Tiwari, and M. Bär. Potassium Post-deposition Treatment-Induced Band Gap Widening at Cu(In,Ga)Se_2 Surfaces – Reason for Performance Leap? *ACS Applied Materials & Interfaces*, 7(49):27414–27420, 2015.

[59] E. Handick, P. Reinhard, R. G. Wilks, F. Pianezzi, T. Kunze, D. Kreikemeyer-Lorenzo, L. Weinhardt, M. Blum, W. Yang, M. Gorgoi, E. Ikenaga, D. Gerlach, S. Ueda, Y. Yamashita, T. Chikyow, C. Heske, S. Buecheler, A. N. Tiwari, and M. Bär. Formation of a K–In–Se Surface Species by NaF/KF Postdeposition Treatment of Cu(In,Ga)Se_2 Thin-Film Solar Cell Absorbers. *ACS Applied Materials & Interfaces*, 9(4):3581–3589, 2017.

[60] F. Pianezzi, P. Reinhard, A. Chirila, B. Bissig, S. Nishiwaki, S. Buecheler, and A. N. Tiwari. Unveiling the effects of post-deposition treatment with different alkaline elements on the electronic properties of CIGS thin film solar cells. *Phys. Chem. Chem. Phys.*, 16:8843–8851, 2014.

[61] Y. Aida, V. Depredurand, J. K. Larsen, H. Arai, D. Tanaka, M. Kurihara, and S. . Cu-rich Cu$InSe_2$ solar cells with a Cu-poor surface. *Progress in Photovoltaics: Research and Applications*, 23(6), 2015.

[62] S. Siebentritt, L. Gütay, D. Regesch, Y. Aida, and V. Deprédurand. Why do we make Cu(In,Ga)Se_2 solar cells non-stoichiometric? *Solar Energy Materials and Solar Cells*, 119:18 – 25, 2013.

[63] Mt. Wagner, I. Dirnstorfer, D. M. Hofmann, M. D. Lampert, F. Karg, and B. K. Meyer. Characterization of Cu(In,Ga)Se_2 Thin Films. *physica status solidi (a)*, 167(1):131–142, 1998.

[64] S. Siebentritt, N. Rega, A. Zajogin, and M. Ch. Lux-Steiner. Do we really need another PL study of $CuInSe_2$? *physica status solidi (c)*, 1(9):2304–2310, 2004.

[65] S. Siebentritt and S. Schuler. Defects and transport in the wide gap chalcopyrite $CuGaSe_2$. *Journal of Physics and Chemistry of Solids*, 64(9):1621 – 1626, 2003. 13th International Conference on Ternary and Multinary Compounds.

[66] M. Turcu, O. Pakma, and U. Rau. Interdependence of absorber composition and recombination mechanism in Cu(In,Ga)$(Se,S)_2$ heterojunction solar cells. *Applied Physics Letters*, 80(14):2598–2600, 2002.

[67] D. Schmid, M. Ruckh, F. Grunwald, and H. W. Schock. Chalcopyrite/defect chalcopyrite heterojunctions on the basis of $cuinse_2$. *Journal of Applied Physics*, 73(6): 2902–2909, 1993.

[68] S. Lany and A. Zunger. Intrinsic dx centers in ternary chalcopyrite semiconductors. *Phys. Rev. Lett.*, 100:016401, 2008.

[69] Xing-Liang Yin, Jie Liu, Wen-Jie Jiang, Xing Zhang, Jin-Song Hu, and Li-Jun Wan. Urchin-like Au@CdS/WO3 micro/nano heterostructure as a visible-light driven photocatalyst for efficient hydrogen generation. *Chem. Commun.*, 51:13842–13845, 2015.

[70] Q. Zhao, B. Zhang, W. Yao, Q. Wu, and C. Huang. Synthesis and photocatalytic activity of hollow CdS microspheres. *Catal. Sci. Technol.*, 6:8474–8481, 2016.

[71] Y. Lee, C. V. V. M. Gopi, A. Eswar Reddy, C. Nagaraju, and H. J. Kim. High performance of TiO2/CdS quantum dot sensitized solar cells with a Cu-ZnS passivation layer. *New J. Chem.*, 41:1914–1917, 2017.

[72] L. Li, X. Yang, J. Gao, H. Tian, J. Zhao, A. Hagfeldt, and L. Sun. Highly Efficient CdS Quantum Dot-Sensitized Solar Cells Based on a Modified Polysulfide Electrolyte. *Journal of the American Chemical Society*, 133(22):8458–8460, 2011.

[73] K. Deng and L. Li. CdS Nanoscale Photodetectors. *Advanced Materials*, 26(17): 2619–2635, 2014.

[74] M. Zayats, A. B. Kharitonov, S. P. Pogorelova, O. Lioubashevski, E. Katz, and I. Willner. Probing Photoelectrochemical Processes in Au-CdS Nanoparticle Arrays by Surface Plasmon Resonance: Application for the Detection of Acetylcholine Esterase Inhibitors. *Journal of the American Chemical Society*, 125(51):16006–16014, 2003.

[75] W. W Zhao, J. Wang, J. J. Xu, and H. Y. Chen. Energy transfer between CdS quantum dots and Au nanoparticles in photoelectrochemical detection. *Chem. Commun.*, 47:10990–10992, 2011.

[76] T. Kiyonaga, T. Akita, and H. Tada. Au nanoparticle electrocatalysis in a photoelectrochemical solar cell using CdS quantum dot-sensitized TiO_2 photoelectrodes. *Chem. Commun.*, pages 2011–2013, 2009.

[77] I. Ibrahim, H. N. Lim, O. K. Abou-Zied, N. M. Huang, P. Estrela, and A. Pandikumar. Cadmium Sulfide Nanoparticles Decorated with Au Quantum Dots as Ultrasensitive Photoelectrochemical Sensor for Selective Detection of Copper(II) Ions. *The Journal of Physical Chemistry C*, 120(39):22202–22214, 2016.

[78] K. D. Dobson, I. Visoly-Fisher, G.Hodes, and D. Cahen. Stability of CdTe/CdS thin-film solar cells. *Solar Energy Materials and Solar Cells*, 62(3):295 – 325, 2000.

[79] S. Han, L. Hu, N. Gao, A. A. Al-Ghamdi, and X. Fang. Efficient Self-Assembly Synthesis of Uniform CdS Spherical Nanoparticles-Au Nanoparticles Hybrids with Enhanced Photoactivity. *Advanced Functional Materials*, 24(24), 2014.

[80] S. Q. Sun and T. Li. Synthesis and Characterization of CdS Nanoparticles and Nanorods via Solvo-Hydrothermal Route. *Crystal Growth & Design*, 7(11):2367–2371, 2007.

[81] Wekks A.F. Structural Inorganic Chemistry. *Oxford Science Publications*, 5th edition: 835–842, Sep 1952.

[82] R. Ortega-Borges and D. Lincot. Mechanism of Chemical Bath Deposition of Cadmium Sulfide Thin Films in the Ammonia-Thiourea System In Situ Kinetic Study and Modelization. *J. Electrochem. Soc. 1993*, 140:3464–3473, 1992.

[83] L. Weinhardt, O. Fuchs, D. Groß, E. Umbach, C. Heske, N. G. Dhere, A. A. Kadam, and S. S. Kulkarni. Surface modifications of $Cu(In,Ga)S_2$ thin film solar cell absorbers by KCN and H_2O_2/H_2SO_4 treatments. *Journal of Applied Physics*, 100(2):024907, 2006.

[84] H. C. Zeng. Ostwald Ripening: A Synthetic Approach for Hollow Nanomaterials. *Current Nanoscience*, 3(2):177–181, 2007.

[85] J. Chantana, D. Hironiwa, T. Watanabe, S. Teraji, K. Kawamura, and T. Minemoto. Investigation of $Cu(In,Ga)Se_2$ absorber by time-resolved photoluminescence for improvement of its photovoltaic performance. *Solar Energy Materials and Solar Cells*, 130:567 – 572, 2014.

[86] M Burgelman, P Nollet, and S Degrave. Modelling polycrystalline semiconductor solar cells. *Thin Solid Films*, 361-362:527 – 532, 2000.

[87] Weierstrass Institute. Modelling and simulation of semiconductor devices. *http://www.wias-berlin.de/software/tesca for WIAS-TeSCA*.

[88] Comsol. The finite element method. *https://www.comsol.de/multiphysics/finite-element-method*.

[89] M. Raghuwanshi, B. Thöner, P. Soni, M. Wuttig, R. Wuerz, and O. Cojocaru-MirÃľdin. Evidence of Enhanced Carrier Collection in $Cu(In,Ga)Se_2$ Grain Boundaries: Correlation with Microstructure. *ACS Applied Materials & Interfaces*, 10(17):14759–14766, 2018.

[90] Harndt, S., Kaufmann, C. A., Lux-Steiner, M. C., Klenk, R., and Nürnberg, R.r. Grain boundary assisted photocurrent collection in thin film solar cells. *EPJ Photovolt.*, 6: 60101, 2015.

[91] G. Dingemans and W. M. M. Kessels. Status and prospects of Al_2O_3-based surface passivation schemes for silicon solar cells. *Journal of Vacuum Science & Technology A: Vacuum, Surfaces, and Films*, 30(4):040802, 2012.

[92] S. W. Glunz, D. Biro, S. Rein, and W. Warta. Field-effect passivation of the SiO_2Si interface. *Journal of Applied Physics*, 86(1):683–691, 1999.

[93] A. G. Aber;e, S. Glunz, and W. Warta. Field effect passivation of high efficiency silicon solar cells. *Solar Energy Materials and Solar Cells*, 29(2):175 – 182, 1993.

[94] Q Cao, O Gunawan, M Copel, K. B. Reuter, S. J. Chey, V. R. Deline, and D. B. Mitzi. Defects in Cu(In,Ga)Se_2 Chalcopyrite Semiconductors: A Comparative Study of Material Properties, Defect States, and Photovoltaic Performance. *Advanced Energy Materials*, 1(5):845–853, 2011. ISSN 1614-6840.

[95] H. Y. Yu, M. F. Li, B. J. Cho, C. C. Yeo, M. S. Joo, D.-L. Kwong, J. S. Pan, C. H. Ang, J. Z. Zheng, and S. Ramanathan. Energy gap and band alignment for $(HfO_2)_x(Al_2O_3)_{1-x}$ on (100) Si. *Applied Physics Letters*, 81(2):376–378, 2002.

[96] R. L. Anderson. Germanium-gallium arsenide heterojunctions [letter to the editor]. *IBM Journal of Research and Development*, 4(3):283–287, 1960.

[97] D. Schmid, M. Ruckh, and H. Werner Schock. A comprehensive characterization of the interfaces in Mo/CIS/CdS/ZnO solar cell structures. *Solar Energy Materials and Solar Cells*, 41-42:281 – 294, 1996.

[98] C. Platzer-Björkman, T. Törndahl, D. Abou-Ras, J. Malmström, J. Kessler, and L. Stolt. Zn(O,S) buffer layers by atomic layer deposition in Cu(In,Ga)Se_2 based thin film solar cells: Band alignment and sulfur gradient. *Journal of Applied Physics*, 100(4):044506, 2006.

[99] M. Gloeckler and J. R. Sites. Potential of submicrometer thickness Cu(In,Ga)Se_2 solar cells. *Journal of Applied Physics*, 98(10):103703, 2005.

[100] J. Sterner, J. Malmström, and L. Stolt. Study on ALD In_2S_3/Cu(In,Ga)Se_2 interface formation. *Progress in Photovoltaics: Research and Applications*, 13(3):179–193, 2005.

[101] T. Törndahl, C. Platzer-Björkman, J. Kessler, and M. Edoff. Atomic layer deposition of $Zn_{1-x}Mg_xO$ buffer layers for Cu(In,Ga)Se_2 solar cells. *Progress in Photovoltaics: Research and Applications*, 15(3), 2007.

[102] O. Cojocaru-Mirédin, Y. Fu, A. Kostka, R. Sáez-Araoz, A. Beyer, N. Knaub, K. Volz, C. H. Fischer, and D. Raabe. Interface engineering and characterization at the atomic-scale of pure and mixed ion layer gas reaction buffer layers in chalcopyrite thin-film solar cells. *Progress in Photovoltaics: Research and Applications*, 23(6): 705–716, 2015.

[103] B. Vermang, J. T. Wätjen, C. Frisk, V. Fjällström, F. Rostvall, M. Edoff, P. Salomé, J. Borme, N. Nicoara, and S. Sadewasser. Introduction of Si PERC Rear Contacting Design to Boost Efficiency of Cu(In,Ga)Se_2 Solar Cells. *IEEE Journal of Photovoltaics*, 4(6):1644–1649, 2014.

[104] J. Kiss, T. Gruhn, G. Roma, and C. Felser. Theoretical Study on the Diffusion Mechanism of Cd in the Cu-Poor Phase of $CuInSe_2$ Solar Cell Material. *The Journal of Physical Chemistry C*, 117(49):25933–25938, 2013.

[105] M. Nerat. Copper-indium-gallium-selenide (CIGS) solar cells with localized back contacts for achieving high performance. *Solar Energy Materials and Solar Cells*, 104:152 – 158, 2012.

[106] F. Erfurth, Z. Jeh, M. Bouttemy, N. Dahan, P. Tran-Van, A. Etcheberry I. Gerard, J.-J. Greffet, M. Powalla, G. Voorwinden, D. Lincot, J.F. Guillemoles, and N. Naghavi. Mo/Cu(In, Ga)Se_2 back interface chemical and optical properties for ultrathin CIGSe solar cells. *Applied Surface Science*, 258(7):3058 – 3061, 2012.

[107] J. Li, S. Glynn, S. Christensen, J. Mann, B. To, K. Ramanathan, R. Noufi, T. E. Furtak, and D. Levi. Optical properties of Zn(O,S) thin films deposited by RF sputtering, atomic layer deposition, and chemical bath deposition. *38th IEEE Photovoltaic Specialists Conference*, pages 001580–001583, June 2012.

[108] L. Kronik, L. Burstein, M. Leibovitch, Yoram Shapira, D. Gal, E. Moons, J. Beier, G. Hodes, David Cahen, D. Hariskos, R. Klenk, and H.-W. Schock. Band diagram of the polycrystalline CdS/Cu(In,Ga)Se_2 heterojunction. *Applied Physics Letters*, 67 (10):1405–1407, 1995.

[109] S. Sharbati and J. R. Sites. Impact of the Band Offset for n-Zn(O,S)/p-Cu(In,Ga)Se_2 Solar Cells. *IEEE Journal of Photovoltaics*, 4(2):697–702, 2014.

[110] J. W. Pankow, K. Xerxes Steirer, L. M. Mansfield, R. L. Garris, K. Ramanathan, and G. R. Teeter. Band alignment of CBD deposited Zn(O,S)/Cu(In_{1-x}, Ga_x)Se_2 interface. *2014 IEEE 40th Photovoltaic Specialist Conference (PVSC)*, pages 1670–1673, 2014.

[111] M. Mezher, R. Garris, L. M. Mansfield, K. Horsley, L. Weinhardt, D. A. Duncan, M. Blum, S. G. Rosenberg, M. Bär, K. Ramanathan, and C. Heske. Electronic structure of the Zn(O,S)/Cu(In,Ga)Se_2 thin-film solar cell interface. *Progress in Photovoltaics: Research and Applications*, 24(8):1142–1148, 2016.

[112] C.A. Kaufmann, T. Unold, D. Abou-Ras, J. Bundesmann, A. Neisser, R. Klenk, R. Scheer, K. Sakurai, and H.-W. Schock. Investigation of coevaporated Cu(In,Ga)Se_2 thin films in highly efficient solar cell devices. *Thin Solid Films*, 515 (15):6217 – 6221, 2007. Proceedings of Sympodium O on Thin Film Chalcogenide Photovoltaic Materials, EMRS 2006 Conference.

[113] R. Scheer, L. Messmann-Vera, R. Klenk, and H.-W. Schock. On the role of non-doped ZnO in CIGSe solar cells. *Progress in Photovoltaics: Research and Applications*, 20(6):619–624, 2012.

[114] B. Vermang, V. Fjällström, J. Pettersson, P. Salomé, and M. Edoff. Development of rear surface passivated Cu(In,Ga)Se_2 thin film solar cells with nano-sized local rear point contacts. *Solar Energy Materials and Solar Cells*, 117:505 – 511, 2013.

[115] J. Kessler, K. O. Velthaus, M. Ruckh, R. Laichinger, D. Lincot H. W. Schock, R. Ortega, and J. Vedel. Chemical bath deposition of CdS on $CuInSe_2$, etching effects and growth kinetics. *Proccedings Sixth Int PVSEC*, pages 1005–1010, 1992.

[116] J. Oh, J. Myoung, J. S. Bae, and S. Lim. Etch Behavior of ALD Al_2O_3 on HfSiO and HfSiON Stacks in Acidic and Basic Etchants. *Journal of The Electrochemical Society*, 158(4):D217–D222, 2011.

[117] W. Witte, S. Spiering, and D. Hariskos. Substitution of the CdS buffer layer in CIGS thin-film solar cells. *Vakuum in Forschung und Praxis*, 26(1):23–27, 2014.

[118] C. S. Tao, J. Jiang, and M. Tao. Natural resource limitations to terawatt-scale solar cells. *Solar Energy Materials and Solar Cells*, 95(12):3176 – 3180, 2011.

[119] V. Fthenakis. Sustainability of photovoltaics: The case for thin-film solar cells. *Renewable and Sustainable Energy Reviews*, 13(9):2746 – 2750, 2009.

[120] G. Yin, V. Brackmann, V. Hoffmann, and M. Schmid. Enhanced performance of ultrathin Cu(In,Ga)Se_2 solar cells deposited at low process temperature. *Solar Energy Materials and Solar Cells*, 132:142 – 147, 2015.

[121] M. Bouttemy, P. Tran-Van, I. Gerard, T. Hildebrandt, A. Causier, J.L. Pelouard, G. Dagher, Z. Jehl, N. Naghavi, G. Voorwinden, B. Dimmler, M. Powalla, J.F. Guillemoles, D. Lincot, and A. Etcheberry. Thinning of CIGS solar cells: Part I: Chemical processing in acidic bromine solutions. *Thin Solid Films*, 519(21):7207 – 7211, 2011. Proceedings of the EMRS 2010 Spring Meeting Symposium M: Thin Film Chalcogenide Photovoltaic Materials.

[122] O. Lundberg, M. Bodegard, J. Malmström, and L. Stolt. Influence of the Cu(In,Ga)Se_2 thickness and Ga grading on solar cell performance. *Progress in Photovoltaics: Research and Applications*, 11(2):77–88, 2003.

[123] B.M. Keyes, F. Hasoon, P. Dippo, A. Balcioglu, and F. Abulfotuh. Influence of Na on the ElectroOptical Properties of Cu(In,Ga)Se_2 . *26th IEEE Photovoltaic Specialists Conference*, 1997.

[124] D. Rudmann, A.F. da Cunha, M. Kaelin, F.-J. Haug, H. Zogg, and A.N. Tiwari. Effects of Na on The Growth of Cu(In, Ga)Se_2 Thin Films and Solar Cells. *MRS Proceedings*, 763, 2003.

[125] P. Salomé, V. Fjällström, A. Hultqvist, and M. Edoff. Na Doping of CIGS Solar Cells Using Low Sodium-Doped Mo Layer. *IEEE Journal of Photovoltaics*, 3(1):509–513, 2013.

[126] A. Hultqvist, J. V. Li, D. Kuciauskas, P. Dippo, M. A. Contreras, D. H. Levi, and S. F. Bent. Reducing interface recombination for Cu(In,Ga)Se_2 by atomic layer deposited buffer layers. *Applied Physics Letters*, 107(3):033906, 2015.

[127] S. Garud, N. Gampa, T. G. Allen, R. Kotipalli, D. Flandre, M. Batuk, J. Hadermann, M. Meuris, J. Poortmans, A. Smets, and B. Vermang. Surface passivation of cigs solar cells using gallium oxide. *Physica Status Solidi (A)*, 0(0):1700826, 2018.

[128] W.L. Bragg. The structure of some crystals as indicated by their diffraction of X-rays. *Proceedings of the Royal Society of London A: Mathematical, Physical and Engineering Sciences*, 89(610):248–277, 1913.

[129] D. Briggs and M. P. Seah. *Practical Surface Analysis, Auger and X-ray Photoelectron Spectroscopy*. Wiley, Chichester, 1983.

[130] D.A. Shirley. High-resolution x-ray photoemission spectrum of the valence bands of gold. *Phys. Rev. B*, 5:4709–4714, 1972.

[131] M. P. Seah. The quantitative analysis of surfaces by XPS: A review. *Surface and Interface Analysis*, 2(6):222–239, 1980.

[132] C. D. Wagner, L. E. Davis, M. V. Zeller, J. A. Taylor, R. H. Raymond, and L. H. Gale. Empirical atomic sensitivity factors for quantitative analysis by electron spectroscopy for chemical analysis. *Surface and Interface Analysis*, 3(5):211–225, 1981.

[133] I. Lauermann, M. Bär, and C. H. Fischer. Synchrotron-based spectroscopy for the characterization of surfaces and interfaces in chalcopyrite thin-film solar cells. *Solar Energy Materials and Solar Cells*, 95(6):1495 – 1508, 2011.

[134] R. Tschöke. *Untersuchung der Phasenbildung in Cu/In-Legierungen als Ausgangsmaterialien für $CuInS_2$-Dünnschichtsolarzellen*. Master thesis dissertation, Freie Universität Berlin, 2010.

[135] V. Efimova. *Study in analytical glow discharge spectrometry and its application in materials science*. PhD dissertation, Technische Universität Dresden, 2012.

[136] C. L. Haynes and R. P. Van Duyne. Nanosphere Lithography: A Versatile Nanofabrication Tool for Studies of Size-Dependent Nanoparticle Optics. *The Journal of Physical Chemistry B*, 105(24):5599–5611, 2001.

List of publications

Part of this thesis has already been published:

- A. Bercegol, B. Chacko, R. Klenk, I. Lauermann, M. Liero and M. Ch. Lux-Steiner. Point contacts at the copper-indium-gallium-selenide interface – A theoretical outlook, *Journal of Applied Physics*, 119 (2016).

Other journal publications:

- I. Majumdar, B. Ümsür, B. Chacko, D. Greiner, M. Ch. Lux-Steiner, R. Schlatmann and I. Lauermann. Surface modifications of Na and K metal incorporated Cu(In,Ga)Se_2 absorbers investigated by synchrotron-based spectroscopies, *physica status solidi (c)*, 14 (2017).

- T.Olar, A. Manoharan, C. Draxl, W. Calvet, B.Ümsür, V. Parvan, B. Chacko, H. Xie, E. Saucedo, L. Elisa Valle-Rios, K. Neldner, S. Schorr, M. Ch. Lux-Steiner, I. Lauermann. Valence and conduction band edges of selenide and sulfide-based kesterites - A study by x-ray based spectroscopy and ab initio theory, *Semiconductor Science and Technology*, 32 (2017).

- T. Olar, I. Lauermann, H. Xie, M. Neuschitzer, E. Saucedo, W. Calvet, A. Steigert, B. Ümsür, B. Chacko, V. Parvan, M. Gorgoi, B. Senkovskiy and M. Ch. Lux-Steiner. Assessment of chemical and electronic surface properties of the $Cu_2ZnSn(SSe)_4$ after different etching procedures by synchrotron-based spectroscopies, *Energy Procedia*, 84, 8-16 (2015).

Oral and poster presentations:

- B. Chacko, M.D. Heinemann, D. Greiner, M. Ch. Lux-Steiner, R. Schlatmann and I. Lauermann, Point contacts at the CIGSe front interface - a prototype. *E-MRS Spring Meeting*, poster session, 05/2017, Strasbourg, France.

- W. Calvet, B. Ümsür, A. Steigert, I. Lauermann, B. Chacko, V. Parvan, T. Olar, K. Prietzel, H.A. Navirian, S. Brunken, C.A. Kaufmann, D. Greiner, T. Unold, M.Ch. Lux-Steiner, Comparison of surface composition, electronic properties, and solar cell performance of UHV-transferred and air exposed CIGSe thin film solar cell absorbers.

31st European Photovoltaic Solar Energy Conference and Exhibition, 09/2015, Hamburg, Germany.

- T. Olar, I. Lauermann, H. Xie, E. Saucedo, W. Calvet, A. Steigert, B. Ümsür, B. Chacko, V. Parvan, M.Ch. Lux-Steiner, Assessment of the $Cu_2ZnSnSSe_4$ chemical and electronic surface properties after different etching procedures by synchrotron-based spectroscopies. *E-MRS Spring Meeting*, 05/2015, Lille, France.

- I. Majumdar, B. Ümsür, M. Heinemann, B. Chacko, D. Smirnov, W. Calvet, V. Parvan, A. Mizrak, I. Lauermann, Depth profiled XPS analysis and NEXAFS study of Na, K-PDT on CIGSe as a function of deposition temperature using synchrotron radiation. *MSE Congress*, poster session, 09/2016, Darmstadt, Germany.

- W. Calvet, I. Majumdar, B. Ümsür, A. Steigert, B. Chacko, V. Parvan, T. Olar, C. A. Kaufmann, D. Greiner, J. Lauche, H. Navirian, G. Voorwinden, W. Mannstadt, R. Schlatmann, M. Ch. Lux-Steiner, I. Lauermann, Analysis of surface composition and device performance of UHV and air-transferred CIGSe thin film solar cell absorbers on alkali-containing substrate glass. *32nd European Photovoltaic Solar Energy Conference and Exhibition*, poster session, 06/2016, Munich, Germany.

- W. Calvet, B. Ümsür, A. Steigert, I. Lauermann, B. Chacko, V. Parvan, T. Olar, K. Prietzel, H.A. Navirian, S. Brunken, C.A. Kaufmann, D. Greiner, T. Unold, M.Ch. Lux-Steiner, Comparison of surface composition, electronic properties, and solar cell performance of UHV-transferred and air exposed CIGSe thin film solar cell absorbers. *E-MRS Spring Meeting*, poster session, 05/2015, Lille, France.

Acknowledgements

Through this work, there has been a number of people who lend their help and support to give it a final shape. At this time, I would like to thank them all.

- Prof. M. Ch. Lux-Steiner for accepting me as a PhD student and giving me the opportunity to realise this work in her department at the Helmholtz-Zentrum Berlin. Also for her great supervision and corrections of the thesis.
- Prof. Paul Fumagalli for agreeing to be my second examiner.
- Iver Lauermann for welcoming me to his CISSY group, his excellent tutoring and supervision through my PhD work, lots of patience, introducing and sharing his knowledge and experience on x-ray photoelectron spectroscopy and proofreading of this thesis.
- Reiner Klenk, Adrien Bercegol and Matthias Liero for the simulation work on point contacts at CIGSe solar cells.
- Marc Daniel Heinemann for back point contact CIGSe solar cells, GDOES and CV measurements.
- Daniel Abou-Ras for facilitating the SEM. Jaison Kavalakkatt and Carola Klimm for SEM images.
- Christian Kaufmann, Dieter Greiner, Marc Daniel Heinemann, Jakob Lauche for providing me Cu(In,Ga)Se_2 absorbers during this work.
- Sergej Levcenco, Thomas Unold and Karolina Mack for PL measurements.
- Sonya Calnan and Iris Dorbandt for ALD and CBD deposition.
- The current and the former members of the CISSY group: Wolfram Calvet, Alexander Steigert, Bünyamin Ümsür, Britta Höpfner, Vladimir Parvan, Isheta Majumdar, Yajie Wang, Natalia Maticiuc, Robert Wenisch, Tetiana Olar, Adrien Bercegol, and Ali Vâlâ Mizark for sharing their knowledge and creating a pleasant work atmosphere through these years.

- Erasmus Mundus EMINTE scholarship programme for supporting my PhD at the Freie Universitüt Berlin and Helmholtz-Zentrum Berlin
- My family, my parents, my brother, my girlfriend Fritzi and her parents, and my friends for their continuous support, showing the life outside research and keeping me motivated at the same time.

Selbständigkeitserklärung

Hiermit erkläre ich, dass ich die vorliegende Dissertation selbständig verfasst und nur mit Hilfe der angegebenen Quellen angefertigt habe. Ich versichere, dass diese Arbeit nicht schon einmal in einem früheren Promotionsverfahren angenommen oder als ungenügend beurteilt worden ist.

Berlin, 19.09.2018	
Ort, Datum	Binoy Chacko

Curriculum Vitae

For reasons of data protection, the curriculum vitae is not published in the electronic version.